

Optimization of solution composition in hexagonal boron nitride crystal growth via the flux method

by

Eli Janzen

B.S., Kansas State University, 2018

AN ABSTRACT OF A DISSERTATION

submitted in partial fulfillment of the requirements for the degree

DOCTOR OF PHILOSOPHY

Tim Taylor Department of Chemical Engineering
Carl R. Ice College of Engineering

KANSAS STATE UNIVERSITY
Manhattan, Kansas

2023

Abstract

Hexagonal boron nitride (hBN) is an ultrawide bandgap (>6 eV) semiconductor and 2D material that has attracted much attention due to its unique properties and applications in electronics, optoelectronics, and nanophotonics. In all of these applications, large, high quality single crystals of hBN are required and atmospheric pressure solution growth is a consistent method to achieve this. This study was undertaken to improve this process, accelerate its optimization, and enable creation of devices in a wide range of fields.

A new methodology was developed to optimize the boron concentration in hBN solution growth using the CALPHAD (CALculation of PHase Diagrams) method to rapidly predict the optimal boron concentration for a wide range of solvents. Comparison with experimental results validates its accuracy. Deviations from CALPHAD predictions, confirmed with crystal growth by reusing source material, suggest that the hBN crystal growth process from molten metal solutions is kinetically limited. Reusing source material also substantially improves the yield of boron to hBN, which is especially important when using expensive isotopically pure boron for growth of $h^{10}\text{BN}$ or $h^{11}\text{BN}$.

Increasing the nitrogen solubility of the solvent is often attributed to increasing crystal size, but this work digs deeper into the effects of this property. Five different solvents (Ni-Cr, Co-Cr, Fe, Fe-V, and Cu) were tested and the domain area and thickness of crystals they produced were compared versus their nitrogen solubility. The nitrogen solubility did not affect the hBN domain area but the crystal thickness increased with nitrogen solubility. This suggests that, so long as the boron concentration is properly optimized, similar domain sizes can be obtained from any solvent. Furthermore, the thickness of as-grown crystals may be engineered for specific applications by choosing a solvent that naturally grows hBN of the required

thickness. Finally, the optimal boron concentration increased with the nitrogen solubility, provides a shortcut for optimizing future solvents, accelerating research.

Crystal defects such as stacking faults, dislocations, and impurities are detrimental to device performance, thus it is important to understand their properties and how they can be avoided or eliminated. Oxygen impurities were greatly reduced in the solvent with the introduction of hydrogen gas while carbon impurities may need to react with oxygen to be removed. Regardless, the impurity content in hBN crystals grown from these solvents was below the detection limit of secondary ion mass spectrometry (SIMS) in all cases, suggesting the purity of the process is already sufficient. Three classes of defects were detected using cathodoluminescence (CL) spectroscopy: spots, invisible lines, and wrinkles, which were determined to be color centers, half-inserted planes, and plastic deformation of hBN single crystals, respectively. A combination of Raman, photoluminescence (PL), and CL spectroscopy indicates that hBN crystals grown from Ni-Cr and Co-Cr tend to have fewer defects than those grown from Fe, Fe-V, or Cu.

Monoisotopic hBN is especially useful in applications where coherence of phonons is especially important such as sub-wavelength optical microscopy and quantum sensing. Previously, processes were developed to synthesize hBN enriched with either the ^{10}B or ^{11}B isotopes using naturally abundant $^{14}\text{N}_2$. In this work, a new process was developed to extend the capabilities of solution growth to also produce hBN with the ^{15}N isotope. Raman and PL spectroscopy on these crystals indicate that they are very high quality, on par with crystals grown with ^{14}N . Furthermore, the effect of the reduced mass on the Raman shift of the E_{2g}^{high} peak and the energy of the phonon replicas is identified, which is in excellent agreement with theory.

Optimization of solution composition in hexagonal boron nitride crystal growth via the flux method

By

Eli Janzen

B.S., Kansas State University, 2018

A DISSERTATION

submitted in partial fulfillment of the requirements for the degree

DOCTOR OF PHILOSOPHY

Tim Taylor Department of Chemical Engineering
Carl R. Ice College of Engineering

KANSAS STATE UNIVERSITY
Manhattan, Kansas

2023

Approved by:

Major Professor
Dr. James H. Edgar

Copyright

© Eli Janzen 2023.

Abstract

Hexagonal boron nitride (hBN) is an ultrawide bandgap (>6 eV) semiconductor and 2D material that has attracted much attention due to its unique properties and applications in electronics, optoelectronics, and nanophotonics. In all of these applications, large, high quality single crystals of hBN are required and atmospheric pressure solution growth is a consistent method to achieve this. This study was undertaken to improve this process, accelerate its optimization, and enable creation of devices in a wide range of fields.

A new methodology was developed to optimize the boron concentration in hBN solution growth using the CALPHAD (CALculation of PHase Diagrams) method to rapidly predict the optimal boron concentration for a wide range of solvents. Comparison with experimental results validates its accuracy. Deviations from CALPHAD predictions, confirmed with crystal growth by reusing source material, suggest that the hBN crystal growth process from molten metal solutions is kinetically limited. Reusing source material also substantially improves the yield of boron to hBN, which is especially important when using expensive isotopically pure boron for growth of $h^{10}\text{BN}$ or $h^{11}\text{BN}$.

Increasing the nitrogen solubility of the solvent is often attributed to increasing crystal size, but this work digs deeper into the effects of this property. Five different solvents (Ni-Cr, Co-Cr, Fe, Fe-V, and Cu) were tested and the domain area and thickness of crystals they produced were compared versus their nitrogen solubility. The nitrogen solubility did not affect the hBN domain area but the crystal thickness increased with nitrogen solubility. This suggests that, so long as the boron concentration is properly optimized, similar domain sizes can be obtained from any solvent. Furthermore, the thickness of as-grown crystals may be engineered for specific applications by choosing a solvent that naturally grows hBN of the required

thickness. Finally, the optimal boron concentration increased with the nitrogen solubility, provides a shortcut for optimizing future solvents, accelerating research.

Crystal defects such as stacking faults, dislocations, and impurities are detrimental to device performance, thus it is important to understand their properties and how they can be avoided or eliminated. Oxygen impurities were greatly reduced in the solvent with the introduction of hydrogen gas while carbon impurities may need to react with oxygen to be removed. Regardless, the impurity content in hBN crystals grown from these solvents was below the detection limit of secondary ion mass spectrometry (SIMS) in all cases, suggesting the purity of the process is already sufficient. Three classes of defects were detected using cathodoluminescence (CL) spectroscopy: spots, invisible lines, and wrinkles, which were determined to be color centers, half-inserted planes, and plastic deformation of hBN single crystals, respectively. A combination of Raman, photoluminescence (PL), and CL spectroscopy indicates that hBN crystals grown from Ni-Cr and Co-Cr tend to have fewer defects than those grown from Fe, Fe-V, or Cu.

Monoisotopic hBN is especially useful in applications where coherence of phonons is especially important such as sub-wavelength optical microscopy and quantum sensing. Previously, processes were developed to synthesize hBN enriched with either the ^{10}B or ^{11}B isotopes using naturally abundant $^{14}\text{N}_2$. In this work, a new process was developed to extend the capabilities of solution growth to also produce hBN with the ^{15}N isotope. Raman and PL spectroscopy on these crystals indicate that they are very high quality, on par with crystals grown with ^{14}N . Furthermore, the effect of the reduced mass on the Raman shift of the E_{2g}^{high} peak and the energy of the phonon replicas is identified, which is in excellent agreement with theory.

Table of Contents

Table of Contents	viii
List of Figures	x
List of Tables	xxi
Acknowledgements	xxii
Chapter 1 - Introduction	1
1.1 Properties and Applications of hBN Single Crystals	1
1.2 Basics of Solution Growth Method	5
1.2.1 Solubility and Saturation	6
1.2.2 Methods of Supersaturation	9
1.2.3 Nucleation and Crystal Growth	11
1.3 Prior Work on hBN Solution Growth	12
1.3.1 High Pressure Synthesis	13
1.3.2 Atmospheric Pressure Synthesis	15
1.3.3 Synthesis of Monoisotopic hBN	22
1.4 Standard Crystal Growth Process	24
1.5 References	30
Chapter 2 - Optimizing Boron Concentration	34
2.1 CALPHAD Modeling	36
2.2 Experimental Validation	41
2.3 Expected vs. Observed Yield	45
2.4 References	52
Chapter 3 - hBN Size vs Solvent Properties	54
3.1 Synthesis and Optimization	56
3.2 Experimental Results	61
3.3 Effects of Nitrogen Solubility on hBN Growth	65
3.4 References	69
Chapter 4 - Understanding Defects in hBN	71
4.1 Impurity Sources and Sinks	71
4.2 Classification of Defects	75
4.2.1 Characterizing Defects with CL Spectroscopy	76
4.2.2 Spots	80
4.2.3 Wrinkles	82
4.2.4 Invisible Lines	86

4.3	Correlating Crystal Quality to Solvent Species	88
4.3.1	Raman Spectroscopy.....	89
4.3.2	Photoluminescence Spectroscopy	90
4.3.3	Cathodoluminescence Spectroscopy.....	92
4.4	References	94
Chapter 5	- Isotopic Control in hBN Synthesis.....	95
5.1	Introduction.....	95
5.2	Synthesis.....	99
5.3	Results	102
5.4	Conclusions	107
5.5	References	108
Chapter 6	- Conclusions and Recommendations	111
Appendix A	- Images for Determining Domain Size Distribution.....	115
Appendix B	- Code for CL Data Analysis.....	119
B.1	Code for Decomposition.....	119
B.2	Code for Normalization	152

List of Figures

Figure 1 – Diagram of the atomic structure of hBN showing the in-plane honeycomb structure (left) and the alternating AA' stacking structure between planes (right) with a, b, and c directions labeled.	2
Figure 2 – Fe-B phase diagram with the sections of the liquidus that represent the maximum boron concentration that can be dissolved at a given temperature highlighted in red. [27].....	7
Figure 3 – Solubility of nitrogen versus temperature in molten Fe-Cr alloys at varying chromium concentrations. Curves based on model parameters given in [28]. Changing the concentration of chromium changes the slope and magnitude of nitrogen solubility curve.	8
Figure 4 – a) Schematic of solvent evaporation method. As the solvent evaporates, boron is left behind, which causes the solution to become supersaturated so that hBN precipitates. b) Schematic of temperature gradient method. Concentration gradient causes B & N to diffuse to cold side, where hBN precipitates due to lower solubility. c) Schematic of slow cooling method. As temperature decreases, solubility decreases and any excess B & N precipitates as hBN.	11
Figure 5 – Examples of hBN crystals grown at high pressure and temperature. a) Optical micrograph of an hBN single crystal grown from a Ba solvent at high temperature (1500-1650°C) and high pressure (4-5 GPa) [36]. b) SEM image of hBN crystals grown from a nickel solvent at 6 GPa and 1600°C [37]. c) Photograph of hBN flakes produced using a magnesium solvent at 3 GPa and 1900-2100°C [38].	14
Figure 6 – a) Large hBN flake produced by Ishii and Sato [31] in a Si solvent at 1850°C. b) Large single crystal grown from molten BaF ₂ -Li ₃ N salt at 820°C by Feigelson, Frazier, and	

Twigg [40]. c) Crystals grown from a mixture of NaBF₄, NaNH₂, and LiBr at 650°C by Gu et al [41]..... 16

Figure 7 – a) Differential interference microscope image of hBN grown from Ni-Mo solvent at 1400°C [42]. b) Photograph of hBN crystals grown from a Ni-Cr solvent at 1430°C. [43]..... 17

Figure 8 – a) Optical micrograph of 5 mm-wide hBN single crystal grown from a Ni-Cr with a dwell temperature of 1700°C and a cooling rate of 2°C/hr [45]. b) Optical micrograph of hBN crystals grown from Ni-Cr using a stepped growth process to encourage growth in both the a/b and c directions. Crystals tended to form the shape of pyramids with their a/b direction roughly perpendicular to the solvent surface [46]. c) Photograph of large hBN single crystals on the surface of the solidified Fe-Cr flux they were grown from [47]..... 18

Figure 9 – a) Optical micrograph of hBN grown from a Ni-Cr solvent containing 1.8 mass% carbon [48]. b) Optical micrograph of hBN grown from a Ni-Cr solvent containing 1.8 mass% carbon and 4.76 mass% gold to suppress precipitation of graphite [49]..... 19

Figure 10- a) Micrograph of hBN on the surface of an Fe-Cr ingot. Green lines outline grain boundaries of three crystals [50]. b) Photograph of hBN single crystal grown from a pure iron solvent on solidified ingot. Triangular hBN sheet is ~4 cm² in area. [51] 20

Figure 11 – a) SEM image of free-standing hBN crystal flakes grown from a Co-Cr solvent [52]. b) Photograph of hBN flake grown from a Cu-Cr solvent [53]. c) Optical micrograph of hBN grown with 16.2 at% B in a pure Fe solvent [54]..... 21

Figure 12 – a) Optical micrograph of h¹⁰BN grown from Ni-Cr with 11.78 mass% ¹⁰B by slowly cooling at 4°C/hr [55]. b) Optical micrograph of h¹⁰BN grown from Ni-Cr with 4 mass%

^{10}B by slowly cooling at 0.5°C/hr [57]. c) Optical micrograph of h^{11}BN grown from Fe-Cr with 3.2 mass% ^{11}B by slowly cooling at 4°C/hr [58]. 24

Figure 13 – a) Temperature profile of ingot formation experiments. b) Diagram of experimental setup inside the tube furnace. Hydrogen diluted with argon for safety continuously flowed over crucible to react with carbon and oxygen impurities and sweep them from the system. c) Results of ingot formation with and without N_2 present in the atmosphere for two solvents. Removing nitrogen produced more homogenous ingots. 25

Figure 14 – a) Temperature profile of crystal growth experiments with diagrams illustrating how crystal growth progresses. b) Diagram of experimental setup inside the tube furnace. Nitrogen and hydrogen continuously flowed over crucible. H_2 reacts with carbon and oxygen impurities and sweep them from the system. Nitrogen dissolves into the solvent and reacts with boron to form hBN 26

Figure 15 – a) Illustration of how mechanical exfoliation with thermal release tape is done. Some crystals inevitable become broken and are usually cleaved to produce thinner crystals. b) Optical micrograph of an hBN single crystal exfoliated from an ingot. 27

Figure 16 – a) Photograph of furnace 1 with components labeled. b) Schematic of gas flow and vacuum system attached to furnace 1. 28

Figure 17 - a) Photograph of furnace 2 with components labeled. b) Schematic of gas flow and vacuum system attached to furnace 2. 29

Figure 18 – Hypothetical liquidus curve of $\text{L} \rightarrow \text{hBN}$ illustrating how to optimize the boron concentration. A concentration that is too high will have a high nucleation rate due to being overly supersaturated, resulting in many small crystals. A concentration that is too low will waste time and energy because no hBN will precipitate until the system hits the liquidus. An

optimal concentration occurs where the liquidus intersects the starting temperature so that the system starts saturated, then slowly supersaturates to limit nucleation and produce few large crystals instead of many small ones..... 36

Figure 19 – Results of CALPHAD Modeling on Fe-B-N and Ni-Cr-B-N systems. Mass fraction of each phase is plotted versus temperature for the Fe-B-N system (a) and the Ni-Cr-B-N system (b) containing 3 mass% B. The temperature at which hBN first becomes stable upon cooling and the amount of hBN predicted to precipitate by the quench temperature are noted. C) The liquidus curves for both systems are derived by plotting the former versus the boron concentration used to calculate the phase equilibria..... 40

Figure 20 – Example of process used to extract crystal sizes from optical micrographs. a) Optical micrograph of hBN grown from an Fe solvent. b) Crystals highlighted by coloring over single crystals in the micrograph using a digital painting program. Blank areas are regions where the image was too dark or out of focus to properly identify crystals, so were excluded from analysis. c) Histogram showing how much of the image was filled by crystals of different size ranges. hBN single crystals $<0.01 \text{ mm}^2$ (red bar) are too small for device applications..... 43

Figure 21 – Coverage of Fe-grown hBN single crystals larger than 0.01 mm^2 in area versus the boron concentration added to the solution at the start of the experiment. Error bars show range of coverage measured in experiments with the same boron concentration. Optical micrographs of representative areas of the ingot surface for each concentration shown at bottom. Width of each image is 1 mm. 44

Figure 22 – Optical micrographs of hBN grown from Fe (left) and Ni-Cr (right) across 5 uses of the same source material..... 47

Figure 23 – Hypothetical liquidus curve illustrating how the boron concentration would change with temperature during solution growth of hBN in multiple uses of the same source material. a) Assuming the system is always at equilibrium, no hBN would be able to form in a second run due to the boron being depleted in the first. b) Assuming the system is kinetically limited, hBN could precipitate from the solution in multiple reuses of the source material because less hBN precipitates in each run than is thermodynamically possible. 49

Figure 24 – a) Diagrams of the self-limiting process hypothesized to be present in the process used in this work. Left – At the start of slow cooling, only a few hBN crystals have precipitated, allowing N₂ from the gas to dissolve into the solution uninhibited and maintaining the system near equilibrium. Right – At the end of slow cooling, hBN crystals fully cover the gas-solvent interface, blocking N₂ from dissolving into the solution. Any further growth must be fed by the reservoir of nitrogen and boron dissolved in the solution. b) Liquidus curve (black) compared to hypothetical state of the system (blue) as the system is slowly cooled. The system starts near equilibrium, but steadily deviates further and further from equilibrium as hBN covers more and more of the gas-solvent interface. 51

Figure 25 – Co-Cr phase diagram modified from ref. [15] with the two Co/Cr ratios used in this work highlighted. In both cases the system is still above the liquidus before the quench temperature (1500°C) 55

Figure 26 – Example of how hBN crystal area measured with ImageJ. Crystal is from a Ni-Cr solvent with 4.0 mass% boron. 58

Figure 27 – a) Nitrogen solubility in the ternary Ni-Co-Cr system, vertical axis shows the nitrogen solubility versus composition at 1600°C and 1 bar. X and Y values calculated with Equations 3 & 4. b) Nitrogen solubility in Ni-Cr raised to the 0.2 power to linearize it. c)

Extrapolated nitrogen solubility curve for the binary Co-Cr system with the solubility of the two solvents tested in this work (1/1 and 43/57) highlighted. 59

Figure 28 – Optimal boron concentration for each solvent plotted versus their nitrogen solubilities. Vertical error bars represent the estimated error in the optimal boron concentration of each solvent and horizontal error bars on Co-Cr points represent error in extrapolating their nitrogen solubilities from data in the Ni-Co-Cr system. 61

Figure 29 – Optical micrographs of the largest crystals produced in each of the five solvents tested in this work: Fe (a), Cu (b), Fe-V (c), Ni-Cr (d), and Co-Cr (e). f) Maximum crystal area plotted versus the nitrogen solubility of each solvent. 62

Figure 30 – a) Illustration of thickness of free-standing hBN flake measured with a surface profilometer, which drags a needle off the edge of a flake and measures the drop of the needle with a laser. b) Illustration of thickness of as-grown hBN flake measured with an optical microscope, which was focused on the top and bottom of the transparent crystals so the change in height of the stage measures thickness. c) Thickness of free standing hBN flakes as measured by both a surface profilometer and an optical microscope and as-grown hBN flakes as measured by an optical microscope from the same crystal growth experiment. d) Distribution of thickness of hBN grown from four different solvents shown with boxplots. Horizontal position of the boxplots determined by the nitrogen solubility of each solvent and the dotted line shows the trend of increasing thickness with increasing nitrogen solubility. 64

Figure 31 – a & b) Optical micrographs of hBN single crystals grown from a pure Cu solvent. c) SEM image of a Cu-grown hBN single crystal with wrinkles. d) Average cathodoluminescence spectrum of region shown in c) that shows peaks characteristic of hBN. ... 67

Figure 32 – Illustration of pathways that nitrogen can take to grow hBN single crystals. 1) Nitrogen dissolves into the solvent at the gas-liquid interface and immediately reacts with boron to grow hBN layers near the surface. 2) Nitrogen dissolves into the solvent and diffuses into the bulk where it reacts with boron to grow hBN layers far from the surface or nucleate new hBN layers. 69

Figure 33 – Carbon and oxygen impurity content in source materials (a) and ingots (b and c). Expected impurity concentrations calculated by summing the carbon and oxygen concentrations from the source materials used to make them, scaled by their relative amounts. 73

Figure 34 - Comparison of a UV-PL spectrum (left) acquired with 196 nm excitation at 9K and a CL spectrum (right) acquired at room temperature with an acceleration voltage of 10 kV. Both techniques show emission in the same basic spectral regions across the entire UV-Vis range: phonon replicas (blue), stacking faults/dislocations (green) and point defects/color centers (red)..... 76

Figure 35 – Example of how a hyperspectral CL map is denoised using SVD decomposition. Top left – Averaged CL map of original data, with the central pixel highlighted in red. Top right – CL spectrum at that pixel. Middle right – First 6 components of SVD decomposition on the original CL map. Middle left – Scree plot of the explained variance versus the component index. The elbow point is the point furthest from a line connecting the first and last components and represents the last significant component. Bottom left – Averaged CL map of denoised data calculated by summing all the SVD components up to the elbow point, with the central pixel highlighted in red. Bottom Right – Denoised CL spectrum at that pixel..... 78

Figure 36 – Example of Non-Negative Matrix Factorization (NMF) and Blind Source Separation (BSS) performed on the data presented in Figure 35. The number of components here were set equal to the elbow point from SVD..... 80

Figure 37 – Three examples of spots observed in hBN crystals using CL spectroscopy. Each example is shown with an SEM image (left), a CL map within a selected range (middle), and the average CL spectrum of the imaged region with the selected range highlighted (right) a) Steps on the edge of a crystal that exhibited faint spots near 320 nm. b) Mostly smooth region that showed two spots – the larger had increased emission across the entire wavelength range and the smaller only emitted in a narrow band near 440 nm. c) A smooth region that showed many small spots speckled across the entire area that emitted in the range 425-480 nm..... 81

Figure 38 – Examples of wrinkles in hBN crystals. a) Optical micrograph of an hBN flake containing many wrinkles (scale bar is 2 mm). b) High magnification optical micrograph of an equilateral triangle formed by wrinkles (scale bar is 100 μm). c) SEM image of an intersection of 3 wrinkles (scale bar is 1 μm)..... 83

Figure 39 – TEM images of cross-sectional samples cut from wrinkles using FIB a) TEM image of a cross-sectional sample of a wrinkle with crystallographic directions highlighted. b) Diffraction pattern of sample shown in a that indicates three highly-crystalline regions are present. Red, blue, and green lines highlight the three lattice orientations present in the sample. c) TEM image of the boundary between two of the crystal domains shown in d, with inset highlighting its lattice structure. d) STEM image of another cross-sectional sample cut from a wrinkle using FIB. 84

Figure 40 – Result of a combination of Non-Negative Matrix Factorization and Independent Component Analysis on an intersection of three wrinkles. Top) – Average CL

spectrum and map prior to analysis. Middle) – Component showing emission unique to wrinkles isolated from data. Bottom) – Component showing emission representative of the base material.

The sum of the two components recreates the average spectra in the top figure..... 86

Figure 41 – Examples of CL maps that showed “invisible lines”. Each row is data from a selected sample and the first image in each row is an SEM image of the region mapped. The middle three columns are bandpass images created by summing the CL emission within a range of wavelengths. The right column is the average CL spectrum from each map with the bands used to create each bandpass image highlighted..... 87

Figure 42 - Optical image of hBN crystal on a perforated SiN membrane (a), SEM image (b), and CL bandpass image (c) of one region on this crystal showing a small wrinkle and invisible lines emitting in the range 219-248 nm. d) In-plane TEM image and diffraction pattern (inset) of another region showing local strain along thin lines. e) Diagram of an inserted plane in hBN..... 88

Figure 43 – a) Example of a Raman E_{2g} peak from an hBN sample generated in this work and b) boxplots of the range of Raman E_{2g} peak widths of samples grown from four different solvents. 90

Figure 44 – a) Example of a hBN PL spectrum normalized by its TO Phonon Line. The normalized intensity at 5.47 eV correlates to the relative abundance of stacking faults and the normalized intensity at 4.16 eV correlates to the relative abundance of point defects. These intensities from several samples grown from each solvent (Fe, Fe-V, Co-Cr, and Ni-Cr) are shown for point defects (b) and stacking faults (c). Dashed lines are the average intensities from each solvent..... 91

Figure 45 - a) CL spectrum fit with 6 gaussian peaks - two for optical and acoustic phonon replicas and 4 for defect emission. b) Example of a region manually selected for comparisons. Obvious defects like wrinkles, cracks, and folds were avoided to be more representative of the material in general. c) Box plots showing the range of the integrated intensity within the range 265-650 nm (representing point defects) for hBN samples grown from each solvent. d) Box plots showing the range of the integrated intensity within the range 200-265 nm (representing stacking faults) for hBN samples grown from each solvent. 93

Figure 46 – Temperature profile of two-part process used to produce isotopically-controlled hBN crystals. In the first part (dashed line), the system is heated and dwelled at 1550°C under an Ar/H₂ atmosphere to form a homogenous ingot. In the second part (solid line), the system is heated to 1550°C and slowly cooled under a ¹⁵N₂/H₂ atmosphere to precipitate hB¹⁵N crystals. 101

Figure 47 – Micrograph of a h¹⁰B¹⁵N single crystal mechanically exfoliated from a solidified ingot. 101

Figure 48 – Image of the surface of the Ni-Cr-B ingot after an experiment with hB¹⁵N single crystals on its surface. 101

Figure 49 – High-energy Raman mode (E_{2g}^{high}) from hBN synthesized with different isotope combinations. a) Normalized peak for each isotope combination. b) Raman shift of each sample plotted versus its reduced mass. 103

Figure 50 - Low-energy Raman mode (E_{2g}^{low}) from hBN synthesized with different isotope combinations. a) Normalized peak for each isotope combination. b) Evolution of the low energy Raman active mode versus the high energy one, which indicates the delicate dependences of the phonon modes with isotopic composition. 104

Figure 51 – Phonon dispersion relations in the four hBN isotopically purified samples. Left-hand side are zoomed the energy regions corresponding to the E_{2g}^{low} (bottom) and E_{2g}^{high} (top) phonons at G. Right-hand side are zoomed the energy regions corresponding to the (TA,LA) couple (bottom) and (TO,LO) couple (top) of phonon at the T point of the Brillouin Zone. 105

Figure 52 – a) Normalized photoluminescence spectra from hBN synthesized from different isotope combinations. b) Energy of the fundamental indirect exciton of each sample plotted versus its reduced mass. 107

List of Tables

Table 1 – Masses of components used in CALPHAD simulations.	38
Table 2 – Composition of solution at the start of each boron optimization experiment with an Fe solvent	42
Table 3 – Composition of experiments to test effect of solvents	57
Table 4 – Optimal Boron Concentrations for solvents used in this work and their nitrogen solubilities.	58
Table 5 – Vendors and rated purity of source materials used in experiments.	72
Table 6 – Composition of source materials in ingots tested with chemical analysis.	73

Acknowledgements

I am deeply grateful to my major professor, Dr. James Edgar, whose expertise, advice, and patience has been invaluable to every aspect of my PhD program. Your support has been instrumental in helping me become the researcher I am today. Thank you as well to my supervisory committee, Dr. John Schlup, Dr. Bin Liu, and Dr. Suprem Das for your advice at key moments throughout my program. Furthermore, thank you to Dr. Ursula Kattner at for teaching me how to properly use the CALPHAD method to study multicomponent systems, and to Dr. Shaul Aloni at the Molecular Foundry for teaching me how to operate a cathodoluminescence system, perform complex data analysis on hyperspectral data using Python programming, and providing invaluable guidance on how to explain that information.

In addition, much of the data presented in this work was collected by collaborators around the world, who also provided advice on how to analyze and comprehend it. Raman data was collected by Dr. Rui He and Gaihua Ye at Texas Tech University. Photoluminescence data was collected by Dr. Bernard Gil, Dr. Guillaume Cassabois, and Adrien Rousseau at the Université de Montpellier in France. Transmission electron microscopy images and samples created with focused ion beam milling were produced by Dr. Shaul Aloni at the Molecular Foundry at LBNL and Dr. Elisabeth Mansfield and Dr. Jason Holm at NIST in Boulder, CO. Thank you for your help, this work would be incomplete without the data you provided.

Finally, a special thank you to my family, who have provided unwavering support throughout many personal struggles I've faced over the past several years. I could not have done this without you.

Chapter 1 - Introduction

This dissertation is centered on optimizing hexagonal boron nitride (hBN) crystal growth from solutions, maximizing their size and minimizing their defect densities. Doing this will expand the wide range of device applications that are enabled by hBN's unique properties (Section 1.1). The solution growth method provides a reliable way to grow crystals of the size and quality necessary for these devices but comes with many process variables that must be optimized (Section 1.2). Research into this process has been ongoing for at least 40 years and many advances have been made throughout that time (Section 1.3). The basic crystal growth process used in this work (Section 1.4) is based on the best results from those prior studies. This work builds on that by exploring the effects of the solution composition on the size and quality of hBN crystals grown from it.

1.1 Properties and Applications of hBN Single Crystals

For most of its history, hBN has been valued for its physical properties [1]. It has very high thermal and chemical stability, so it is frequently used as a refractory material in high temperature manufacturing and research. It is nontoxic, so it has been incorporated into cosmetics as a whitening agent. It is also comprised of layers that slide easily past one another, making it useful as a high temperature dry lubricant. These properties continue to be valuable in more modern applications, where hBN's unique electrical and optical properties are especially relevant.

As a single crystal, hBN is a wide bandgap semiconductor and 2D material. While bulk hBN was initially thought to have a direct bandgap [2], it is actually an indirect bandgap with an energy of ~ 6.0 eV and a highly efficient exciton-phonon interaction [3]. Its structure is similar to that of graphite and graphene as shown in Figure 1. Each layer forms a honeycomb structure

with alternating boron and nitrogen atoms and between each layer the atoms alternate as well in an AA' stacking structure, though other stacking structures are possible [4].

Due to these properties, bulk single crystals of hBN have uses in a wide variety of electronic, photonic, and optoelectronic devices listed below. Each of these applications require large, high-quality hBN single crystals as opposed to the powders used in industrial applications. Therefore, processes like those presented in this work are necessary to make those applications possible.

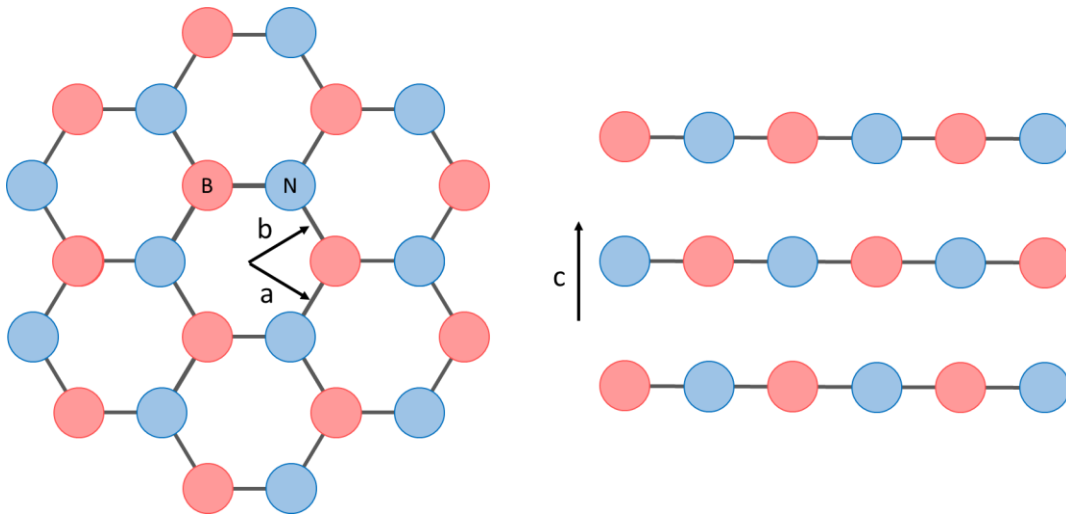
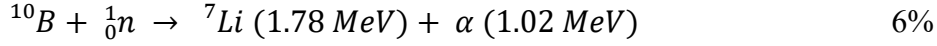
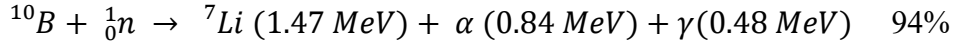


Figure 1 – Diagram of the atomic structure of hBN showing the in-plane honeycomb structure (left) and the alternating AA' stacking structure between planes (right) with a, b, and c directions labeled.

Neutron Detectors

A unique capability of hBN is for neutron detectors, which could have a much higher efficiency than existing options. Neutron detectors have many applications such as material analysis research, metrology, nuclear energy, nuclear decommissioning, and homeland security [5]. Currently, the most common neutron detectors use ^3He as the neutron-sensitive material, but the global supply of ^3He is steadily diminishing due to a reduction in nuclear weapons [6]. In contrast, the ^{10}B isotope is abundant and has one of the highest thermal neutron capture cross sections of any element (3840 barns) [7].

When a ^{10}B atom captures a neutron, it splits into ^7Li , an alpha particle, and a gamma particle according to the following reactions:



The electron-hole pairs created by inelastic scattering of the energetic ^7Li and α particles moving through the material can be efficiently collected in the single-crystalline structure of hBN, leading to a detection efficiency of $\sim 88.6\%$, in contrast with the low detection efficiency ($< 5\%$) obtained with ^{10}B -coated devices [8]. For devices made with monoisotopic $h^{10}\text{BN}$, thick crystals ($\sim 90 \mu\text{m}$) are needed to capture all of the incident neutrons and maximize efficiency [9].

Substrate for 2D Materials and 2D Heterostructures

The atomically smooth surface of hBN with no dangling bonds, its high chemical and physical stability, and its large bandgap make it an ideal substrate for many 2D materials. Zhang *et al.* [10] grew WSe_2 via epitaxy on a hBN substrate, showing that vacancies in hBN trap W atoms and reduce the formation of WSe_2 . Ge *et al.* [11] grew graphene nanoflakes via epitaxy inside holes etched into an hBN substrate such that the graphene was bonded to the etched hBN plane. The zig-zag edge where the two materials met exhibited very high magnetism, which is highly desirable for graphene spintronics. Wang *et al.* [12] fabricated graphene devices encapsulated with hBN, which exhibited ballistic transport of electrons over $>15 \mu\text{m}$. In addition, Woessner *et al.* [13] showed that hBN encapsulation of graphene dramatically decreases the plasmon scattering in graphene, which will significantly improve nanophotonic and optoelectronic devices based on graphene. Lee *et al.* [14] fabricated transparent, flexible field-effect transistors based on a 2D heterostructure of hBN, MoS_2 , and graphene that had a high field effect mobility ($45 \text{ cm}^2/\text{V s}$) and a low operating voltage ($<10\text{V}$).

UV Emitter

Even though hBN is an indirect bandgap, its luminescence efficiency is very high based on the short lifetime of excitons in the material (27 ns) [15], which makes it an excellent candidate for ultraviolet emitters. UV emitters can be used in a wide variety of applications including water and air sterilization, photocatalysis, and UV curing. Watanabe *et al* [16] fabricated a far ultraviolet (225 nm) plane-emission device with hBN powder that had a power output of 0.2 mW using only the power provided by standard AA batteries. These could be used in a wide range of applications including photocatalysis, sterilization, and modification of chemical substances.

Nanophotonics

Grudin *et al* [17] showed that hBN has a very high refractive index, broad birefringence, and low optical losses compared to similar materials, which makes it an excellent material for nanophotonics. Caldwell *et al* [18] reported that hBN is a low-loss, mid-infrared, natural hyperbolic material, which allows sub-diffractive guided waves to be confined in all three dimensions. Dai *et al* [19] showed that the phonon-polariton resonance in hBN can be tuned by the number of layers.

Single Photon Emitters

Single photon emitters in crystals are point defects that emit one photon at a time. Grosso *et al* [20] demonstrated that the emission energy of single photon emitters at room temperature in hBN could be reversibly tuned to ± 6 meV by stressing the material and that they were stable enough to be transferred to other substrates. These properties make it highly desirable for quantum information processing devices.

Twistronics

Twistronics are a new class of devices that are fabricated by twisting one layer of a 2D material with respect to another, which creates moiré patterns and can affect its electronic, optical, and magnetic properties. Su *et al* [21] demonstrated that color centers at a twisted hBN interface could be precisely controlled, which could enable their use in quantum information technologies. Yasuda *et al* [22] and Woods *et al* [23] demonstrated that twisted bilayer hBN exhibited ferroelectric properties at room temperature and atomic thickness, which has applications in nonvolatile memories, high-permittivity dielectrics, electromechanical actuators, and pyroelectric sensors.

Heat Management

The high thermal conductivity hBN makes it promising for heat management in 2D devices and its electrically insulative nature means it won't short any electrical connections. Wang *et al.* [24] fabricated a reduced graphene oxide-based device with polycrystalline hBN-coated glass as a substrate. The high in-plane conductivity (14 W/m K) carried heat away from its source while the low cross-plane conductivity (0.4 W/m K) prevented the formation of a hot spot directly under the device. The thermal conductivity could be increased further by using monoisotopic $h^{10}\text{BN}$ single crystals, which have an in-plane conductivity of 585 W/m K and a cross-plane conductivity of 3.5 W/m K [25].

1.2 Basics of Solution Growth Method

The solution growth method uses a solvent to dissolve both boron and nitrogen so that they can react with each other and precipitate as hBN. This reaction could, in theory, take place without a solvent, but it would be impractical in practice because hBN melts incongruently at a very high temperature (2142°C [26]). Deposition techniques such as chemical vapor deposition,

but they form thin films that are typically hindered by the lattice mismatch between hBN and the substrate.

Solution growth has four basic steps: saturation, supersaturation, nucleation, and crystal growth. During saturation, boron and nitrogen dissolve into the solution until their solubility limits are reached. In the supersaturation step, the state of the system is changed such that the concentration of B and N increases or their solubility decreases, causing precipitation of hBN to be thermodynamically favorable. While the solution is supersaturated, hBN crystals will nucleate, then grow until the solution is no longer supersaturated. This section details the factors that influence each of these steps and how they inform how the process should be optimized.

1.2.1 Solubility and Saturation

Every hBN solution growth experiment starts by saturating the solvent with boron and nitrogen. So long as the solvent is exposed to sufficient boron and nitrogen sources, the system will naturally approach saturation due to being in a non-equilibrium state. The concentrations at which this will occur depend on the solubility of boron and nitrogen in the solvent.

The solubility of boron in these systems is simply the liquidus curve on boron-solvent phase diagrams. For example, the Fe-B phase diagram [27] is shown in Figure 2 where the red line highlights the boron solubility in liquid Fe. At the maximum temperature used in this work (1550°C, see Section 1.4), the boron solubility in Fe is ~12 mass%.

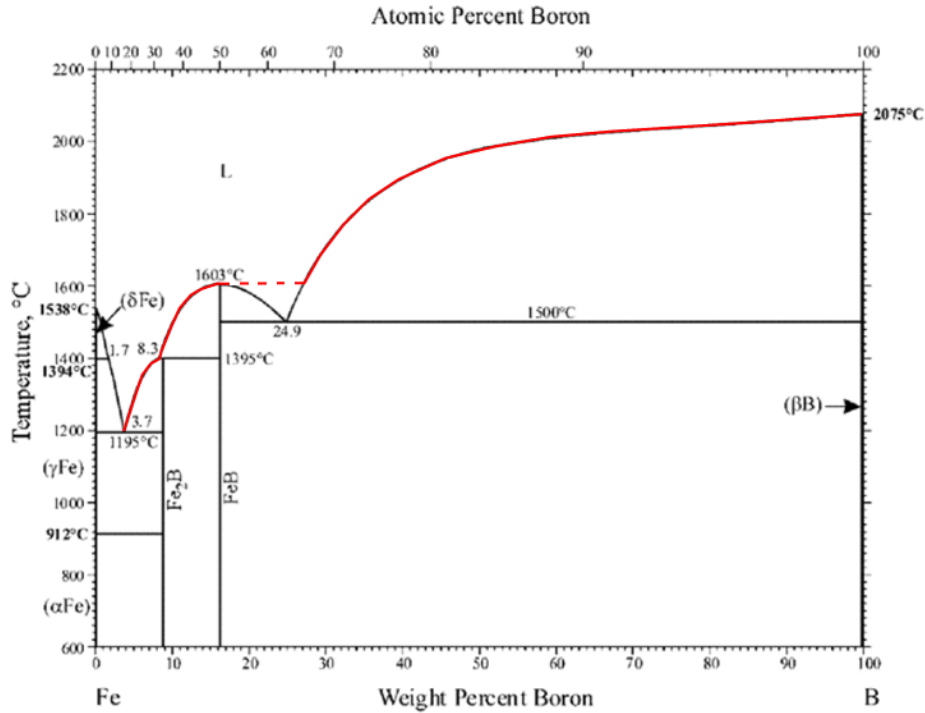


Figure 2 – Fe-B phase diagram with the sections of the liquidus that represent the maximum boron concentration that can be dissolved at a given temperature highlighted in red. [27]

The solubility of molecular nitrogen in the molten metals typically used as solvents is governed by Sievert’s Law, which assumes that N₂ splits into atomic species upon dissolving.

The equation for Sievert’s Law takes the form

$$K_S = \frac{x_N}{P_{N_2}^{1/2}}$$

Where x_N is the solubility of nitrogen as a mole fraction, P_{N_2} is the partial pressure of N₂ in the gas, and K_S is the Sievert’s constant, which is a function of temperature and the solvent composition. This indicates a few different ways to increase nitrogen solubility. First, a solvent can be chosen that has a higher nitrogen solubility in general. A quick rule of thumb is that, within the transition metals, the further left you go on the periodic table, the higher the nitrogen solubility of the element.

Second, the pressure of the system can be increased. All else held constant, the nitrogen solubility will increase by a factor equal to the square root of the increase in pressure. For example, if pressure is increased by a factor of 4, nitrogen solubility will increase by a factor of 2. In crystal growth systems where the pressure can be easily controlled, this provides a very straightforward way to increase the nitrogen solubility, and thus the concentration of nitrogen in solution.

Third, the temperature of the system will change the nitrogen solubility, either increasing or decreasing it depending on the solvent being used and its composition. For example, Figure 3 shows how nitrogen solubility increases with temperature in pure iron but decreases with temperature when the solvent is at least 6.5 wt% chromium [28]. Molten Ni-Cr alloys also have similar trends [29], but pure Fe, Fe-Cr, and Ni-Cr have all been used as solvents for hBN solution growth very successfully (see Section 1.3), so the trend of nitrogen solubility versus temperature does not appear to be critical for the functioning of a solvent in this process.

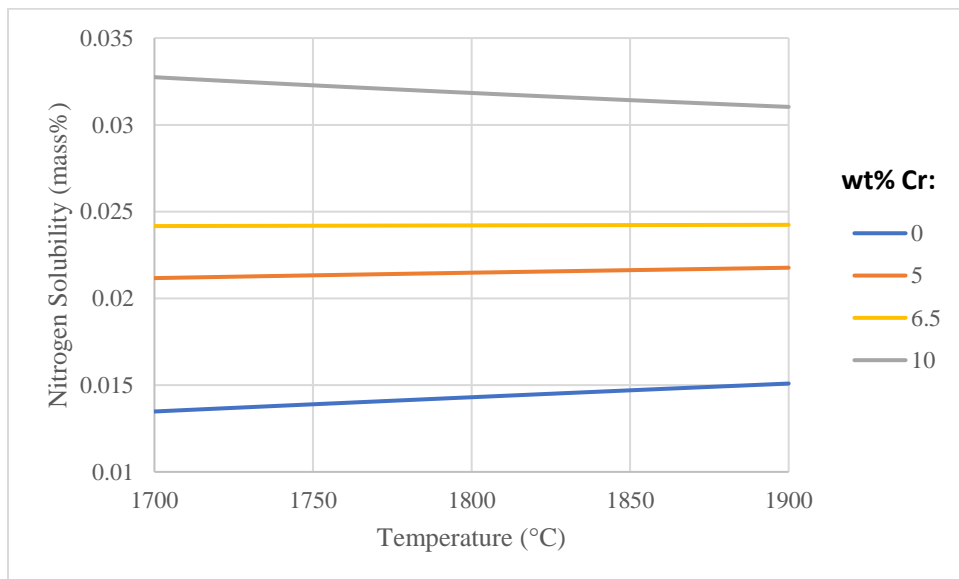


Figure 3 – Solubility of nitrogen versus temperature in molten Fe-Cr alloys at varying chromium concentrations. Curves based on model parameters given in [28]. Changing the concentration of chromium changes the slope and magnitude of nitrogen solubility curve.

Complicating matters is that the presence of boron in the solution affects the solubility of nitrogen and vice versa. Evans and Pehlke [30] studied the nitrogen solubility in an Fe-B system, which gives insights into how boron and nitrogen interact while dissolved in a solvent. They demonstrated that increasing the boron concentration in the solution decreased its nitrogen solubility, even in the absence of hBN formation.

Regardless, the greater question is what conditions are required to cause hBN to start precipitating. This can be difficult to predict because it requires phase equilibria data for the 3+ component systems used for hBN solution growth, and that data is often scarce. Fortunately, in this work, a procedure was developed to predict the liquidus of hBN in an arbitrary solvent using the CALPHAD Method (see Section 2.1). As with boron solubility, the hBN liquidus defines the solubility curve of hBN. Thus, this curve can reveal when the solution is saturated or supersaturated.

1.2.2 Methods of Supersaturation

Once the solution has become saturated, the state of the system must be shifted to cause the solution to become supersaturated so that hBN will precipitate. This can be accomplished with a few different methods: slow cooling, temperature gradient, or solvent evaporation. Each of these have different parameters that dictate how crystal growth will progress.

In the solvent evaporation method, the temperature is held constant and the solvent is allowed to evaporate, leaving boron behind and causing the solution to supersaturate. For this to be a practical method for crystal growth, the evaporation rate of the solvent needs to be high, which requires either a volatile solvent or extreme temperatures. A few works have grown hBN with this method [31]–[33], but with the exception of Ishii and Sato [31] (see Section 1.3.2), the size and quality of hBN grown with this method have been poor.

In the temperature gradient method, a temperature gradient is imposed along the length of the solution to drive crystal growth, as illustrated in Figure 4b. In this setup, supersaturation is maintained through a balance between diffusion and crystal growth. The temperature gradient produces a gradient in the solubility of hBN, which increases with increasing temperature. More boron and nitrogen will dissolve on the hot side than the cold side, which introduces a concentration gradient in the same direction as the temperature gradient. This, in turn, provides a driving force for boron and nitrogen mass transfer from the hot to the cold side, producing a supersaturated solution in the cooler region that causes hBN crystals to precipitate. This process persists because the concentration gradient is maintained through the continuous removal of boron and nitrogen on the cold side (due to crystal growth) and addition of these components on the hot side (due to solvation of the source material). The key parameters in this method are the temperatures of the hot and cold side and the temperature gradient between them.

In the slow cooling method, the entire system is cooled uniformly, which decreases the solubility and causes any B and N in excess of the saturation limit to precipitate as hBN (Figure 4c). The key parameters in this method are the starting temperature, the quench temperature (the temperature at which slow cooling ends and the system is brought back to room temperature), and the cooling rate. The cooling rate is largely responsible for the degree of supersaturation, and thus the nucleation and growth rate, because it defines how quickly the state of the system is changing. Since crystals grown with this method form over a range of temperatures, the crystals grown with it could precipitate with a range of crystal qualities based on the temperature at which they formed.

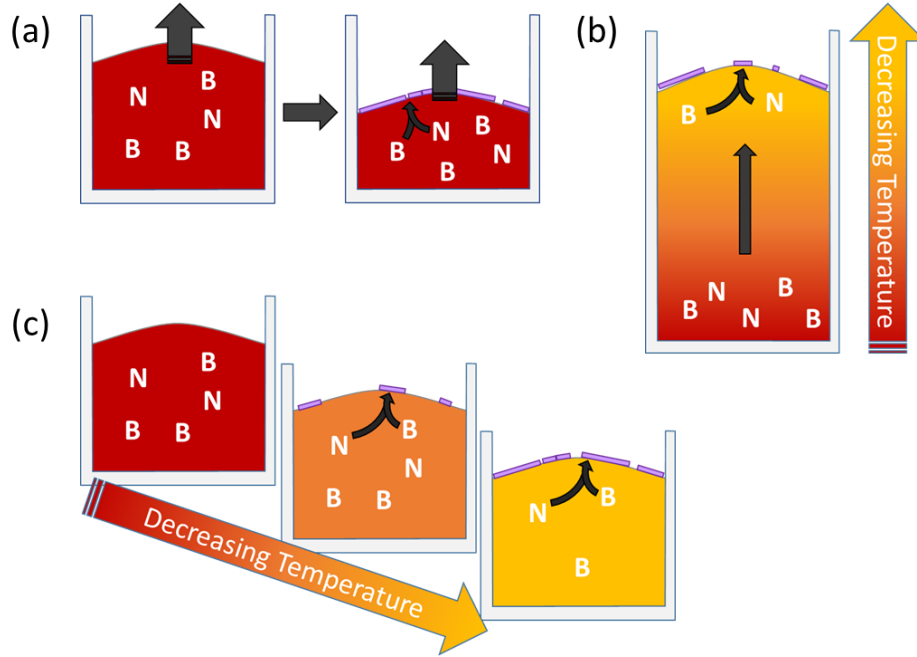


Figure 4 – a) Schematic of solvent evaporation method. As the solvent evaporates, boron is left behind, which causes the solution to become supersaturated so that hBN precipitates. b) Schematic of temperature gradient method. Concentration gradient causes B & N to diffuse to cold side, where hBN precipitates due to lower solubility. c) Schematic of slow cooling method. As temperature decreases, solubility decreases and any excess B & N precipitates as hBN.

1.2.3 Nucleation and Crystal Growth

To produce large single hBN crystals, the nucleation rate should be much slower than the crystal growth rate. Ideally, only one crystal will nucleate and grow to fill the entire region available to it. The kinetics of nucleation in hBN solution growth has not been explicitly studied, but Lacmann, Herden, and Mayer [34] showed that the rate of homogeneous nucleation (J) for crystals in general is given by the expression,

$$J \propto e^{-\Delta G/k_B T}$$

Where k_B is the Boltzmann constant, T is the absolute temperature, and ΔG is the Gibbs free energy of nucleation, which is given by the expression,

$$\Delta G \propto \frac{\gamma^3}{(\Delta c/c_s)^2}$$

Where γ is the surface energy between the crystal and the solution, c_S is the solubility of the crystal material in the solvent, and Δc is the supersaturation ($\Delta c = c_{actual} - c_S$).

These equations reveal a few ways to reduce the nucleation rate. First, lowering the temperature reduces nucleation, but that is not a good option because it will also slow crystal growth and mass transport. Increasing the Gibbs free energy of nucleation will also reduce the rate, which can be done by either increasing the surface energy between the crystal and the solution or decreasing the relative supersaturation ($\Delta c/c_S$). The surface energy is difficult to predict and will depend on what solvent is used for crystal growth, so while this does not provide a straightforward strategy to reduce nucleation rate, it does reveal that the choice of solvent will inherently affect it.

The relative supersaturation, on the other hand, can be more easily controlled as is discussed in Section 1.2.2. For example, the relative supersaturation could be reduced by decreasing the cooling rate or the temperature gradient when using the slow cooling method or the temperature gradient method, respectively. However, the fact that supersaturation (Δc) is divided by the solubility (c_S) suggests that increasing the solubility will also decrease the nucleation rate. Furthermore, the slope of the solubility curve versus temperature may play an important role. With a constant cooling rate, a solvent with a steeper solubility versus temperature curve will be supersaturated faster than a solvent with a flatter curve.

1.3 Prior Work on hBN Solution Growth

Solution growth of hBN can be split into three categories: High Pressure High Temperature (HPHT), Atmospheric Pressure High Temperature (APHT), and monoisotopic hBN. HPHT hBN synthesis is widely considered the gold standard for growth of large, high-quality hBN. However, APHT synthesis can frequently produce hBN on par or better than those grown

at HPHT. Monoisotopic hBN is synthesized so that both boron and nitrogen have only one isotope and has only been grown with APHT synthesis to date. The natural isotope distribution of boron is 20% ^{10}B and 80% ^{11}B while the natural isotope distribution of nitrogen is 99.6% ^{14}N and 0.4% ^{15}N (i.e., nearly isotopically pure ^{14}N). Thus, by using a monoisotopic boron source material, monoisotopic hBN can be grown. This section details the advances each hBN solution growth researcher has made in developing these processes.

1.3.1 High Pressure Synthesis

Taniguchi and Watanabe *et al* [2], [35] began research into HPHT synthesis of hBN when it formed as a byproduct of cBN synthesis and they observed that it exhibited UV luminescent properties. They grew these crystals via the temperature gradient method with a barium solvent at high temperature (1500-1750°C) and high pressure (4.0-5.5 GPa) with the temperature gradient method. The crystals grown in these works were 1-6 mm² and were colorless, which indicates low carbon impurities. In later work [36] with the barium solvent, they used SIMS to analyze the carbon and oxygen impurity concentrations in their hBN crystals; both were less than 10^{18} atoms/cm³. An example of an hBN single crystal grown under these conditions is shown in Figure 5a. Kubota *et al* [37] also tested a pure nickel solvent at high temperature (1300-1900°C) and high pressure (4.5-6 GPa). The crystals produced were relatively small (10-25 μm across) and were irregularly shaped, as shown in Figure 5b. The small size may be due to the extremely low solubility of nitrogen in pure nickel, which may inhibit the rate of crystal growth.

Zhigadlo [38] followed up on this work with a magnesium solvent at 1700-2100°C and 1-3 GPa using the temperature gradient method. A drawback of the barium solvent is that it is hygroscopic and oxidizes quickly in air, so it must always be handled in a dry nitrogen atmosphere. Magnesium is more stable and does not require such stringent care to be taken in

handling it, so the author proposes it as a more practical solvent. The best results with this solvent were obtained at 1900-2100°C and 3 GPa, the maximum temperatures and pressure they tested. An image of hBN crystals produced with this solvent is shown in Figure 5c. The success of these parameters could be attributed to the faster kinetics with higher temperatures and increasing nitrogen solubility with higher pressure. These crystals have a similar size to those reported by Watanabe *et al* [35] and produced a Raman E_{2g} peak FWHM of 8 cm^{-1} , which indicates good quality, suggesting this is a viable substitute for barium.

Onodera *et al* [39] discovered that hBN crystals grown with a Ba solvent as described in ref. [36] consistently contained a carbon-rich domain. These domains are invisible in optical and electron microscope images, but visible in cathodoluminescence and photoluminescence images. They are also significantly detrimental to carrier mobility in an adjacent graphene layer as determined by electrical measurements on a hBN-graphene heterostructure. No advice was given on how to eliminate the domain from forming, but their method of detecting them with CL or PL allows carbon-free crystals to be selected before device fabrication.

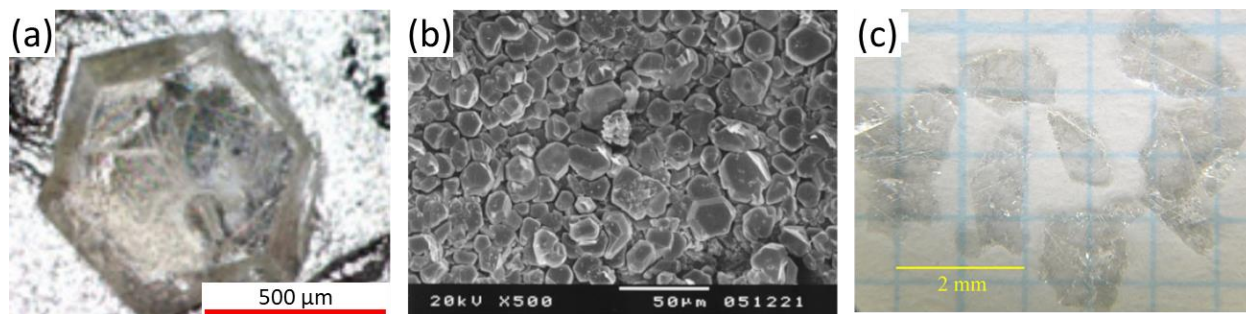


Figure 5 – Examples of hBN crystals grown at high pressure and temperature. a) Optical micrograph of an hBN single crystal grown from a Ba solvent at high temperature (1500-1650°C) and high pressure (4-5 GPa) [36]. b) SEM image of hBN crystals grown from a nickel solvent at 6 GPa and 1600°C [37]. c) Photograph of hBN flakes produced using a magnesium solvent at 3 GPa and 1900-2100°C [38].

1.3.2 Atmospheric Pressure Synthesis

The first reported demonstration of solution growth of bulk hBN single crystals was in 1983 by Ishii and Sato [31], who used a silicon solvent at atmospheric pressure. They were able to produce flakes up to 2 mm across and 20 μm thick as shown in Figure 6. The mechanism for hBN supersaturation and precipitation in their work is unclear, but the authors suggest that evaporation of the solvent could have been the driving force. The extreme temperature (1830°C) and low pressure makes this explanation plausible, but the driving force may also have been the cooling period from 1830°C to 1800°C. Unfortunately, the cooling rate was not specified. It is also unclear if these flakes were single crystals or polycrystalline, but their Raman E_{2g} peak FWHM was 8 cm^{-1} , indicating their quality was relatively good, even by today's standards. However, these crystals had a pale-yellow color, which is indicative of carbon contamination, likely caused by the use of a graphite susceptor in their induction furnace.

A few different researchers tested hBN solution growth at low temperatures (<1000°C) and pressures using a variety of solvents and experimental setups. Ostrovskaya *et al* [32] grew hBN at 650-1450°C from a lithium borate solvent, which was supersaturated by evaporating the solvent. Feigelson, Frazier, and Twigg [40] grew hBN (Figure 6b) with a molten salt ($\text{BaF}_2\text{-Li}_3\text{N}$) as a solvent at 760-900°C under a temperature gradient, following procedures that were successful for growth of other III-nitrides like GaN. Gu *et al* [41] grew hBN (Figure 6c) with a mixture of NaBF_4 , NaNH_2 , and LiBr at 600-700°C, though they did not specify how their solution was supersaturated. In all of these low temperature studies, the width of hBN single crystals were very small (<10 μm) or their crystal quality was poor (Raman E_{2g}^{high} peak FWHM >10 cm^{-1}).

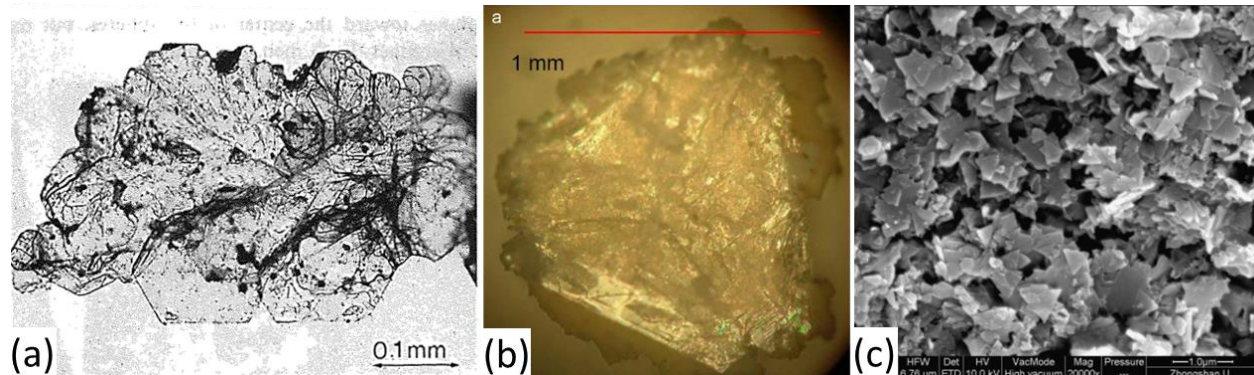


Figure 6 – a) Large hBN flake produced by Ishii and Sato [31] in a Si solvent at 1850°C. b) Large single crystal grown from molten $\text{BaF}_2\text{-Li}_3\text{N}$ salt at 820°C by Feigelson, Frazier, and Twigg [40]. c) Crystals grown from a mixture of NaBF_4 , NaNH_2 , and LiBr at 650°C by Gu et al [41]

Kubota *et al* [42], following their success with high pressure synthesis of hBN and the success of Ishii and Sato [31] at atmospheric pressure, developed the slow cooling method for hBN solution growth at atmospheric pressure. To grow crystals, they cooled the system from 1350-1500°C to 1200°C at 4°C/hr and tested two different solvents: pure Ni and Ni-Mo. A major conclusion in their work was the importance of the nitrogen solubility of the solvent. Pure nickel has a very low nitrogen solubility and produced crystals that were 300 μm across or less with a thickness of a few microns. Adding Mo significantly increased the nitrogen solubility of the solvent, and crystals grown from Ni-Mo solvents (Figure 7a) were significantly thicker (10 μm) and had a Raman E_{2g} peak FWHM of 9.0 cm^{-1} , which indicates good quality.

In a follow-up to this work, Kubota *et al* [43] tested a Ni-Cr solvent. The addition of Cr enabled crystals (Figure 7b) up to 500 μm across and 60 μm thick to be formed, which they attributed to its much higher nitrogen solubility than Ni-Mo. They also suggest that the optimal starting temperature of the process is near 1430°C since this produced their largest single crystals (Figure 7b).

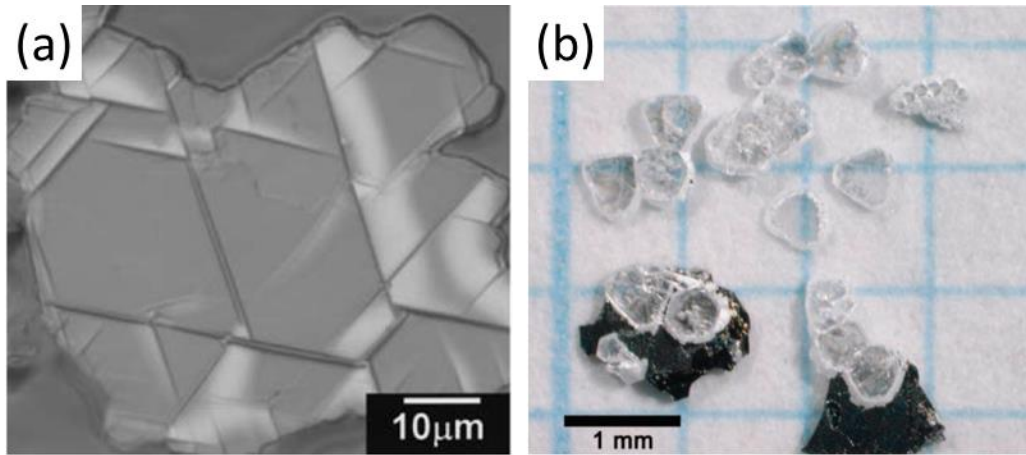


Figure 7 – a) Differential interference microscope image of hBN grown from Ni-Mo solvent at 1400°C [42]. b) Photograph of hBN crystals grown from a Ni-Cr solvent at 1430°C. [43].

The success of the APHT slow cooling method for hBN solution growth developed by Kubota *et al* [42], [43] led many others to build off of this process and improve it. Clubine [44] and Hoffman *et al* [45] studied the effect of the cooling rate and dwell temperature with a Ni-Cr solvent and concluded that the slowest cooling rate (2°C/hr) and highest dwell temperature (1700°C) they tested produced the largest crystals. This was attributed to a reduction in the nucleation rate with decreasing cooling rate and increasing atomic mobility with increasing growth temperature. However, the highest temperature in both works required use of a furnace with a graphite heating element, which may have contaminated the crystals with carbon. The largest crystal produced in these works (Figure 8a) was 5 mm wide with a Raman E_{2g}^{high} peak of 8 cm^{-1} , indicating they were high quality. Clubine [44] also tested pure Ni and pure Cu as solvents, but did not precipitate hBN from them.

Sperber [46] tested a stepped growth process with a Ni-Cr solvent intended to increase the thickness of hBN single crystals without affecting their domain area. In the first step, the solution was slowly cooled from 1410°C to 1394°C at 4°C/hr to grow wide crystals as done in prior work. Then the system was dwelled at that temperature for 24 hours to allow the

established crystals to grow thicker. The crystals were relatively small compared to prior work (~170 μm wide), but their thickness (~17 μm) was large relative to their width, suggesting that both wide and thick crystals could be grown with this process if it were further optimized. Notably, the crystals grown in this way also grew oriented so their a/b direction was perpendicular to the surface of the solvent as shown in Figure 8b.

Liu *et al* [47] compared Ni-Cr to Fe-Cr as a solvent for hBN solution growth because Fe is significantly cheaper than Ni and would make the process more economical. They obtained hBN single crystals that were up to 2 mm wide (Figure 8c) and had a Raman E_{2g}^{high} peak of 7.8 cm^{-1} , indicating that both solvents produce similarly large and high-quality crystals and demonstrating that Fe-Cr will work as a low-cost alternative to Ni-Cr.

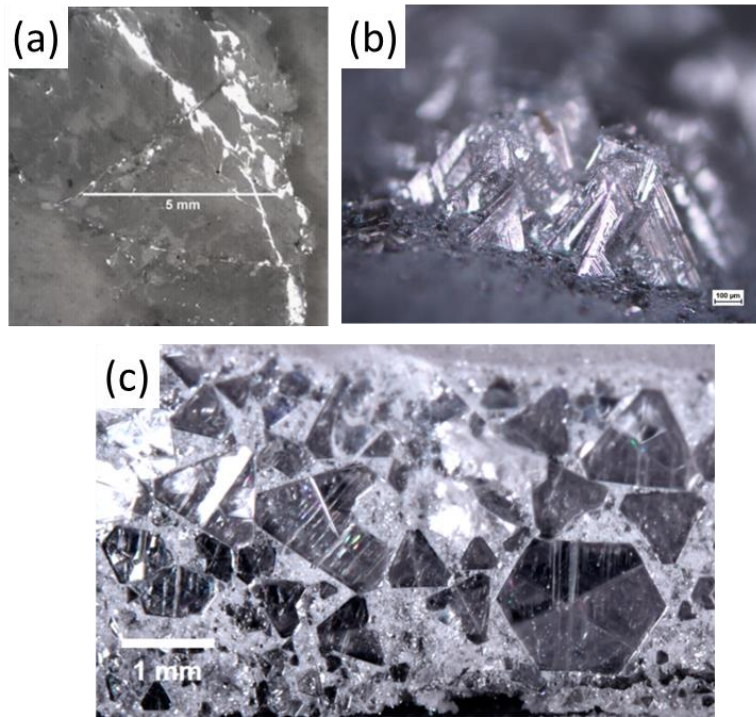


Figure 8 – a) Optical micrograph of 5 mm-wide hBN single crystal grown from a Ni-Cr with a dwell temperature of 1700°C and a cooling rate of 2°C/hr [45]. b) Optical micrograph of hBN crystals grown from Ni-Cr using a stepped growth process to encourage growth in both the a/b and c directions. Crystals tended to form the shape of pyramids with their a/b direction roughly perpendicular to the solvent surface [46]. c) Photograph of large hBN single crystals on the surface of the solidified Fe-Cr flux they were grown from [47].

Zhang *et al* [48] demonstrated that intentionally adding carbon to their Ni-Cr solvent increased the size and yield of hBN crystals, claiming that carbon reduces any residual oxygen in the system that would have otherwise inhibited crystal formation. Their results showed a 10-fold increase in domain size while using carbon concentrations between 1.8 and 6.8 mass% compared to their own results without any added carbon. No carbon was detected in the hBN crystals with EELS, but their largest crystals (Figure 9a) were 200 μm wide while all other researchers that tried Ni-Cr were able to grow crystals larger than 500 μm . Subsequent analysis by Cao *et al* [49] of hBN crystal growth with a Ni/Cr solvent, hBN as the source material, and with the addition of 1.8 mass% carbon, demonstrate that graphite was precipitating where cracks appeared in the hBN crystals. This graphite precipitation was suppressed by adding 0.25 to 4.76 mass% gold, which suppressed the carbon aggregation and produced larger crystals (Figure 9b). The time resolved photoluminescence properties were also improved with the addition of gold.

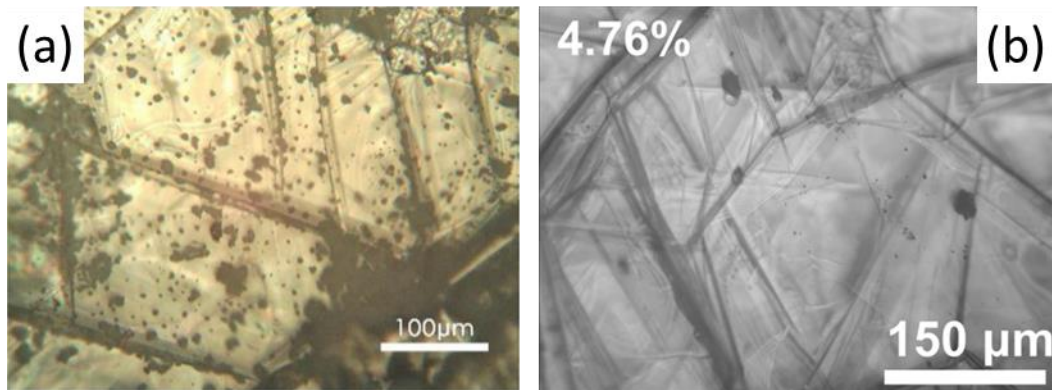


Figure 9 – a) Optical micrograph of hBN grown from a Ni-Cr solvent containing 1.8 mass% carbon [48]. b) Optical micrograph of hBN grown from a Ni-Cr solvent containing 1.8 mass% carbon and 4.76 mass% gold to suppress precipitation of graphite [49].

Li *et al* [50] grew hBN from an Fe-Cr solvent with a process that combined features of the slow cooling and temperature gradient methods. One zone in their horizontal tube furnace was held at 1600°C throughout crystal growth while the temperature of the neighboring zone was steadily dropped from 1600°C to 1400°C at 4°C/hr, creating a temperature gradient across the

solution that gradually increased over the course of the experiment. These crystals were up to 3-4 mm wide (Figure 10a) and had a Raman E_{2g}^{high} peak FWHM of only 7.6 cm^{-1} , the narrowest peak width reported to date using natural isotope distribution boron.

In another work, Li *et al* [51] grew hBN from a pure Fe solvent by slowly cooling from 1550°C to 1450°C at 4°C/hr . Pure Fe has a very low nitrogen solubility compared to other solvents that have been tested for hBN solution growth, but it still produced large, high quality hBN (Raman E_{2g}^{high} peak FWHM of 7.6 cm^{-1}). As shown in Figure 10b, this process also produced a highly-ordered hBN flake $\sim 4 \text{ cm}^2$ in area, one of the largest continuous hBN sheets reported.

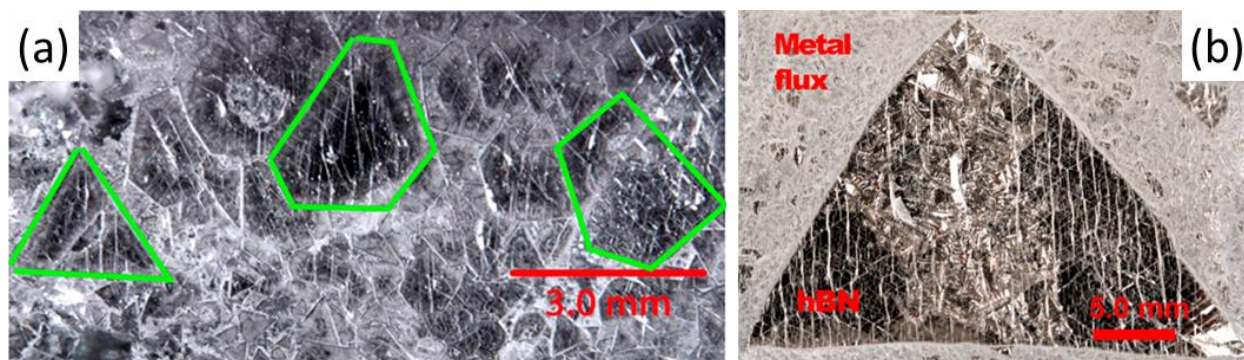


Figure 10- a) Micrograph of hBN on the surface of an Fe-Cr ingot. Green lines outline grain boundaries of three crystals [50]. b) Photograph of hBN single crystal grown from a pure iron solvent on solidified ingot. Triangular hBN sheet is $\sim 4 \text{ cm}^2$ in area. [51]

Onodera *et al* [52] tested Ni-Cr alongside Ni-Mo and Co-Cr. They concluded that Co-Cr was the best of these solvents because it produced crystals with the lowest impurity concentrations. The largest of these flakes were $>180 \mu\text{m}^2$ after exfoliation from the solidified ingot (Figure 11a). These are smaller than those produced from Ni-Cr, but the reason for this is unclear based on the information provided in the article. However, a major conclusion from this work is that the crystals they produced from Co-Cr with an APHT process were free of carbon-rich domains frequently found in crystals grown from Ba in a HPHT process, which were

initially discovered in a prior work [39]. These carbon domains were shown to degrade the carrier mobility of the material, so finding ways to avoid them is important.

Zhang *et al* [53] grew hBN from a Cu-Cr solvent by slow cooling from 1700°C to 1500°C at a rate between 2.5 and 10°C/hr. Copper was chosen as a replacement for Ni because it is much cheaper than Ni and has a very low carbon solubility, potentially reducing the concentration of carbon impurities in hBN grown from it. As in other works testing the effect of the cooling rate, the slowest rate they tested (2.5°C/hr) produced the largest, clearest hBN flakes. These flakes were up to 6 mm wide (Figure 11b) with a Raman E_{2g}^{high} peak FWHM of 9.3 cm^{-1} , which is significantly higher than in other works, indicating that they have worse quality.

Li, Y. *et al* [54], following the success of Li, J. *et al* [51], also studied hBN solution growth in pure Fe by slowly cooling the system from 1550°C to 1450°C at 4°C/hr. They specifically studied how the concentration of boron in the melt (1.5-25.3 at%) affected the size of hBN grown, determining that a boron concentration of 16.2 at% (3.6 mass%) produced the largest crystals (up to 400 μm wide, Figure 11c). These crystals had a Raman E_{2g}^{high} peak FWHM of 7.9 cm^{-1} , which indicates that they have a high crystal quality.

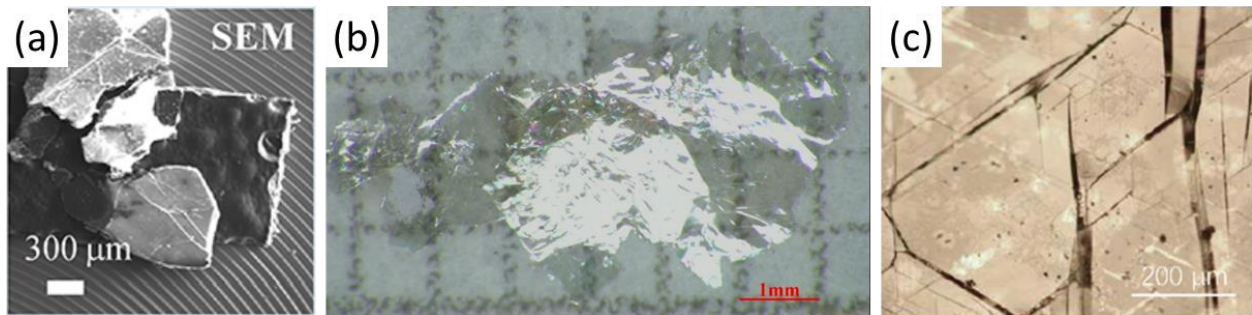


Figure 11 – a) SEM image of free-standing hBN crystal flakes grown from a Co-Cr solvent [52]. b) Photograph of hBN flake grown from a Cu-Cr solvent [53]. c) Optical micrograph of hBN grown with 16.2 at% B in a pure Fe solvent [54].

1.3.3 Synthesis of Monoisotopic hBN

To grow monoisotopic hBN, a hot-pressed boron nitride (HPBN) boat cannot be used as is often done for hBN solution growth because HPBN is only commercially available with the natural isotope distributions. Since HPBN dissolves into the solution during crystal growth, any hBN grown with it will have an unpredictable mixture of isotopes. Therefore, an inert crucible like alumina is required and monoisotopic boron powder is the boron source material. However, this comes with the additional challenge of needing to decide what concentration of boron to add to the solution instead of relying on the solvent's boron solubility and the solvation kinetics of HPBN to control the concentration of boron. Several works have been published that detail how to grow high-quality hBN

Hoffman *et al* [55] was the first to describe how monoisotopic hBN can be grown via the solution growth method. They used a 46.76/ 41.47/ 11.78 mass% Ni/Cr/B solution with isotopically enriched ^{10}B (92.64 at%) or ^{11}B (99.99 at%) as the boron source material, cooling from 1500°C to 1200°C at 2°C/hr. However, they performed the experiment in a HPBN crucible, which diluted the isotopically enriched boron with natural isotope distribution boron. Furthermore, the crystals grown in their work were small (20-30 μm) with wide Raman E_{2g}^{high} peak FWHM (14.1 and 9.4 cm^{-1} for $h^{10}\text{BN}$ and $h^{11}\text{BN}$, respectively), indicating that they had relatively poor quality. In later attempts, Hoffman [56] replaced the HPBN crucible with an alumina one, leaving all else the same, to much greater success. These crystals were much larger (~ 300 μm , Figure 12a) with Raman E_{2g}^{high} peak FWHMs of 3.5 and 3.6 cm^{-1} for $h^{10}\text{BN}$ and $h^{11}\text{BN}$, respectively.

Liu *et al* [57] achieved even better results using a process with a few key differences The starting composition was 48/48/4 mass% Ni/Cr/B, hydrogen was added to the furnace

atmosphere to remove carbon and oxygen impurities from the solution, and the cooling rate was lowered from 4°C/hr to 0.5°C/hr. Crystals grown with this process were up to 1 mm wide (Figure 12b) and had Raman E_{2g}^{high} peak FWHMs of 3.1 and 3.3 cm^{-1} for $h^{10}\text{BN}$ and $h^{11}\text{BN}$, respectively. As with the results of Hoffman [56], these peak widths are dramatically narrower than those produced by any hBN single crystal with a natural boron isotope distribution, which is attributed to eliminating isotopic disorder in the material.

Following this work, Li, J. *et al* [58] grew monoisotopic $h^{10}\text{BN}$ and $h^{11}\text{BN}$ from an Fe-Cr solvent. They used a faster cooling rate, cooling from 1550°C to 1450°C at 4°C/hr, but the basic process was otherwise the same. The largest crystals grown were 1-5 mm across (Figure 12c) and had Raman E_{2g}^{high} peak FWHMs of 3.1 and 2.7 cm^{-1} for $h^{10}\text{BN}$ and $h^{11}\text{BN}$, respectively, indicating that they are larger and slightly higher quality than those produced by Liu [57] with a Ni-Cr solvent..

Li, Y. *et al* [54] grew monoisotopic $h^{10}\text{BN}$ and $h^{11}\text{BN}$ from a pure Fe solvent using the optimal boron concentration they determined in the same work (see previous section). They did not specify the domain size of monoisotopic hBN they grew, but it is likely close to the size of natural isotope distribution hBN they grew (~400 μm). Furthermore, the Raman E_{2g}^{high} peak FWHMs for these crystals were 3.3 and 2.9 cm^{-1} for $h^{10}\text{BN}$ and $h^{11}\text{BN}$, respectively, indicating that they have crystal quality similar to those of Liu *et al* [57] and Li, J.*et al* [58].

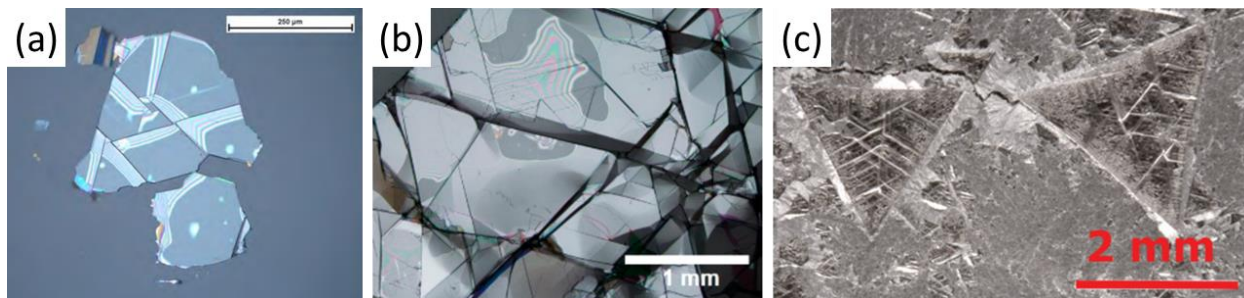


Figure 12 – a) Optical micrograph of $h^{10}\text{BN}$ grown from Ni-Cr with 11.78 mass% ^{10}B by slowly cooling at 4°C/hr [55]. b) Optical micrograph of $h^{10}\text{BN}$ grown from Ni-Cr with 4 mass% ^{10}B by slowly cooling at 0.5°C/hr [57]. c) Optical micrograph of $h^{11}\text{BN}$ grown from Fe-Cr with 3.2 mass% ^{11}B by slowly cooling at 4°C/hr [58].

1.4 Standard Crystal Growth Process

All crystal growth experiments conducted in this study employed a two-step process: ingot formation then crystal growth. Ingot formation was done to thoroughly mix the source materials into a homogenous ingot that was used in the second step. A similar process was done in past work [56] with the goal of precipitating impurities from the solution prior to crystal growth. In that prior study, any material that precipitated during ingot formation was polished off and discarded along with any unincorporated powder. However, in this work, special focus was placed on the composition of the solution, and discarding material would change the composition of the solution by an unpredictable amount.

Thus, ingot formation was modified as shown in Figure 13. Metal and boron powder – the solvent and boron source materials, respectively – were loaded into an alumina crucible and placed into a horizontal tube furnace. An alumina crucible was chosen in place of the hot-pressed boron nitride (HPBN) crucibles used in past work to prevent the boron concentration from changing unpredictably due to solvation of the HPBN crucible [43], [45], [47], [51]. Furthermore, HPBN crucibles cannot be used during synthesis of isotopically pure hBN because they are only available with the natural isotope distributions of B and N. Next, the furnace was

heated to 1550°C at 200°C/hr and held there for 24 hours so all components melted together into a homogenous liquid, then quenched at 200°C/hr back down to room temperature (Figure 13a). Throughout this process, a steady stream of 93/7 Ar/H₂ flowed through the furnace at 270 sccm and 850 torr (Figure 13b). Hydrogen gas is included to react with carbon and oxygen impurities to produce H₂O and CH₄, which are swept from the system.

The only major difference between this process and the ingot formation process described in ref. [56] is flowing argon through the furnace in place of nitrogen. Ingot formation without any nitrogen in the system consistently produced clean, homogenous ingots while ingot formation with nitrogen frequently left undissolved powder in the crucible as shown in Figure 13c. This is likely due to avoiding the formation of hBN or metal nitrides during melting, which may inhibit thorough mixing of the components. In any case, the substitution of nitrogen for argon allows the composition of the solution to be precisely controlled by avoiding the need to discard material.

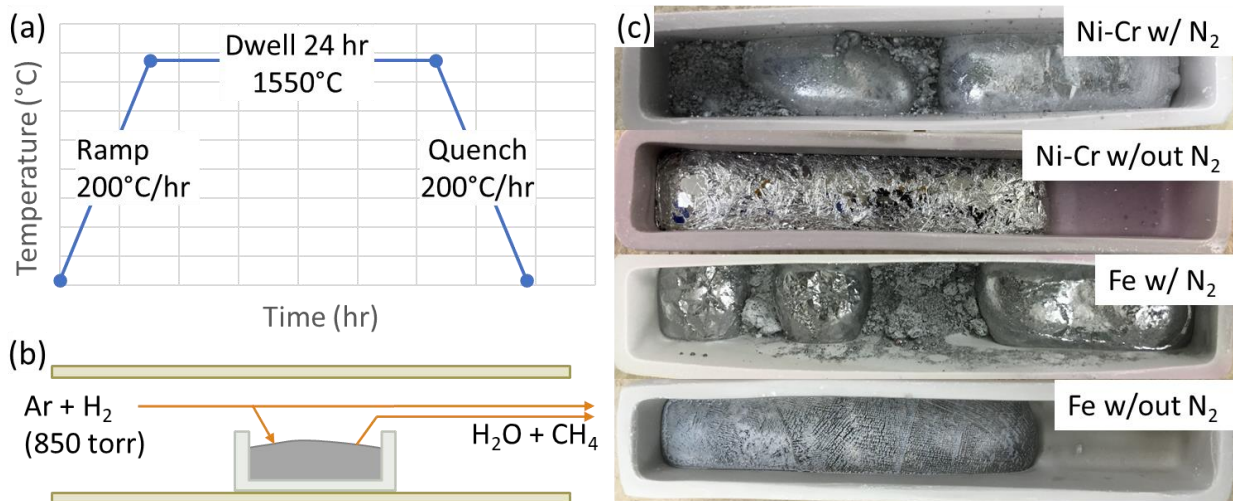


Figure 13 – a) Temperature profile of ingot formation experiments. b) Diagram of experimental setup inside the tube furnace. Hydrogen diluted with argon for safety continuously flowed over crucible to react with carbon and oxygen impurities and sweep them from the system. c) Results of ingot formation with and without N₂ present in the atmosphere for two solvents. Removing nitrogen produced more homogenous ingots.

For the crystal growth step, the ingot formed in the first step was loaded into a horizontal tube furnace again to grow hBN single crystals. Unlike the ingot formation step, nitrogen is introduced into the system by continuously flowing 93/7 N₂/H₂ through the furnace at 270 sccm and 850 torr (Figure 14b). Hydrogen continues to volatilize impurities and remove them from the system while nitrogen dissolves into the solution to react with boron and form hBN. Once the ingot is loaded, the furnace is heated to 1550°C at 200°C/hr and held there for 24 hours to allow nitrogen ample time to saturate the solution, then slowly cooled at 1°C/hr to supersaturate the solution and cause hBN to precipitate (Figure 14a). At 1500°C, the system is quenched at 50°C/hr to 1300°C, then at 100-200°C/hr down to room temperature. The initial slow quench is done to protect the alumina tube from thermal shock, which could crack the tube and ruin an experiment due to oxygen from the air entering the system. Once cooled, the ingot has a layer of hBN crystals covering its entire surface as shown in Figure 14c.

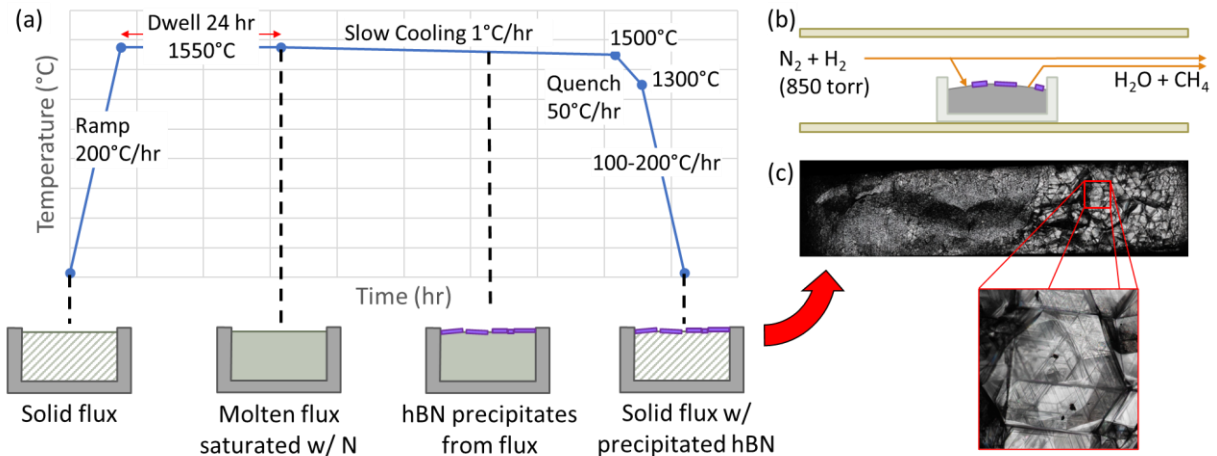


Figure 14 – a) Temperature profile of crystal growth experiments with diagrams illustrating how crystal growth progresses. b) Diagram of experimental setup inside the tube furnace. Nitrogen and hydrogen continuously flowed over crucible. H₂ reacts with carbon and oxygen impurities and sweep them from the system. Nitrogen dissolves into the solvent and reacts with boron to form hBN.

To make use of the crystals grown via this method, they must be removed from the ingot. This was done by mechanical exfoliation of the crystals with thermal release tape as shown in

Figure 15a. Once they are removed from the ingot, they can be removed from the tape by heating it on a hotplate so that it is no longer adhesive, producing free-standing crystals like the one shown in Figure 15b. Unfortunately, this process tends to break crystals, making them thinner and smaller in-plane than they were as-grown.

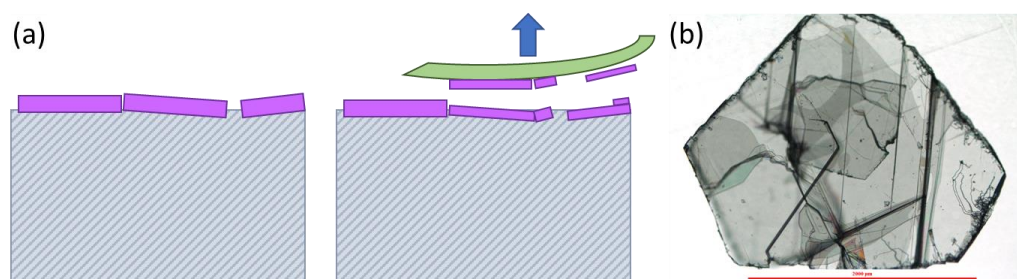


Figure 15 – a) Illustration of how mechanical exfoliation with thermal release tape is done. Some crystals inevitably become broken and are usually cleaved to produce thinner crystals. b) Optical micrograph of an hBN single crystal exfoliated from an ingot.

Ingot formation and crystal growth experiments were each conducted in one of two furnaces shown below in Figure 16 and Figure 17, termed here “Furnace 1” and “Furnace 2”, respectively. Both furnaces are 1600 series single heating zone horizontal tube furnaces from CM Furnaces Inc., though they have a few minor differences. Furnace 2 is mounted on a structure that allows it to be tilted up to 30° forward or back, though this functionality was not used in this work. Furnace 1 has three gas cylinders attached to it: Ultra-high purity (UHP) nitrogen, hydrogen, and argon, all from Matheson Gas. By setting the flowrates on the mass flow controllers (MFC) connected to each cylinder, precise mixtures of the three gases can be achieved. Furnace 1 has two gas cylinders attached to it: UHP nitrogen and a custom 95/5 Ar/H₂ mixture from Matheson Gas. A pure hydrogen cylinder is not attached to this furnace because of fire safety concerns due to it not being in a fume hood. In both furnaces, a butterfly valve is automatically controlled with a pressure controller reading a pressure transducer (covering a pressure range from 1 to 1000 torr) to maintain the pressure at 850 torr in all experiments. A low-

pressure thermocouple gauge (covering a pressure range from 0.001 to 1 torr) measured the pressure during vacuum-purge cycles.

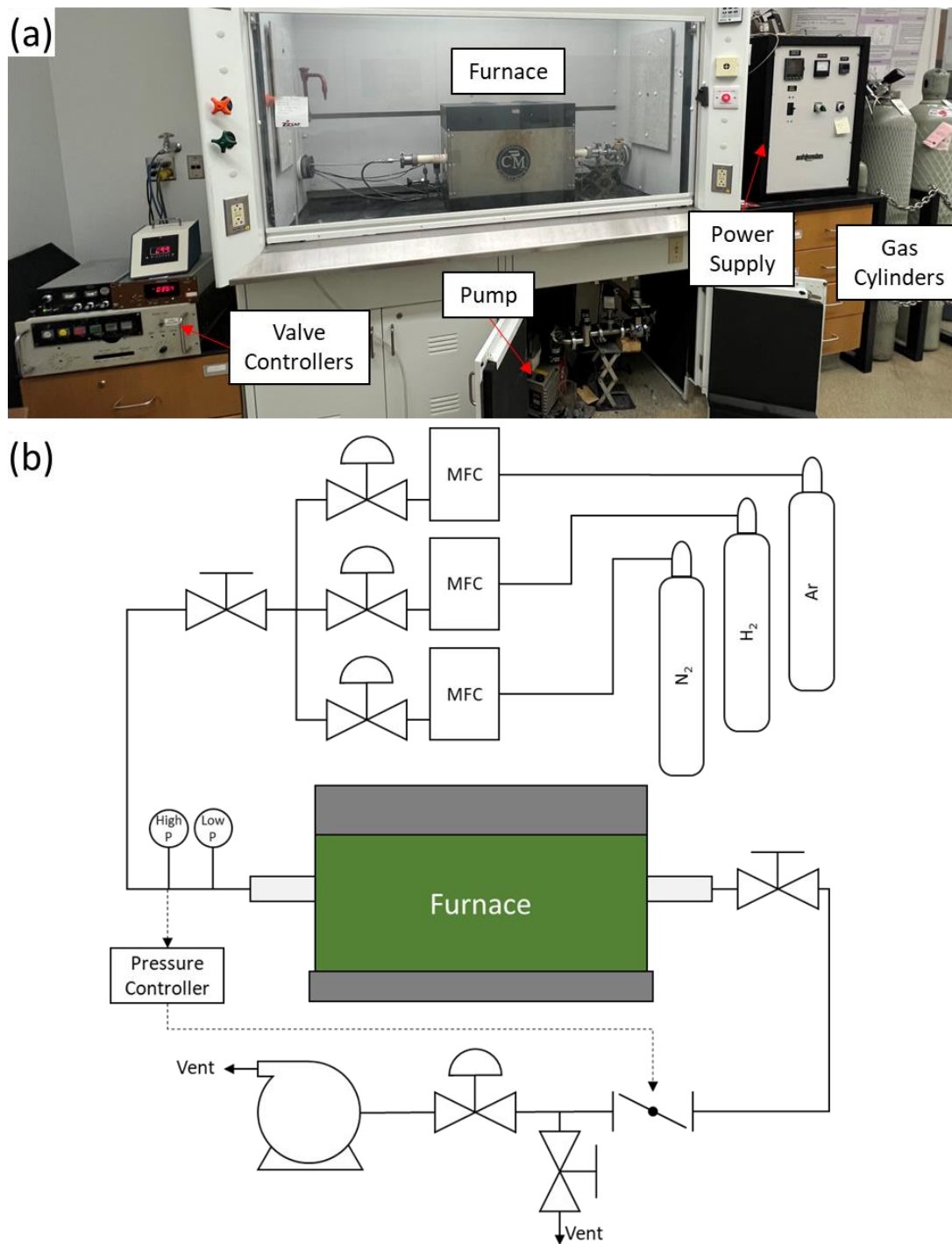


Figure 16 – a) Photograph of furnace 1 with components labeled. b) Schematic of gas flow and vacuum system attached to furnace 1.

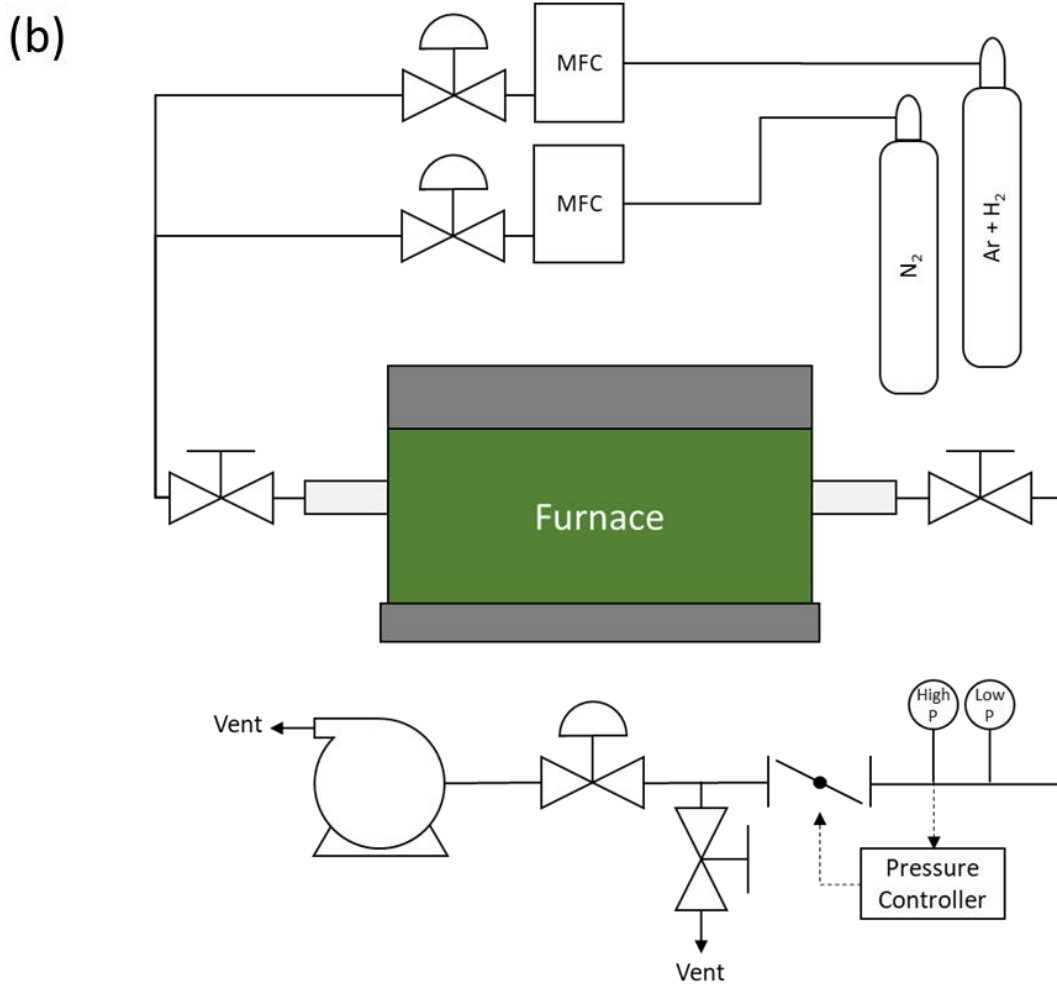
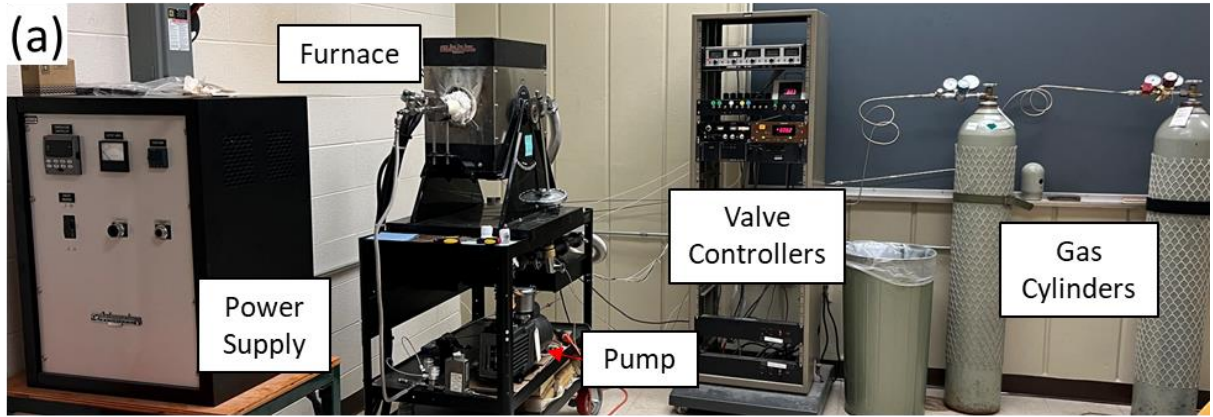


Figure 17 - a) Photograph of furnace 2 with components labeled. b) Schematic of gas flow and vacuum system attached to furnace 2.

1.5 References

- [1] J. Greim and K. A. Schwetz, "Boron carbide, boron nitride, and metal borides," *Ullmann's Encyclopedia of Industrial Chemistry*. Wiley-VCH Verlag GmbH & Co. KGaA, Weinheim, Germany, 15-Dec-2006.
- [2] K. Watanabe, T. Taniguchi, and H. Kanda, "Direct-bandgap properties and evidence for ultraviolet lasing of hexagonal boron nitride single crystal," *Nat. Mater.*, vol. 3, no. 6, pp. 404–409, Jun. 2004.
- [3] G. Cassabois, P. Valvin, and B. Gil, "Hexagonal boron nitride is an indirect bandgap semiconductor," *Nat. Photonics*, vol. 10, no. 4, pp. 262–266, Apr. 2016.
- [4] B. Gil *et al.*, "Polytypes of sp²-bonded boron nitride," *Crystals (Basel)*, vol. 12, no. 6, p. 782, May 2022.
- [5] A. Klett, "Neutron Detection," in *Handbook of Particle Detection and Imaging*, C. Grupen and I. Buvat, Eds. Cham, Switzerland: Springer International Publishing, 2012, pp. 759–790.
- [6] R. T. Kouzes *et al.*, "Neutron detection alternatives to ³He for national security applications," *Nucl. Instrum. Methods Phys. Res. A*, vol. 623, no. 3, pp. 1035–1045, Nov. 2010.
- [7] D. S. McGregor, T. C. Unruh, and W. J. McNeil, "Thermal neutron detection with pyrolytic boron nitride," *Nucl. Instrum. Methods Phys. Res. A*, vol. 591, no. 3, pp. 530–533, Jul. 2008.
- [8] J. Uher, S. Pospisil, V. Linhart, and M. Schieber, "Efficiency of composite boron nitride neutron detectors in comparison with helium-3 detectors," *Appl. Phys. Lett.*, vol. 90, no. 12, p. 124101, Mar. 2007.
- [9] T. C. Doan, S. Majety, S. Grenadier, J. Li, J. Y. Lin, and H. X. Jiang, "Fabrication and characterization of solid-state thermal neutron detectors based on hexagonal boron nitride epilayers," *Nuclear Instruments and Methods in Physics Research A*, vol. 748, pp. 84–90, 2014.
- [10] X. Zhang *et al.*, "Defect-controlled nucleation and orientation of WSe₂ on hBN: A route to single-crystal epitaxial monolayers," *ACS Nano*, vol. 13, no. 3, pp. 3341–3352, Mar. 2019.
- [11] Y. Ge *et al.*, "Edge magnetism of triangular graphene nanoflakes embedded in hexagonal boron nitride," *Carbon N. Y.*, vol. 203, pp. 59–67, Jan. 2023.
- [12] L. Wang *et al.*, "One-Dimensional Electrical Contact to a Two-Dimensional Material," *Science*, vol. 342, pp. 614–617, 2013.
- [13] A. Woessner *et al.*, "Highly confined low-loss plasmons in graphene-boron nitride heterostructures," *Nat. Mater.*, vol. 14, no. 4, pp. 421–425, Apr. 2015.
- [14] G.-H. Lee *et al.*, "Flexible and transparent MoS₂ field-effect transistors on hexagonal boron nitride-graphene heterostructures," *ACS Nano*, vol. 7, no. 9, pp. 7931–7936, Sep. 2013.
- [15] S. Roux *et al.*, "Radiative lifetime of free excitons in hexagonal boron nitride," *Phys. Rev. B.*, vol. 104, no. 16, Oct. 2021.
- [16] K. Watanabe, T. Taniguchi, T. Niiyama, K. Miya, and M. Taniguchi, "Far-ultraviolet plane-emission handheld device based on hexagonal boron nitride," *Nat. Photonics*, vol. 3, pp. 591–594, 2009.
- [17] D. V. Grudinin *et al.*, "Hexagonal boron nitride nanophotonics: a record-breaking material for the ultraviolet and visible spectral ranges," *Mater. Horiz.*, vol. 10, no. 7, pp. 2427–2435, Jul. 2023.

- [18] J. D. Caldwell *et al.*, “Sub-diffractive, volume-confined polaritons in a natural hyperbolic material: hexagonal boron nitride (Presentation Recording),” in *Metamaterials, Metadevices, and Metasystems 2015*, San Diego, California, United States, 2015.
- [19] S. Dai *et al.*, “Tunable phonon polaritons in atomically thin van der Waals crystals of boron nitride,” *Science*, vol. 343, no. 6175, pp. 1125–1129, Mar. 2014.
- [20] G. Grosso *et al.*, “Tunable and high-purity room temperature single-photon emission from atomic defects in hexagonal boron nitride,” *Nat. Commun.*, vol. 8, no. 705, 2017.
- [21] C. Su *et al.*, “Tuning colour centres at a twisted hexagonal boron nitride interface,” *Nat. Mater.*, vol. 21, no. 8, pp. 896–902, Aug. 2022.
- [22] K. Yasuda, X. Wang, K. Watanabe, T. Taniguchi, and P. Jarillo-Herrero, “Stacking-engineered ferroelectricity in bilayer boron nitride,” *Science*, vol. 372, no. 6549, pp. 1458–1462, May 2021.
- [23] C. R. Woods *et al.*, “Charge-polarized interfacial superlattices in marginally twisted hexagonal boron nitride,” *Nat. Commun.*, vol. 12, no. 1, p. 347, Jan. 2021.
- [24] Y. Wang *et al.*, “High temperature thermal management with boron nitride nanosheets,” *Nanoscale*, vol. 10, pp. 167–173, 2018.
- [25] C. Yuan *et al.*, “Modulating the thermal conductivity in hexagonal boron nitride via controlled boron isotope concentration,” *Communications Physics*, vol. 2, no. 43, 2019.
- [26] V. L. Solozhenko and V. Z. Turkevich, “Phase Diagram of the B–BN System at Pressures up to 24 GPa: Experimental Study and Thermodynamic Analysis,” *J. Phys. Chem. C*, vol. 122, no. 15, pp. 8505–8509, Apr. 2018.
- [27] H. S. Okamoto, M. E. Mueller, and E. M., *ASM Handbook, Volume 03 - Alloy Phase Diagrams (2016 edition)*. Materials Park, OH: ASM International, 2016.
- [28] J. Siwka, “Equilibrium Constants and Nitrogen Activity in Liquid Metals and Iron Alloys,” *ISIJ Int.*, vol. 48, no. 4, pp. 385–394, 2008.
- [29] R. F. Abdulrahman and A. Hendry, “Solubility of nitrogen in liquid nickel-based alloys,” *Metall. Mater. Trans. B*, 2001.
- [30] D. B. Evans and R. D. Pehlke, “The Boron-Nitrogen Equilibrium in Liquid Iron,” in *Transactions of the Metallurgical Society of AIME*, vol. 230, 1964, pp. 1657–1662,.
- [31] T. Ishii and T. Sato, “Growth of single crystals of hexagonal boron nitride,” *J. Cryst. Growth*, vol. 61, no. 3, pp. 689–690, Apr. 1983.
- [32] N. F. Ostrovskaya, T. S. Bartnitskaya, V. I. Lyahenko, V. B. Zelyavskii, and A. V. Kurdyumov, “Crystallization of Boron Nitride from Solution in a Lithium Borate Melt,” *Powder Metal. Metal Ceram.*, vol. 35, no. 11–12, pp. 636–639, 1996.
- [33] T. Yamada, Y. Kamiya, N. Naruse, N. Zettsu, and K. Teshima, “Exclusive Growth of Low-Aspect Ratio, Polyhedral h-BN Crystals in Molten Li₂CO₃ as the Reactive Flux,” *Cryst. Growth Des.*, vol. 19, pp. 5720–5728, 2019.
- [34] R. Lacmann, A. Herden, and C. Mayer, “Kinetics of nucleation and crystal growth,” *Chem. Eng. Technol.*, vol. 22, no. 4, pp. 279–289, Apr. 1999.
- [35] K. Watanabe, T. Taniguchi, and H. Kanda, “Ultraviolet luminescence spectra of boron nitride single crystals grown under high pressure and high temperature,” *Physica Status Solidi A Appl. Res.*, vol. 201, no. 11, pp. 2561–2565, Sep. 2004.
- [36] T. Taniguchi and K. Watanabe, “Synthesis of High-Purity Boron Nitride Single Crystals Under High Pressure by Using Ba-BN Solvent,” *J. Cryst. Growth*, vol. 303, pp. 525–529, 2007.

- [37] Y. Kubota, K. Watanabe, and T. Taniguchi, "Synthesis of cubic and hexagonal boron nitrides by using Ni solvent under high pressure," *Jpn. J. Appl. Phys. (2008)*, vol. 46, no. 1, pp. 311–314, Jan. 2007.
- [38] N. D. Zhigadlo, "Crystal growth of hexagonal boron nitride (hBN) from Mg–B–N solvent system under high pressure," *J. Cryst. Growth*, vol. 402, pp. 308–311, Sep. 2014.
- [39] M. Onodera *et al.*, "Carbon-Rich Domain in Hexagonal Boron Nitride: Carrier Mobility Degradation and Anomalous Bending of the Landau Fan Diagram in Adjacent Graphene," *Nano Lett.*, vol. 19, pp. 7782–7286, 2019.
- [40] B. N. Feigelson, R. M. Frazier, and M. Twigg, "III-Nitride crystal growth from nitride-salt solution," *J. Cryst. Growth*, vol. 305, no. 2, pp. 399–402, Jul. 2007.
- [41] Y. Gu, M. Zheng, Y. Liu, and Z. Xu, "Low-temperature synthesis and growth of hexagonal boron-nitride in a lithium bromide melt," *J. Am. Ceram. Soc.*, vol. 90, no. 5, pp. 1589–1591, May 2007.
- [42] Y. Kubota, K. Watanabe, O. Tsuda, and T. Taniguchi, "Deep Ultraviolet Light-Emitting Hexagonal Boron Nitride Synthesized at Atmospheric Pressure," *Science*, vol. 317, pp. 932–934, 2007.
- [43] Y. Kubota, K. Watanabe, O. Tsuda, and T. Taniguchi, "Hexagonal boron nitride single crystal growth at atmospheric pressure using Ni–Cr solvent," *Chem. Mater.*, vol. 20, no. 5, pp. 1661–1663, Mar. 2008.
- [44] B. Clubine, "Synthesis and characterization of bulk single crystal hexagonal boron nitride from metal solvents," MSc, Kansas State University, Manhattan, KS, 2010.
- [45] T. B. Hoffman, B. Clubine, Y. Zhang, K. Snow, and J. H. Edgar, "Optimization of Ni–Cr flux growth for hexagonal boron nitride single crystals," *J. Cryst. Growth*, vol. 393, pp. 114–118, May 2014.
- [46] J. Sperber, "Investigations of Hexagonal Boron Nitride: Bulk Crystals and Atomically-Thin Two Dimensional Layers," PhD, Kansas State University, Manhattan. KS, 2016.
- [47] S. Liu *et al.*, "Large-scale growth of high-quality hexagonal boron nitride crystals at atmospheric pressure from an Fe–Cr flux," *Cryst. Growth Des.*, vol. 17, no. 9, pp. 4932–4935, Sep. 2017.
- [48] S.-Y. Zhang, K. Xu, X.-K. Zhao, Z.-Y. Shao, and N. Wan, "Improved hBN single-crystal growth by adding carbon in the metal flux," *Cryst. Growth Des.*, vol. 19, no. 11, pp. 6252–6257, Nov. 2019.
- [49] J. Cao, M. Tian, S. Zhang, W. Hu, N. Wan, and T. Lin, "Carbon-related defect control of bulk hBN single crystals growth by atmospheric-pressure metal-flux-based fusion synthesis," *J. Mater. Sci.*, vol. 57, no. 31, pp. 14668–14680, Aug. 2022.
- [50] J. Li *et al.*, "Hexagonal Boron Nitride Single Crystal Growth from Solution with a Temperature Gradient," *Chem. Mater.*, vol. 32, pp. 5066–5072, 2020.
- [51] J. Li *et al.*, "Hexagonal Boron Nitride Crystal Growth from Iron, a Single Component Flux," *ACS Nano*, vol. 15, no. 4, pp. 7032–7039, Apr. 2021.
- [52] M. Onodera *et al.*, "Hexagonal boron nitride synthesized at atmospheric pressure using metal alloy solvents: Evaluation as a substrate for 2D materials," *Nano Lett.*, vol. 20, no. 1, pp. 735–740, Jan. 2020.
- [53] N. Zhang, N. Yang, W. Wang, X. Zhong, and X. Chen, "Growth of hexagonal boron nitride crystals at atmospheric pressure from Cu Cr flux," *J. Cryst. Growth*, vol. 562, no. 126074, p. 126074, May 2021.

- [54] Y. Li *et al.*, “Synthesis of centimeter-scale high-quality polycrystalline hexagonal boron nitride films from Fe fluxes,” *Nanoscale*, vol. 13, no. 25, pp. 11223–11231, Jul. 2021.
- [55] T. B. Hoffman, Y. Zhang, J. H. Edgar, and D. K. Gaskill, “Growth of hBN using metallic boron: Isotopically enriched h10BN and h11BN,” *Mater. Res. Soc. Symp. Proc.*, vol. 1635, no. mrsf13-1635-t06-10, pp. 35–40, 2014.
- [56] T. Hoffman, “Optimization and Characterization of Bulk Hexagonal Boron Nitride Single Crystals Grown by the Nickel-Chromium Flux Method,” PhD, Kansas State University, Manhattan, KS, 2016.
- [57] S. Liu, R. He, L. Xue, J. Li, B. Liu, and J. H. Edgar, “Single Crystal Growth of Millimeter-Sized Monoisotopic Hexagonal Boron Nitride,” *Chem. Mater.*, vol. 30, pp. 6222–6225, 2018.
- [58] J. Li *et al.*, “Single crystal growth of monoisotopic hexagonal boron nitride from a Fe–Cr flux,” *J. Mater. Chem. C Mater. Opt. Electron. Devices*, vol. 8, no. 29, pp. 9931–9935, 2020.

Chapter 2 - Optimizing Boron Concentration

In many other studies on the solution growth of hBN crystals, the boron source material was hot pressed boron nitride (HPBN) [1]–[10]. In those cases, boron is present in large excess such that the concentration of boron in solution is dictated by the kinetics of the solvent dissolving the HPBN, the hBN growth rate, and the solubility limit of boron in the solvent. In this work, the boron source material was elemental boron powder, which gives more precise control over the boron concentration in the solution and enables synthesis of isotopically enriched hBN simply by using isotopically pure boron powder (see Chapter 5). However, this necessitates choosing an amount of boron to add to the solvent at the start of each experiment and presents another variable to optimize.

The concentration of boron dramatically affects the phase equilibria in hBN crystal growth solutions as will be shown in this chapter. Figure 18a shows a hypothetical liquidus curve for hBN in a molten metal solution. Above the curve, hBN is not stable: only a homogenous liquid phase is present. Below the curve, hBN is also stable and will precipitate from the liquid. An optimal starting boron concentration would be equal to the liquidus curve at the starting temperature.

If the concentration is much higher than the optimum, the solution will start in a state far from equilibrium, creating a large driving force for hBN to precipitate and thus causing many hBN crystals to nucleate as illustrated by the orange dashed line in Figure 18. These crystals will grow as quickly as the mass transport and reaction kinetics will allow. This rapid growth tends to create more defective crystals as the atoms do not have time to find their most stable positions, and the abundance of nuclei will result in many small crystals instead of a few large ones as the crystals grow until they collide with their many close neighbors.

With the optimal starting boron concentration, illustrated by the green dashed line in Figure 18, the driving force for precipitating hBN will be controlled by the cooling rate of the furnace. Therefore, throughout the slow cooling process, the system will stay close to equilibrium, keeping the driving force for hBN precipitation small. Therefore, compared to the case with a too high boron concentration, fewer hBN crystals nucleate and grow more slowly, allowing them to grow larger and with better quality.

If a boron concentration much lower than the optimum is used, time and energy will be wasted as illustrated by the blue dashed line in Figure 18. Until the temperature drops to the liquidus curve, hBN will not precipitate at all. Once the temperature reaches the liquidus curve, hBN will nucleate and grow like with the optimum concentration, just at a lower temperature. However, higher temperatures are expected to produce higher quality crystals since atomic mobility increases with increasing temperature, allowing atoms to find their most stable locations more easily. Therefore, lowering the starting temperature to accommodate the lower starting boron concentration is not a good solution.

This chapter discusses how to find the optimum boron concentration, both experimentally and with the use of CALPHAD, with specific focus on maximizing the size of the single crystals formed.

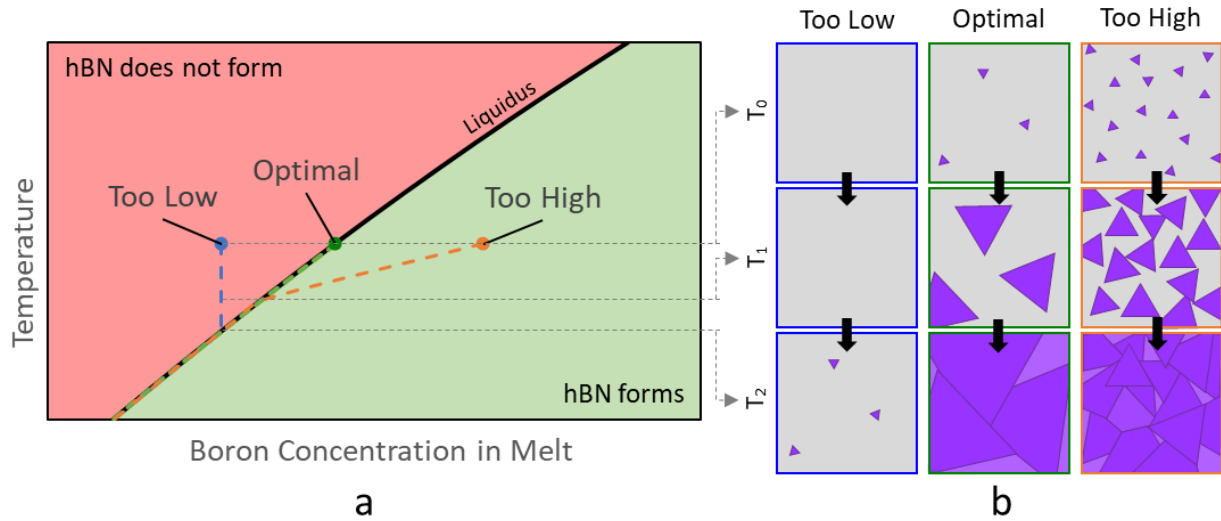


Figure 18 – Hypothetical liquidus curve of $L \rightarrow hBN$ illustrating how to optimize the boron concentration. A concentration that is too high will have a high nucleation rate due to being overly supersaturated, resulting in many small crystals. A concentration that is too low will waste time and energy because no hBN will precipitate until the system hits the liquidus. An optimal concentration occurs where the liquidus intersects the starting temperature so that the system starts saturated, then slowly supersaturates to limit nucleation and produce few large crystals instead of many small ones.

2.1 CALPHAD Modeling

The CALPHAD (CALculation of PHase Diagrams) method, described in great detail in ref. [11], is an algorithm that uses thermodynamic data collected from experiments and ab initio calculations with one, two, or three components to predict phase diagrams and thermodynamic properties in multicomponent systems. The thermodynamic data is used to determine a set of Gibbs energy equations that represent how every component in a system interacts with every other component in every phase that could be stable. For example, to accurately predict the liquid phase in the Fe-B-N system, equations for each unary (Fe, B, and N), binary (Fe-B, Fe-N, and B-N), and ternary (Fe-B-N) in the liquid phase need to be known. Ternary components can often be excluded from the equations if the ternary interactions are weak or one or more of the components is very dilute, making ternary interactions unlikely. Each of these equations are

combined into Gibbs energy equations for each phase (G_i) that are a function of temperature, pressure, and the concentration of every component in the system.

$$G_i = f(T, P, x_1, x_2, \dots) \quad \text{Equation 1}$$

To determine what phase(s) are stable, the Gibbs energies for every phase are summed together, weighted by the amount of each phase (n_i) and the total Gibbs energy (G_{Total}) is minimized by adjusting the amount of each phase and the free parameters.

$$G_{Total} = \sum n_i G_i \quad \text{Equation 2}$$

For example, in the Fe-B-N system, the temperature, pressure, and overall concentrations of Fe, B, and N in the system could be fixed and the amount of each phase and the concentration of components in each phase will be adjusted to minimize the total Gibbs energy. This can be repeated at other temperatures and other overall concentrations to fill out an entire phase diagram. However, calculating a phase diagram is only part of what the CALPHAD method can predict. Since the process provides a value for the total Gibbs energy at every state, many different thermodynamic properties such as the heat capacity or the coefficient of thermal expansion at those states can be calculated from Maxwell Relations.

This is a powerful method to accurately extrapolate to states with no experimental data or to systems with four or more components without needing to gather additional data on those systems. In this work, the CALPHAD method was applied to two systems: Fe-B-N and Ni-Cr-B-N. Some data is available on the ternary Fe-B-N system [12]–[14], but the CALPHAD method can extrapolate and interpolate to the entire temperature and concentration range of interest in this study. For the Ni-Cr-B-N system, no data is available on the quaternary system and only scattered data is available for the four ternary sub-systems [15]–[17], but the CALPHAD method is able to accurately fill those gaps as well.

In this work, ThermoCalc [18] software handled the intricacies of the CALPHAD method using their TCFE9 Steels/Fe-alloys database as the basis for all calculations. In all calculations, the pressure was fixed at 1 bar, which is close to the pressure used during experiments (1.14 bar). The total mass of boron and metal (Fe or Ni + Cr) in the system was set for each calculation (summarized in Table 1) to match the mass of these components in experiments. The amount of nitrogen in the system was defined by fixing the number of moles of N₂ in the gas at a constant value, regardless of how the temperature changes or how much nitrogen dissolves into the solution or reacts with the boron to form hBN. This simulates a continuous flow of nitrogen into the system throughout an experiment, which creates a virtually infinite source of nitrogen. Thus, at every state calculated, nitrogen is fully saturating the system. The evaporation of boron, solvent metals, and hBN was ignored for these calculations, so the gas phase is pure N₂. This makes the definition of the moles of N₂ in the gas phase arbitrary since any amount greater than zero will saturate the solution within the given parameters. Finally, the temperature was varied as the independent variable so that the phase behavior throughout the experimental temperature range could be studied.

Table 1 – Masses of components used in CALPHAD simulations.

Mass% B	Mass B (g)	Mass Fe (g)	Mass Ni (g)	Mass Cr (g)
2	0.204	10	---	---
3.0	0.31	10	---	---
4.0	0.42	10	---	---
5.0	0.53	10	---	---
3.0	6.2	---	100	100
4.0	8.3	---	100	100
5.0	10.5	---	100	100
6.0	12.8	---	100	100

An example of the output of these calculations is shown in Figure 19, which shows the mass fraction of every phase plotted versus the temperature of the system using either Fe (Figure

19a) or 1:1 Ni-Cr (Figure 19b) as a solvent and containing 3 mass% B. At high temperatures, both systems consist of only two phases: liquid and gas. The first solid phase to become stable upon cooling is hBN, which occurs at 1592°C using Fe and 1474°C using Ni-Cr with 3 mass% B. This temperature marks the position of the liquidus under the given conditions and represents the state at which hBN will start precipitating. The mass fraction of hBN provides a way to predict the yield in crystal growth experiments as discussed in Section 2.3. At lower temperatures, the solvent starts to solidify as indicated by the sudden shift of liquid to body centered cubic (BCC) at 1443°C using Fe and to hexagonal close pack (HCP) at 1365°C using Ni-Cr. These temperatures provide a lower bound on the temperature range in which high-quality hBN can be grown. Coprecipitation of two solid phases typically reduces the crystal size of both as one solid provides more nucleation sites for the other solid to form and vice versa. Furthermore, once the solution has fully solidified, the mass transport kinetics required to feed hBN crystals more boron and nitrogen become too slow for practical solution growth of bulk crystals. Each of these lines shifts based on the concentration of boron in the system, allowing the effect of boron on the phase equilibrium of the system to be extracted.

A liquidus curve can be extracted by plotting the liquidus temperature at a series of boron concentrations as shown in Figure 19c. As discussed at the start of this chapter, the optimum boron concentration will be the concentration of the liquidus curve at 1550°C, the maximum temperature in the standard crystal growth process used in this work. This concentration is 2.3 mass% B for Fe and 4.0 mass% B for Ni-Cr. In past work [19], the boron concentration that produced the best results in a Ni-Cr solvent was 4 mass% B, perfectly matching the predicted optimum. Similar work with a pure Fe solvent had not been completed prior to this work, so a series of experiments were conducted to test the effect of boron as discussed in the next section.

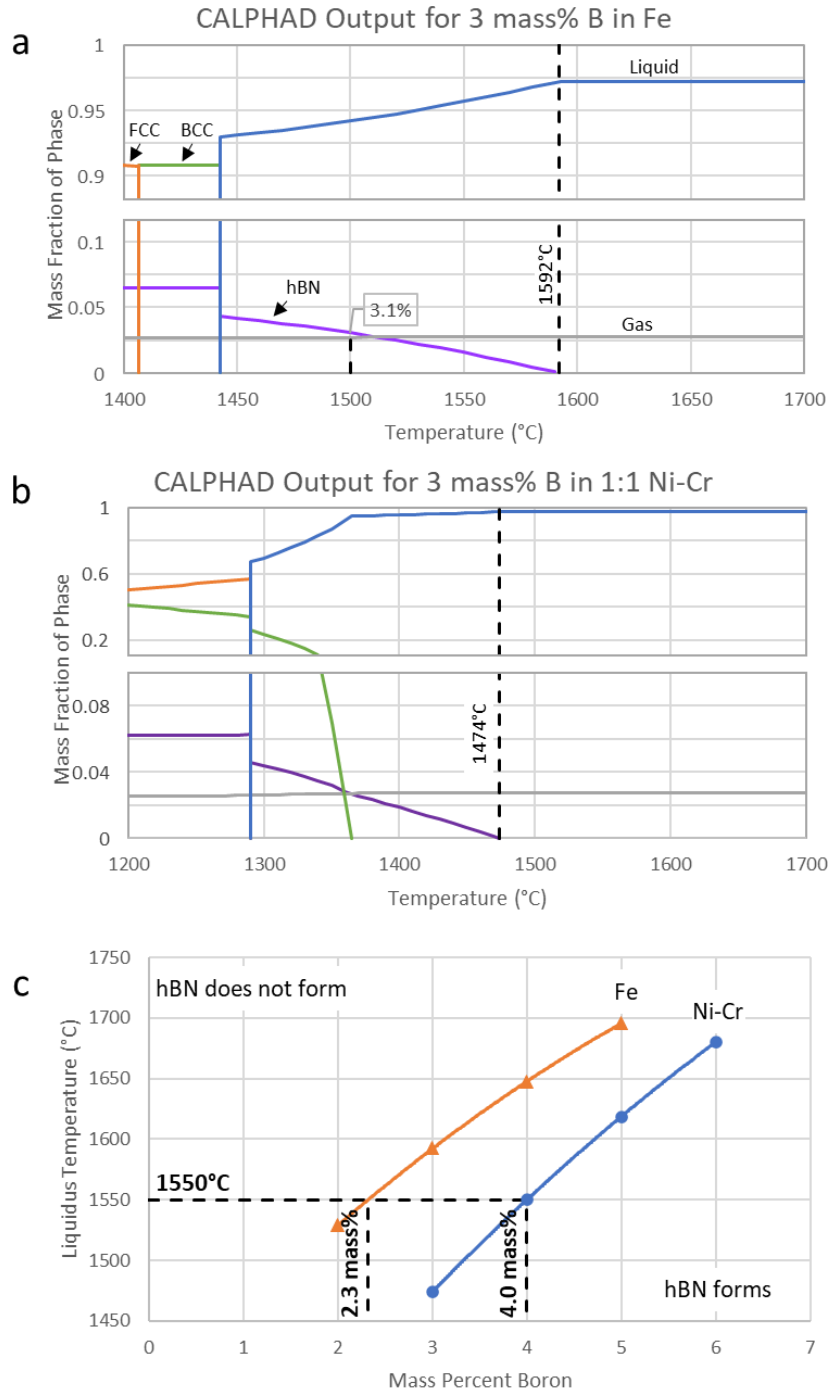


Figure 19 – Results of CALPHAD Modeling on Fe-B-N and Ni-Cr-B-N systems. Mass fraction of each phase is plotted versus temperature for the Fe-B-N system (a) and the Ni-Cr-B-N system (b) containing 3 mass% B. The temperature at which hBN first becomes stable upon cooling and the amount of hBN predicted to precipitate by the quench temperature are noted. C) The liquidus curves for both systems are derived by plotting the former versus the boron concentration used to calculate the phase equilibria.

2.2 Experimental Validation

To determine the validity of the predictions presented in the previous section, a series of hBN crystal growth experiments were conducted with a range of boron concentrations in an Fe solvent, using the average size of hBN single crystals as the metric of success. If the maximum crystal size is obtained at or near the predicted optimum boron concentration, the predictions will be considered accurate, suggesting that the predictive power of CALPHAD will be useful for optimizing other systems as well. If the maximum crystal size does not match the predicted optimum or is not affected by the boron concentration at all, determining why will help better understand how hBN solution growth works.

Boron and Fe powder in amounts summarized in Table 2 were loaded in alumina boats and run through the standard crystal growth process described in Section 1.4. Optical micrographs were taken of the crystals that formed, both as-grown on the solidified metal ingot and as free-standing hBN flakes obtained by mechanical exfoliation with thermal release tape. Micrographs that were representative of the crystals produced in each experiment were selected and used to identify the range of crystal sizes produced as shown in Figure 20. Single crystals were identified by manually coloring over the single crystals in a digital painting program as shown in Figure 20b. Where no hBN was present or details of crystals were difficult to discern due to the image being out of focus or too dark, the image was left blank, excluding these regions from consideration in further analysis. This was done manually because automatic tools proved unreliable for identifying grain boundaries due to the abundance of visible features present within grain boundaries, resulting in the software consistently underestimating the size of crystals.

Table 2 – Composition of solution at the start of each boron optimization experiment with an Fe solvent

Experiment #	Mass B (g)	Mass Fe (g)	Mass% B
130	1.16	48.84	2.3
131	1.16	48.84	2.3
132	1.50	48.50	3.0
133	1.5056	48.50	3.0
134	1	49.00	2.0
135	1	49.00	2.0
136	1.5	48.50	3.0
138	1.16	48.84	2.3
141	1.1598	48.84	2.3
146	0.9993	24.01	4.0
147	1.25	23.75	5.0
149	1.0065	24.02	4.0
150	1.2503	23.75	5.0
152	0.6254	24.38	2.5
153	0.8751	24.13	3.5
154	0.625	24.38	2.5
155	0.8753	24.13	3.5
160	1.1627	48.84	2.3
161	1.25	48.77	2.5
171	1.1598	48.84	2.3

These images were then analyzed with ImageJ’s Analyze Particles function to measure the area of each colored region, which corresponds to the size of each crystal. The crystals were sorted into bins by their areas, then the sum of all areas in each bin was normalized by the total area of all crystals in the image. This gives an estimate of the percentage of the total surface area covered in crystals of a particular range of sizes. An example of a histogram of the percent coverage for each bin is shown in Figure 20c. The process used to generate this data is imperfect, with potential for errors in correctly identifying grain boundaries or bias in choosing representative areas from each experiment, but it is still expected to be accurate to within $\pm 20\%$. Similar figures as those shown in Figure 20 are provided for the other experiments in this series in Appendix A.

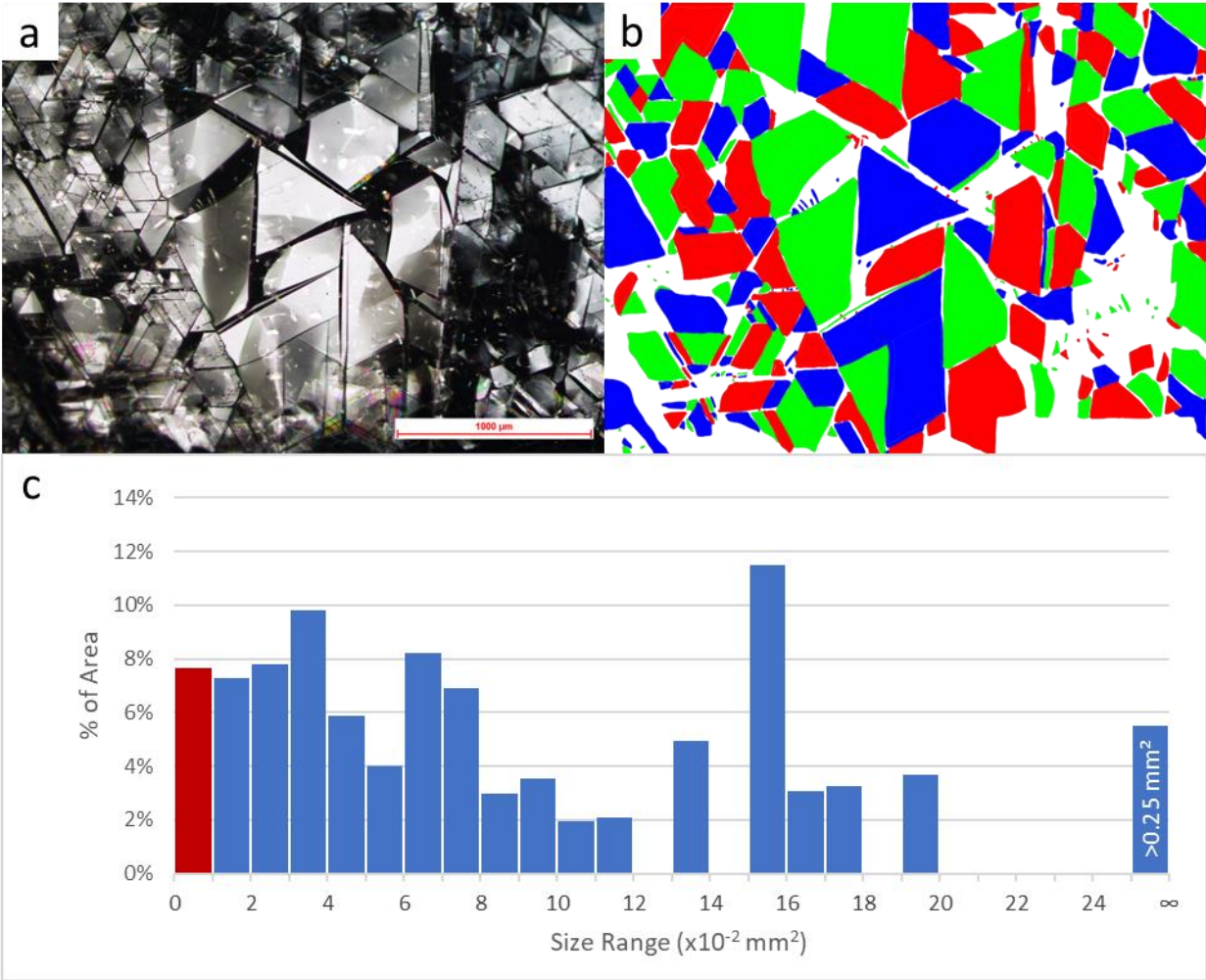


Figure 20 – Example of process used to extract crystal sizes from optical micrographs. a) Optical micrograph of hBN grown from an Fe solvent. b) Crystals highlighted by coloring over single crystals in the micrograph using a digital painting program. Blank areas are regions where the image was too dark or out of focus to properly identify crystals, so were excluded from analysis. c) Histogram showing how much of the image was filled by crystals of different size ranges. hBN single crystals $<0.01 \text{ mm}^2$ (red bar) are too small for device applications.

Crystals as small as 0.01 mm^2 can frequently be used for devices, so the percentage of the solvent-gas interface covered with crystals larger than 0.01 mm^2 (termed “coverage” here) provides a succinct measure of how successful a given experiment was. Figure 21 shows coverage plotted versus boron concentration with micrographs showing examples of crystals grown with each of the boron concentrations tested. The trend here is clear: boron concentrations significantly above the predicted optimum ($>3.0 \text{ mass\% B in Fe}$) produced hBN with a

significantly smaller crystal size than boron concentrations near the predicted optimum (2.0-3.0 mass% B in Fe). This indicates that optimizing the boron concentration is crucial for maximizing crystal size and that the CALPHAD method is a viable method for optimizing it. Boron concentrations lower than 2.0 mass% were not tested, but the crystal size would likely drop again at low enough concentrations due to not having enough time to grow before the system is quenched.

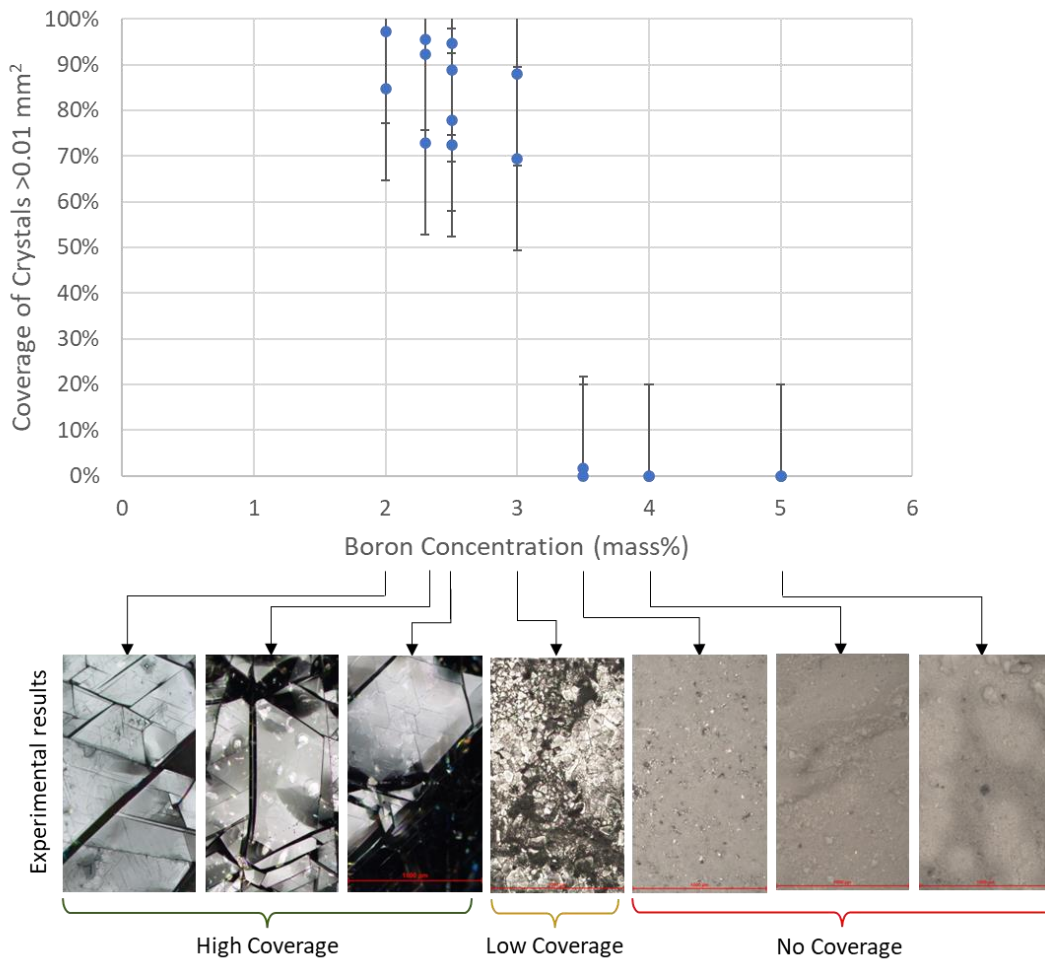


Figure 21 – Coverage of Fe-grown hBN single crystals larger than 0.01 mm² in area versus the boron concentration added to the solution at the start of the experiment. Error bars show range of coverage measured in experiments with the same boron concentration. Optical micrographs of representative areas of the ingot surface for each concentration shown at bottom. Width of each image is 1 mm.

A possible explanation for why hBN crystals grown with 2.0 mass% B are not measurably smaller than hBN crystals grown with 2.3 mass% B is that crystal growth only occurs within a fraction of the total slow cooling period. If this is true, concentrations that are slightly too low would simply shift the crystal growth range to lower temperatures and the process would continue in much the same way as with the optimal concentration. This is still undesirable though because crystals grown at lower temperatures are expected to have worse crystal quality. At sufficiently low boron concentrations, the crystal growth range would overlap with the quench stage, at which point the crystal size would drop precipitously. Additional evidence for hBN only growing within a fraction of the slow cooling range is discussed in the next section.

2.3 Expected vs. Observed Yield

A significant deviation between the CALPHAD predictions and experimental observations is in the yield of boron to boron nitride: only about 0.75% of the boron added to the solution precipitates as hBN while CALPHAD predicts the yield of B to hBN to be 31%. The former was determined by stripping hBN from the surface of the solidified ingot with thermal release tape and weighing the free-standing crystals. This is an imperfect method for determining the total amount of hBN precipitated because some crystals remain adhered to the ingot despite multiple attempts to mechanically exfoliate them. However, in experiments using Fe as a solvent, 80-90% of the surface area covered with hBN can frequently be stripped entirely of hBN, allowing this method to still provide a rough approximation of yield. These measurements are all underestimates of yield, but not by enough to explain the ~40x difference between the measured and predicted yield.

The predicted yield was determined from the mass fraction of the hBN phase predicted with CALPHAD at 1500°C, the temperature at which the system is quenched. An example of this is shown in Figure 19a, where the mass fraction of hBN in the system is predicted to be 3.1 mass%. This is multiplied by the total mass of the system to get the mass of hBN, which is converted to the mass of B contained in hBN, then divided by the total mass of boron in the system to predict the yield (47%). With the optimal boron concentration (2.3 mass%), the predicted mass fraction of hBN at 1500°C is 1.3 mass%, corresponding to a yield of B to hBN of 31%. More hBN could precipitate during quenching, making this prediction an underestimate, but accounting for kinetic changes during quenching would be difficult and this still provides a lower bound for the predicted yield.

The large discrepancy between the measured and predicted yield suggests that more of the boron present in the solution could still be converted into hBN. To test that, the hBN precipitated from an Fe solution was mechanically exfoliated from the ingot, then the ingot was run through the standard crystal growth process again (skipping ingot formation) without adding any more source materials. The result was the precipitation of more hBN single crystals with a similar size and clarity as those formed in the first experiment (see Figure 22). To test the limits of recycling an ingot, this process was repeated another 3 times, for a total of 5 uses of the same source material. In each experiment, the size and clarity of crystals seemed largely unaffected by reusing the source material. The third run with Fe and the fifth run with Ni-Cr are exceptions where the crystal size was notably smaller, but this is likely simply due to process-to-process variability rather than being a result of reusing the material.

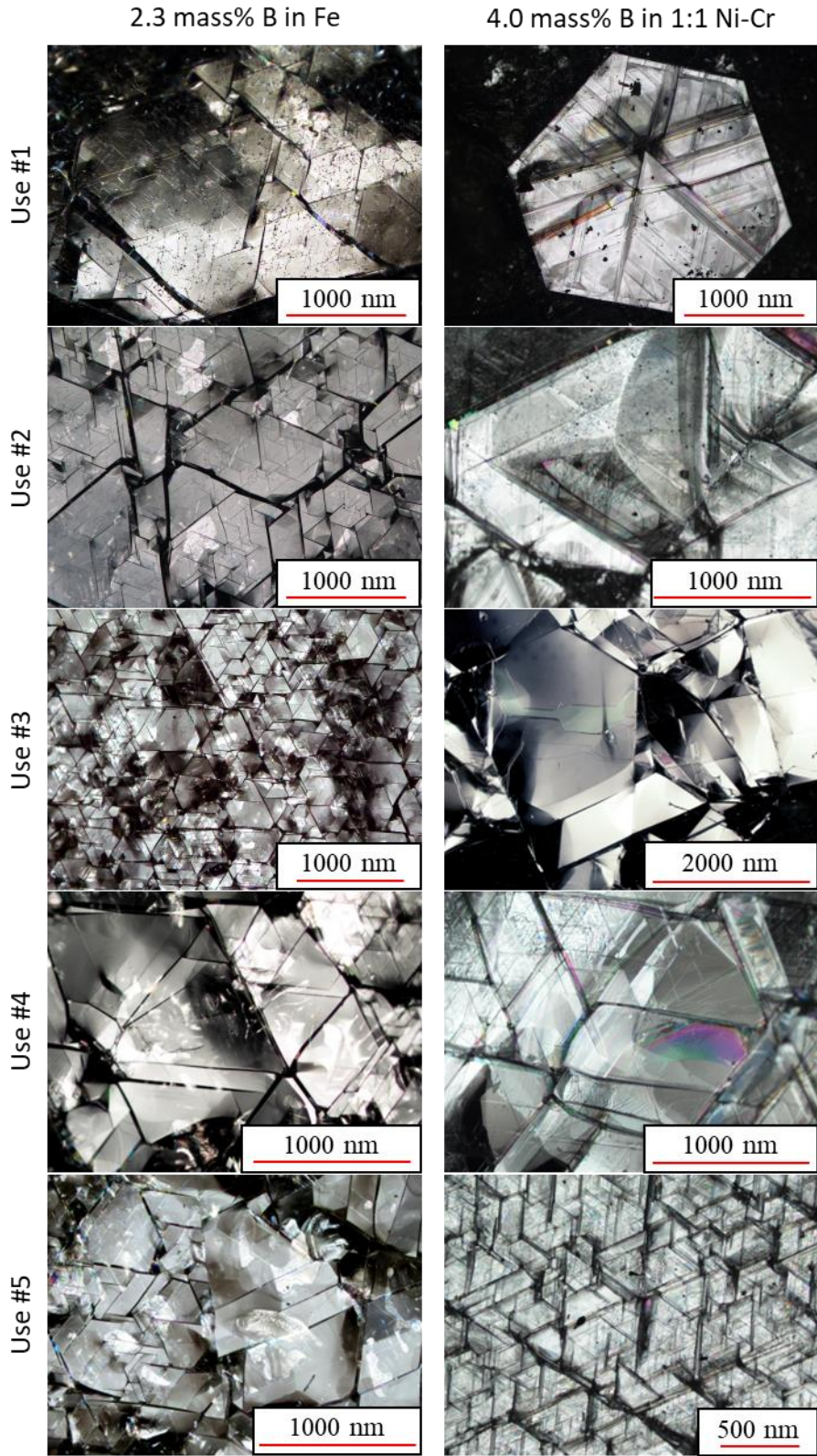


Figure 22 – Optical micrographs of hBN grown from Fe (left) and Ni-Cr (right) across 5 uses of the same source material.

This discovery is a great boon to improving the resource efficiency of the atmospheric pressure solution growth process, which is especially beneficial when producing isotopically-enriched hBN (see Chapter 5) where the cost of source materials is much higher. The same source material could likely be reused more than 5 times, but that was not attempted in this work. Assuming that the predicted yield of B to hBN (31%) accurately represents how much hBN could be produced with the given source material and only 0.75% of the initial boron is converted to hBN in each experiment, it may be possible to reuse the same ingot 40 times.

However, a significant concern with reusing the same source material multiple times is contamination of the source material or concentration of impurities experiment-to-experiment. Since these experiments are not conducted in a clean room, contaminants in the environment such as dust could deposit on the source material and the use of thermal release tape to remove hBN between experiments could leave behind small amounts of adhesive residue. Furthermore, as boron is extracted from the solvent through hBN crystal growth and small amounts of metal evaporates, impurities present in the solution may become more concentrated with each experiment, increasing their chance of incorporating into the hBN single crystals.

To test if the impurity concentration in the hBN crystals changes with repeated use of the source material, hBN samples from the first and 5th uses with both Fe and Ni-Cr (1:1) solvents were tested using Secondary Ion Mass Spectrometry (SIMS) at Eurofins EAG. In all four cases, the carbon and oxygen concentrations were below their detection limits of $<2E16$ atoms/cm³ (<0.4 ppm) for carbon and $<2E17$ atoms/cm³ (<4 ppm) for oxygen. SIMS may not be sensitive enough to detect the effect of repeated uses of the source material on impurity concentrations, but this indicates that any effects it does have are minor.

In any case, the fact that hBN can be grown with successive uses of the same source material indicates that the process is kinetically limited. If the system stayed at or near equilibrium throughout the slow cooling period (Figure 23a), the boron concentration in the solution would slowly decline as it was converted into hBN until the system was quenched. In this case, the boron concentration in the solution at the end of the experiment would equal the concentration of the liquidus at the quench temperature. Since the precipitated hBN is removed in subsequent experiments, this would be the starting boron concentration of the following experiment. No hBN will precipitate until the system hits the liquidus curve and since this wouldn't happen until the quench temperature, no hBN would precipitate at all in the second run. If the system is instead kinetically limited (Figure 23b), dissolved boron will be converted to hBN more slowly than the slope of the liquidus curve allows, reducing the boron concentration less than what is thermodynamically possible. Thus, subsequent runs with the same source materials would hit the liquidus curve before quench, allowing more hBN to precipitate. This is what is observed experimentally, indicating that the process is kinetically limited.

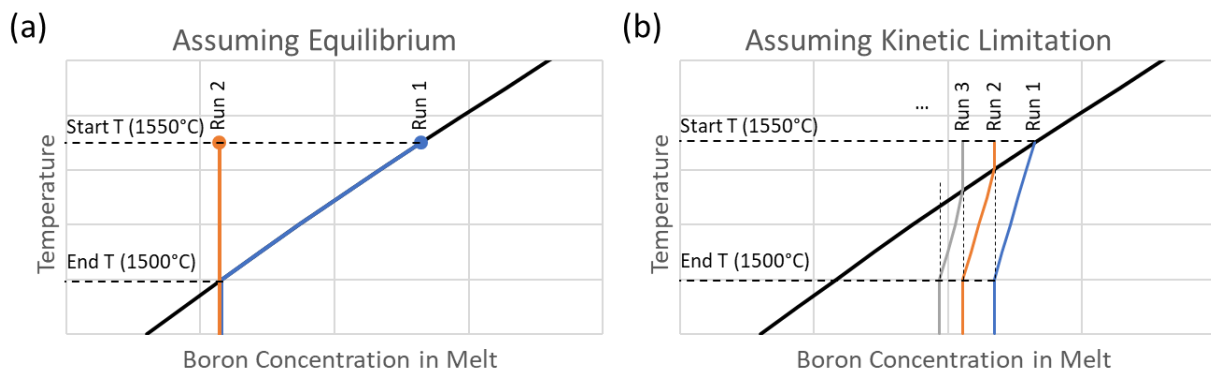


Figure 23 – Hypothetical liquidus curve illustrating how the boron concentration would change with temperature during solution growth of hBN in multiple uses of the same source material. a) Assuming the system is always at equilibrium, no hBN would be able to form in a second run due to the boron being depleted in the first. b) Assuming the system is kinetically limited, hBN could precipitate from the solution in multiple reuses of the source material because less hBN precipitates in each run than is thermodynamically possible.

The kinetic limitation may be due to a reduction in the nitrogen mass transport into the solution caused by the formation of an hBN layer that blocks nitrogen from reaching the surface, as illustrated in Figure 24a. The crystal growth process used in this work starts by heating to 1550°C and dwelling there for 24 hours, giving ample time for nitrogen to saturate the solution without forming hBN. Therefore, when the system begins to slowly cool, it is starting from an equilibrium state. As the system continues to cool, hBN forms at the liquid-gas interface and more nitrogen must dissolve to feed further crystal growth as illustrated Figure 24a (left). Since most of the surface is still bare molten metal, nitrogen gas is uninhibited from dissolving into the solution and the system stays close to equilibrium, which is reflected by the segment of the high temperature segment of the blue line in Figure 24b. However, since nitrogen cannot easily diffuse through a solid, the more hBN that forms on the surface, the slower nitrogen mass transport into the solution becomes, and the slower the formation of hBN becomes. This is reflected by the low temperature segment of the blue line in Figure 24b, where the system's state deviates further and further from the liquidus curve as the system cools. Eventually, the entire gas-liquid interface is filled with a layer of hBN single crystals, which blocks nitrogen mass transport entirely and any further hBN growth would be fed by the reservoir of dissolved boron and nitrogen (Figure 24a, right) until it is depleted and growth halts entirely.

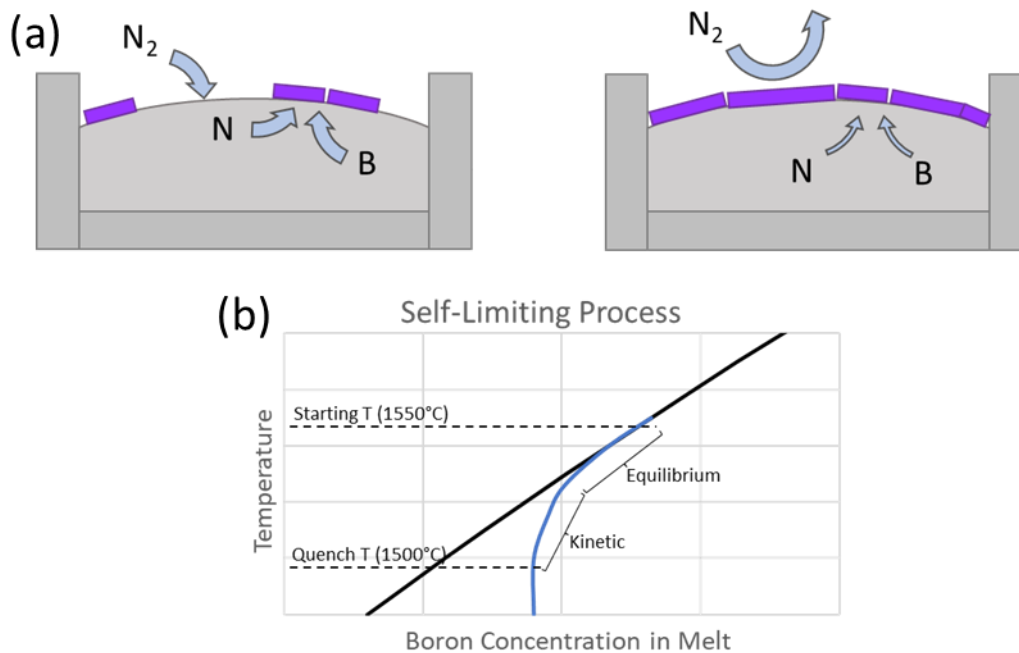


Figure 24 – a) Diagrams of the self-limiting process hypothesized to be present in the process used in this work. Left – At the start of slow cooling, only a few hBN crystals have precipitated, allowing N_2 from the gas to dissolve into the solution uninhibited and maintaining the system near equilibrium. Right – At the end of slow cooling, hBN crystals fully cover the gas-solvent interface, blocking N_2 from dissolving into the solution. Any further growth must be fed by the reservoir of nitrogen and boron dissolved in the solution. b) Liquidus curve (black) compared to hypothetical state of the system (blue) as the system is slowly cooled. The system starts near equilibrium, but steadily deviates further and further from equilibrium as hBN covers more and more of the gas-solvent interface.

It is clear that the crystal growth process used in this work is kinetically limited, which contradicts the assumption in CALPHAD simulations that the system is at equilibrium, but this does not invalidate its use for optimizing the process. This is because the assumption of equilibrium is still accurate at the start of slow cooling, at which point the system has been dwelled at a constant temperature for 24 hours. Thus, the predictions discussed in Section 2.1 will also be accurate at the start of slow cooling. Experiments using boron concentrations >3 mass% produced very small hBN crystals because the system far exceeded saturation and thus the nucleation rate was higher than in lower concentration experiments. Regardless of how the kinetics change later, the number of crystals that nucleate is the biggest factor in determining the

final size of hBN crystals because they usually grow until they collide with neighboring crystals or the walls of the container.

2.4 References

- [1] T. Ishii and T. Sato, "Growth of single crystals of hexagonal boron nitride," *J. Cryst. Growth*, vol. 61, no. 3, pp. 689–690, Apr. 1983.
- [2] Y. Kubota, K. Watanabe, and T. Taniguchi, "Synthesis of cubic and hexagonal boron nitrides by using Ni solvent under high pressure," *Jpn. J. Appl. Phys.* (2008), vol. 46, no. 1, pp. 311–314, Jan. 2007.
- [3] T. Taniguchi and K. Watanabe, "Synthesis of high-purity boron nitride single crystals under high pressure by using Ba–BN solvent," *J. Cryst. Growth*, vol. 303, no. 2, pp. 525–529, May 2007.
- [4] Y. Kubota, K. Watanabe, O. Tsuda, and T. Taniguchi, "Hexagonal boron nitride single crystal growth at atmospheric pressure using Ni–Cr solvent," *Chem. Mater.*, vol. 20, no. 5, pp. 1661–1663, Mar. 2008.
- [5] N. D. Zhigadlo, "Crystal growth of hexagonal boron nitride (hBN) from Mg–B–N solvent system under high pressure," *J. Cryst. Growth*, vol. 402, pp. 308–311, Sep. 2014.
- [6] T. B. Hoffman, B. Clubine, Y. Zhang, K. Snow, and J. H. Edgar, "Optimization of Ni–Cr flux growth for hexagonal boron nitride single crystals," *J. Cryst. Growth*, vol. 393, pp. 114–118, May 2014.
- [7] S. Liu et al., "Large-scale growth of high-quality hexagonal boron nitride crystals at atmospheric pressure from an Fe–Cr flux," *Cryst. Growth Des.*, vol. 17, no. 9, pp. 4932–4935, Sep. 2017.
- [8] S.-Y. Zhang, K. Xu, X.-K. Zhao, Z.-Y. Shao, and N. Wan, "Improved hBN single-crystal growth by adding carbon in the metal flux," *Cryst. Growth Des.*, vol. 19, no. 11, pp. 6252–6257, Nov. 2019.
- [9] J. Li et al., "Hexagonal Boron Nitride Crystal Growth from Iron, a Single Component Flux," *ACS Nano*, vol. 15, no. 4, pp. 7032–7039, Apr. 2021.
- [10] N. Zhang, N. Yang, W. Wang, X. Zhong, and X. Chen, "Growth of hexagonal boron nitride crystals at atmospheric pressure from Cu Cr flux," *J. Cryst. Growth*, vol. 562, no. 126074, p. 126074, May 2021.
- [11] H. Lukas, S. G. Fries, and B. Sundman, *Computational thermodynamics*. Cambridge, England: Cambridge University Press, 2012.
- [12] D. L. Ball, "THE PRECIPITATION OF BORON NITRIDE FROM FERROUS MELTS," *AIME MET SOC TRANS*, vol. 239, no. 1, pp. 31–36, 1967.
- [13] M. S. Yaghmaee and B. Shokri, "Modeling the formation of strong couples in high temperature liquid," *J. Appl. Phys.*, vol. 102, no. 1, p. 014307, Jul. 2007.
- [14] D. B. Evans and R. D. Pehlke, "The Boron-Nitrogen Equilibrium in Liquid Iron," in *Transactions of the Metallurgical Society of AIME*, vol. 230, 1964, pp. 1657-1662.
- [15] C. Kowanda and M. O. Speidel, "Solubility of nitrogen in liquid nickel and binary Ni–Xi alloys (Xi=Cr, Mo, W, Mn, Fe, Co) under elevated pressure," *Scr. Mater.*, vol. 48, no. 8, pp. 1073–1078, Apr. 2003.
- [16] R. F. Abdulrahman and A. Hendry, "Solubility of nitrogen in liquid nickel-based alloys," *Metall. Mater. Trans. B*, 2001.

- [17] P. Villars, A. Prince, and H. Okamoto, Handbook of ternary alloy phase diagrams. ASM International, 1995.
- [18] J.-O. Andersson, T. Helander, L. Höglund, P. Shi, and B. Sundman, “Thermo-Calc & DICTRA, computational tools for materials science,” CALPHAD, vol. 26, no. 2, pp. 273–312, Jun. 2002.
- [19] S. Liu, “Experimental and Theoretical Studies of Hexagonal Boron Nitride Single Crystal Growth,” Kansas State University, Manhattan, Kansas, 2018.

Chapter 3 - hBN Size vs Solvent Properties

Choosing an appropriate solvent for hBN solution growth is critical for producing large, high quality hBN. The size of an hBN crystal is defined by the area of a single crystal domain in the a/b lattice directions (in-plane) and the thickness in the c lattice direction (out of plane). Maximizing crystal area is important because grain boundaries are a significant barrier to charge carrier mobility in devices. Maximizing thickness is important for applications such as neutron detectors [1], where the greater thickness improves collection efficiency, or in applications where hBN is used as an insulator, where greater thickness ensures that components are electrically isolated from one another. However, many modern applications call for thin films, so understanding how to minimize thickness without sacrificing on domain area is also important.

Many different solvents have been tested including Si [2], Ni [3], Ni-Mo [3], [4], Ni-Cr [4]–[7], Fe [8], Fe-Cr [9], [10], Co-Cr [4], Cu [11], Cu-Cr [12], Ba [13], and Mg [14] using a wide range of experimental parameters and producing varying results. In this work, five different solvents were tested: Ni-Cr, Co-Cr, Fe, Fe-V, and Cu. Each of these solvents meet a few requirements that make them useful for hBN solution growth.

First, they are all liquid at process conditions. For most of the solvents, this requires a process temperature well above 1000°C to ensure all components melt together. Solvents that are prone to vaporization at these high temperatures like Ba and Mg can only be used at high pressures, which keeps them liquid. The liquid state is necessary because the mass transport kinetics in a solid is too slow to be practical for synthesis of large hBN single crystals, and a gas phase system would fall into the category of a deposition technique like CVD or PVD, which have different use cases than solution growth.

Second, the solvent does not precipitate any solids other than hBN within the growth temperature range. The phase equilibria in some systems may favor a different material, making them undesirable for hBN solution growth. For example, in experiments with an Fe-V solvent conducted in this work, when the vanadium concentration was 30 mass%, VN precipitated instead of hBN, so lower vanadium concentrations were needed. Binary phase diagrams can help predict if any other solid phases might be stable during crystal growth. For example, the Co-Cr phase diagram is shown in Figure 25. With the same chromium concentration as used in Ni-Cr solvents (50 mass%), the system is well above the liquidus, even at the quench temperature (1500°C), making precipitation of Co-rich or Cr-rich phases unlikely during crystal growth. The highest chromium concentration that is still above the liquidus at 1500°C is 57 mass%, which is why 43/57 Co-Cr was tested as a solvent.

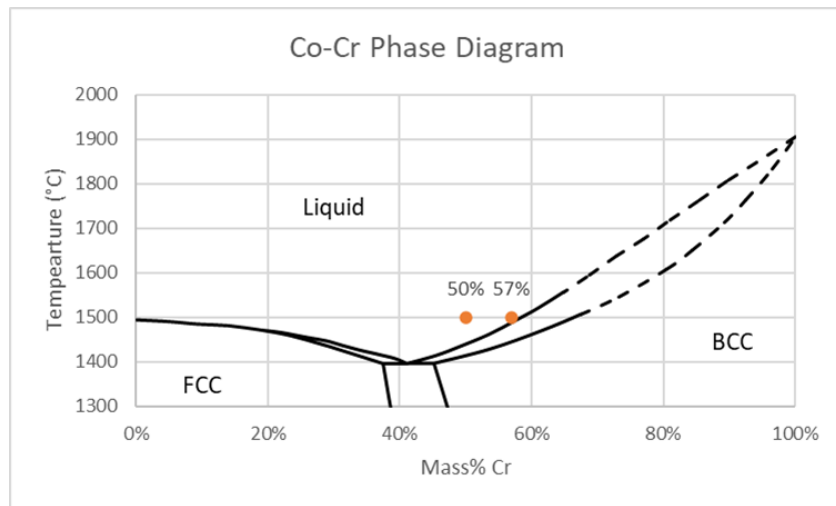


Figure 25 – Co-Cr phase diagram modified from ref. [15] with the two Co/Cr ratios used in this work highlighted. In both cases the system is still above the liquidus before the quench temperature (1500°C)

Third, the solvent can dissolve both boron and nitrogen. Molten metals are usually used as a solvent because they have a high enough boron solubility that it is unlikely to be a limiting factor in the process. Unfortunately, these solvents also typically have a low nitrogen solubility, and nearly every hBN solution growth researcher that has written about nitrogen solubility has

stated that increasing the nitrogen solubility of the solvent increases the size of hBN single crystals precipitated. This is mostly due to the claims of Kubota *et al* [3], [5], who observed that adding components to Ni that increased the nitrogen solubility of the solvent (first Mo, then Cr) increased the crystal size. When other researchers were successful with other high-nitrogen solubility solvents like Co-Cr [4], Fe-Cr [7], and Cu-Cr [12], the claim was cemented as fact. However, this was challenged by the great success of pure Fe as a solvent [8], which produced a highly-ordered hBN flake $\sim 4 \text{ cm}^2$ in area despite having a relatively low nitrogen solubility. This work challenges the idea even further by demonstrating that hBN of a reasonable size can be grown from pure copper despite having a nitrogen solubility that is nearly zero. Clearly there is more to optimizing hBN solution growth than maximizing nitrogen solubility and this chapter seeks to unravel the true effects of nitrogen solubility.

3.1 Synthesis and Optimization

The standard crystal growth process described in Section 1.4 was used in each of these experiments and only the composition of boron and solvent metals were adjusted. Table 3 summarizes the compositions tested, which are combined with the experiments using Fe that are detailed in Section 2.2 and summarized in Table 2. Two different Co/Cr ratios and three Fe/V ratios were tested as solvents to test how nitrogen solubility affects crystal growth with a consistent set of components rather than comparing entirely different solvents. Since Cr and V have a high affinity for nitrogen, increasing their concentration in the solvent significantly increases the nitrogen solubility of the system.

Table 3 – Composition of experiments to test effect of solvents

Solvent	Solvent Ratio (g/g)	Mass% B
Fe-V	70/30	2.5
	95/5	
	97/3	
	99/1	
Ni-Cr	1/1	4.0
Co-Cr	1/1	2.0
		4.0
		5.0
		6.0
	43/57	3.0
		4.0
		5.0
		6.0
Cu	---	0.25
		0.5
		0.75
		1.0
		2.0
		3.0

A range of boron concentrations were tested in the Co-Cr and Cu solvents to find the concentration that produced the largest crystals. Optical micrographs of the largest crystals grown in each experiment were taken and the boundaries of the crystal were traced manually in ImageJ to determine its area in square micrometers as shown in Figure 26. The largest crystal obtained in each experiment is used as a metric instead of the distribution of crystal areas as was done in Section 2.2 because it is much faster to quantify and still correlates to the optimal conditions, though less precisely. With these results (summarized in Table 4), the boron concentration in four of the five solvents used in this work have been optimized.

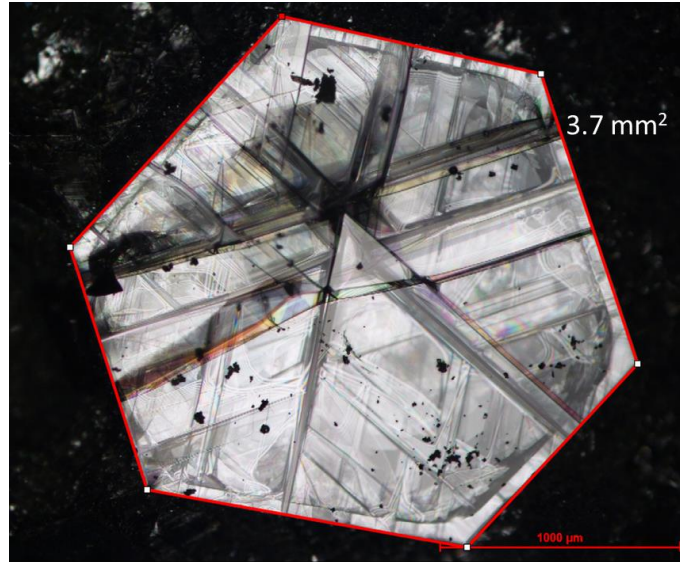


Figure 26 – Example of how hBN crystal area measured with ImageJ. Crystal is from a Ni-Cr solvent with 4.0 mass% boron.

Table 4 – Optimal Boron Concentrations for solvents used in this work and their nitrogen solubilities.

Solvent	Solvent Mass Ratio	Optimal B Conc. (mass %)	Nitrogen Solubility @ 1 bar, 1600 °C (mass%)
Ni/Cr	1/1	4.0*	1.2 [16]
Co/Cr	1/1	5.0	1.2 [†]
Co/Cr	43/57	4.0	1.9 [†]
Fe	N/A	2.3**	0.045 [17]
Fe/V	99/1-95/5	Not determined	0.055-0.15 [17]
Cu	N/A	0.75	$5.4 \cdot 10^{-5}$ [18]
* 4.0 mass% B was used in Ref. [19] because it produced the best results ** Determined with optimizations detailed in 0 † Extrapolated from data in the Ni-Co-Cr system (see text below)			

It is illustrative to compare solvents for hBN solution growth with their nitrogen solubilities, which are summarized in Table 4 above. Values for the nitrogen solubility in liquid Ni-Cr, Fe, Fe-V, and Cu exist in literature, but data is scarce on the Co-Cr system. However, Abdulrahman and Hendry [20] studied the nitrogen solubility in the Ni-Co-Cr system, which can be combined with Ni-Cr data from refs. [16] and [21] and Co data from ref. [22] to define a model for the solubility of the ternary system as shown in Figure 27a.

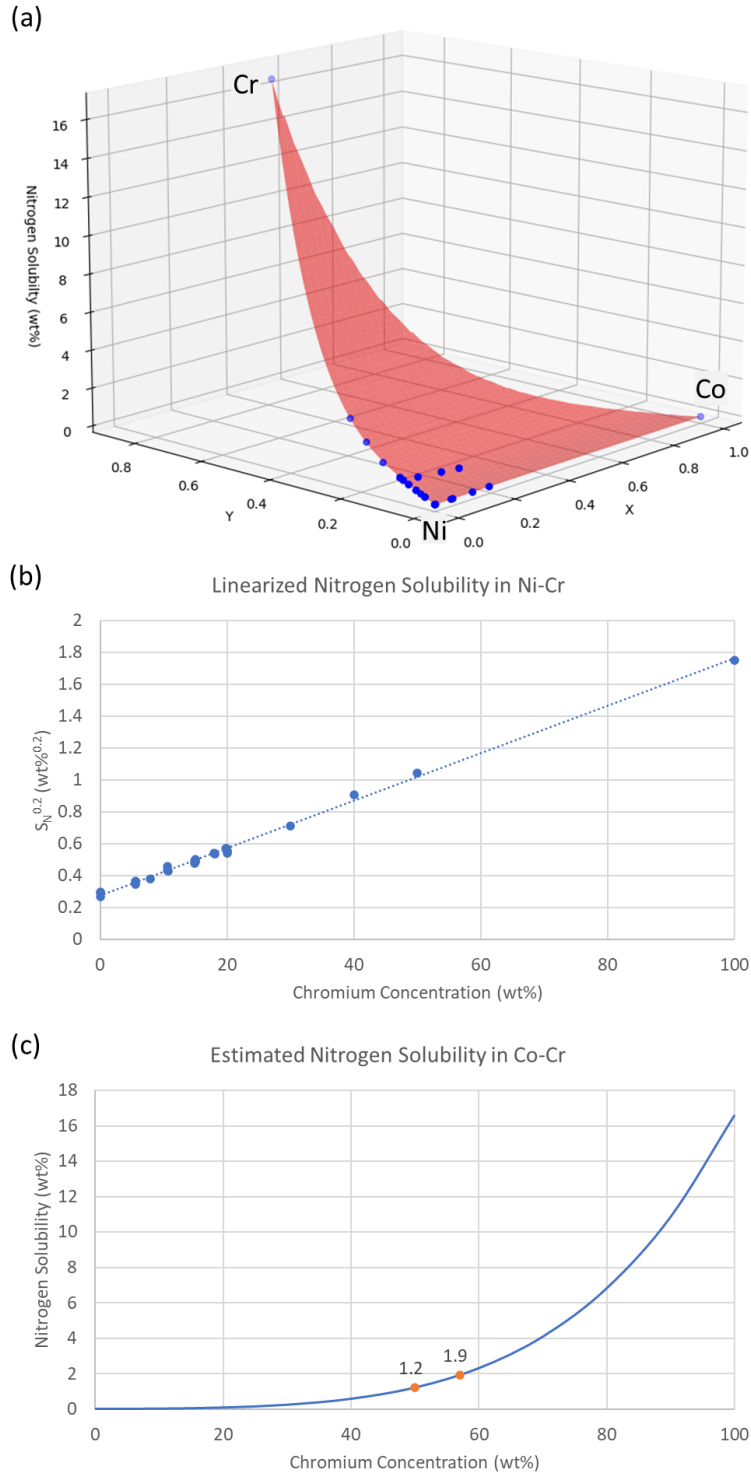


Figure 27 – a) Nitrogen solubility in the ternary Ni-Co-Cr system, vertical axis shows the nitrogen solubility versus composition at 1600°C and 1 bar. X and Y values calculated with Equation 3 & Equation 4. b) Nitrogen solubility in Ni-Cr raised to the 0.2 power to linearize it. c) Extrapolated nitrogen solubility curve for the binary Co-Cr system with the solubility of the two solvents tested in this work (1/1 and 43/57) highlighted.

The ternary data was mapped to cartesian coordinates with the following equations:

$$X = \frac{1}{2} \frac{2 \%Co + \%Cr}{\%Ni + \%Co + \%Cr} \quad \text{Equation 3}$$

$$Y = \frac{\sqrt{3}}{2} \frac{\%Cr}{\%Ni + \%Co + \%Cr} \quad \text{Equation 4}$$

Where %Ni, %Co, and %Cr are the mass percents of nickel, cobalt, and chromium, respectively. The model (Equation 5), shown as the red surface in Figure 27a, is defined to be linear in the “X” direction, following the linear trend of the nitrogen solubility in Ni-Co. In the “Y” direction, the model takes the form of a linear equation raised to the 5th power because the 5th root of the nitrogen solubility in Ni-Cr linearized the data (Figure 27b).

$$S_N = -0.124 + 0.00878 X + (0.326 + 1.65 Y)^5 \quad \text{Equation 5}$$

To estimate the nitrogen solubility in the Co-Cr system, this model was extrapolated to 0 mass% Ni, resulting in the curve shown in Figure 27c above. For the two Co-Cr solvent ratios tested in this work, the estimated nitrogen solubility is 1.2 and 1.9 mass% for 1:1 and 43:57 Co-Cr, respectively. Since these are extrapolations of experimental data, a percent error of $\pm 10\%$ is estimated for these values.

Figure 28 shows the optimal boron concentration for each solvent plotted versus its nitrogen solubility, which increases with increasing boron concentration. While it is not backed by any theory, a power law of the form

$$w_{B \text{ optimal}} = 4.0 * (w_{N \text{ solubility}})^{0.17} \quad \text{Equation 6}$$

fits this data very well, where $w_{B \text{ optimal}}$ is the optimal boron mass% and $w_{N \text{ solubility}}$ is the solubility of nitrogen at 1 bar and 1600°C in mass%. More data is needed on solvents with mid-range nitrogen solubilities to confirm this trend, but it still provides a starting point to optimize the boron concentration in future solvents. For example, the 95/5 Fe-V solvent tested in this

work but not optimized has a nitrogen solubility of 0.15 mass% at 1600°C and 1 bar, so would likely have an optimal boron concentration near 2.9 mass%.

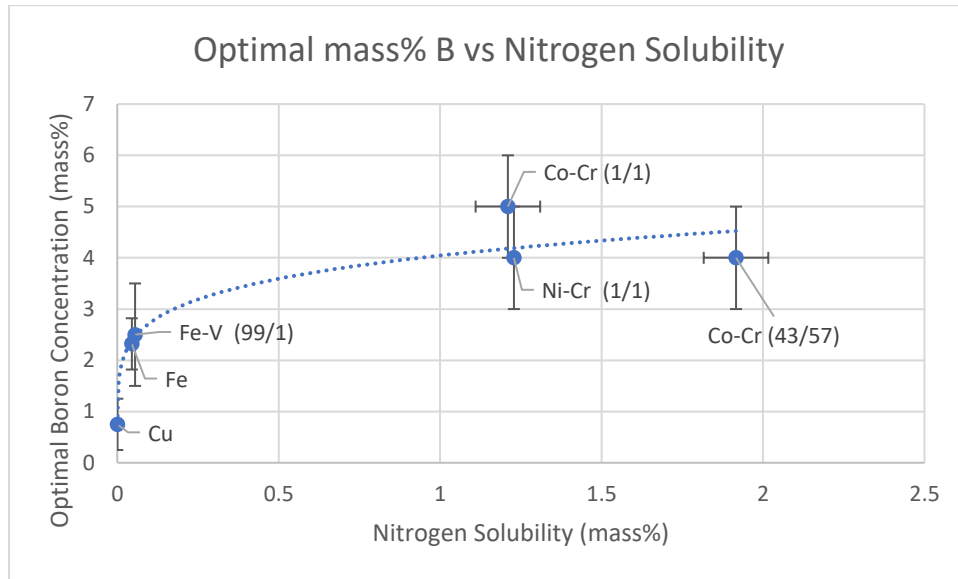


Figure 28 – Optimal boron concentration for each solvent plotted versus their nitrogen solubilities. Vertical error bars represent the estimated error in the optimal boron concentration of each solvent and horizontal error bars on Co-Cr points represent error in extrapolating their nitrogen solubilities from data in the Ni-Co-Cr system.

3.2 Experimental Results

Two different metrics for hBN single crystal size were considered in this work: the area of the largest single crystal and the distribution of crystal thickness. For crystal area, the solvents were compared using crystals grown with their optimal boron concentrations. The exceptions are the three Fe-V solvents tested, where optimal boron concentrations have not yet been determined.

Figure 29 shows optical micrographs of the largest single crystals in each of the solvents tested in this work with a graph of domain size versus nitrogen solubility. These values were determined in the same way as described in Section 3.1 to estimate the optimal boron concentration (see Figure 26). Though the largest domains obtained in experiments using low nitrogen solubility solvents (Fe or Fe-V) are slightly lower than those grown from high nitrogen

solubility solvents (Ni-Cr and Co-Cr) on average, the overlap between these two groups is too great to consider it a trend considering experimental variability. Thus, every solvent is capable of producing similarly-large domains given that they have been properly optimized.

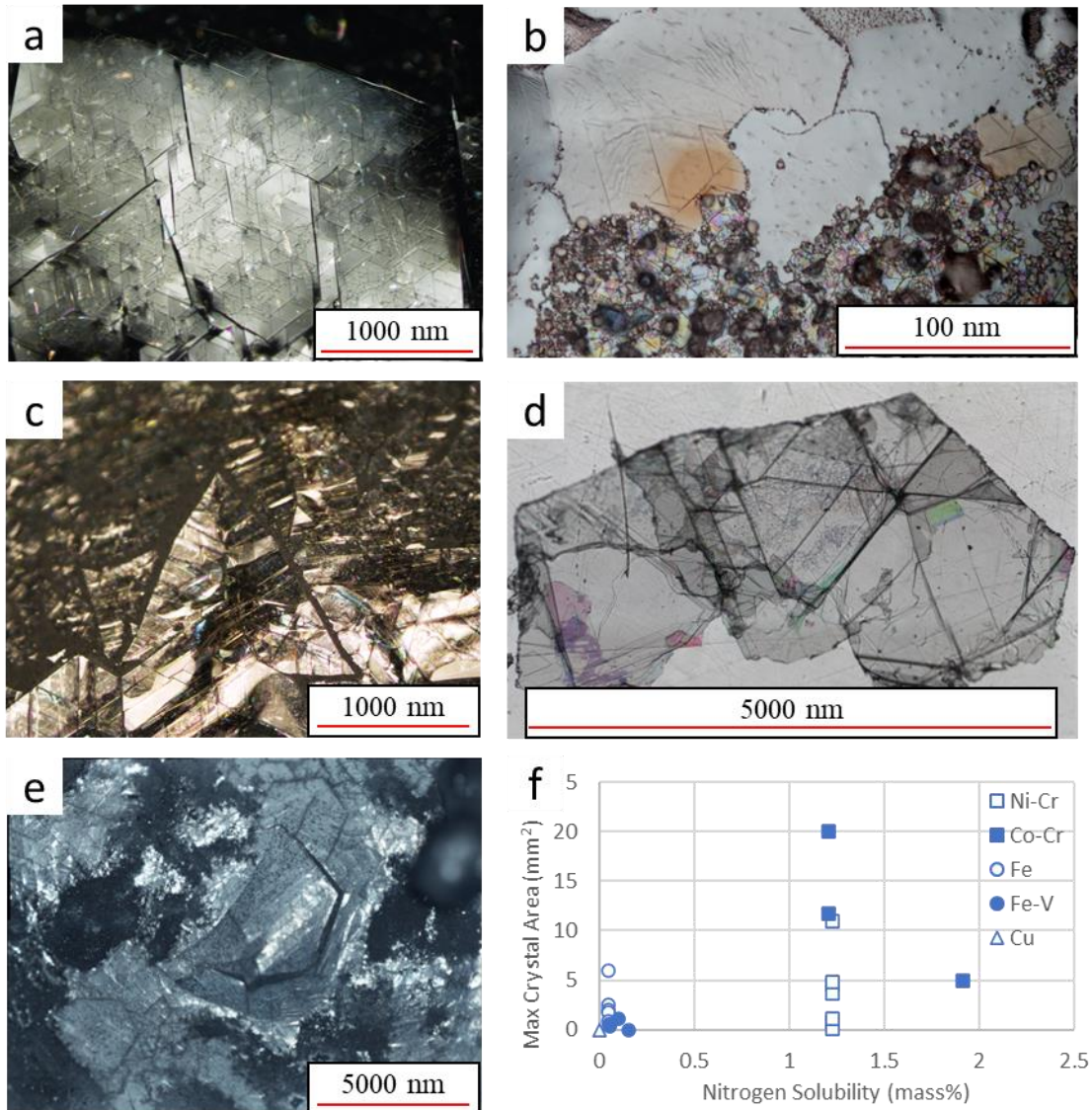


Figure 29 – Optical micrographs of the largest crystals produced in each of the five solvents tested in this work: Fe (a), Cu (b), Fe-V (c), Ni-Cr (d), and Co-Cr (e). f) Maximum crystal area plotted versus the nitrogen solubility of each solvent.

The thickness of crystals was measured by both surface profilometry and optical microscopy. For the former method, free standing hBN flakes were placed on glass slides and a

surface profilometer measured the thickness at the edge of each flake as illustrated in Figure 30a. To produce these free-standing flakes, hBN was mechanically exfoliated from the surface of the solidified metal flux using thermal release tape. However, this often cleaves crystals, skewing the data to be thinner than as-grown crystals and making it more difficult to determine how the solvent affects crystal thickness. To correct for this, crystals must be either exfoliated from the ingot without cleaving them or measured while they are still adhered to the ingot.

Attempts were made to dissolve the ingot in 70% nitric acid to release the crystals from the metal without damaging them. This was somewhat successful with Fe-B ingots, but it required etching for 2-3 days in nitric acid at room temperature to separate the crystals from the ingot. Furthermore, a unique feature of hBN flakes grown from Fe-B ingots was that they could frequently be exfoliated without cleaving the hBN, making dissolving the ingot unnecessary for accurately measuring crystal thickness. Ni-Cr-B ingots were largely unaffected by the nitric acid, even when the solution was boiling, making this an impractical way to release hBN from these ingots.

Instead, the thickness of as-grown hBN crystals still adhered to the ingot were measured with an optical microscope under 1000x magnification. Since the crystals are transparent, features on the bottom can be seen through the material. By focusing on the top, then the bottom and noting how much the microscope stage moved, the thickness of the crystal was estimated as illustrated in Figure 30b. Measurement of the stage position was determined by the numeric dial of the fine focus adjustment knob.

This process works on crystals grown from any solvent, so long as they are thick enough to accurately focus on the top and bottom of the crystal separately under 1000x magnification. It

is less precise than using a surface profilometer, but does not carry any risk of cleaving crystals, making it more accurate for measuring the thickness of as-grown crystals.

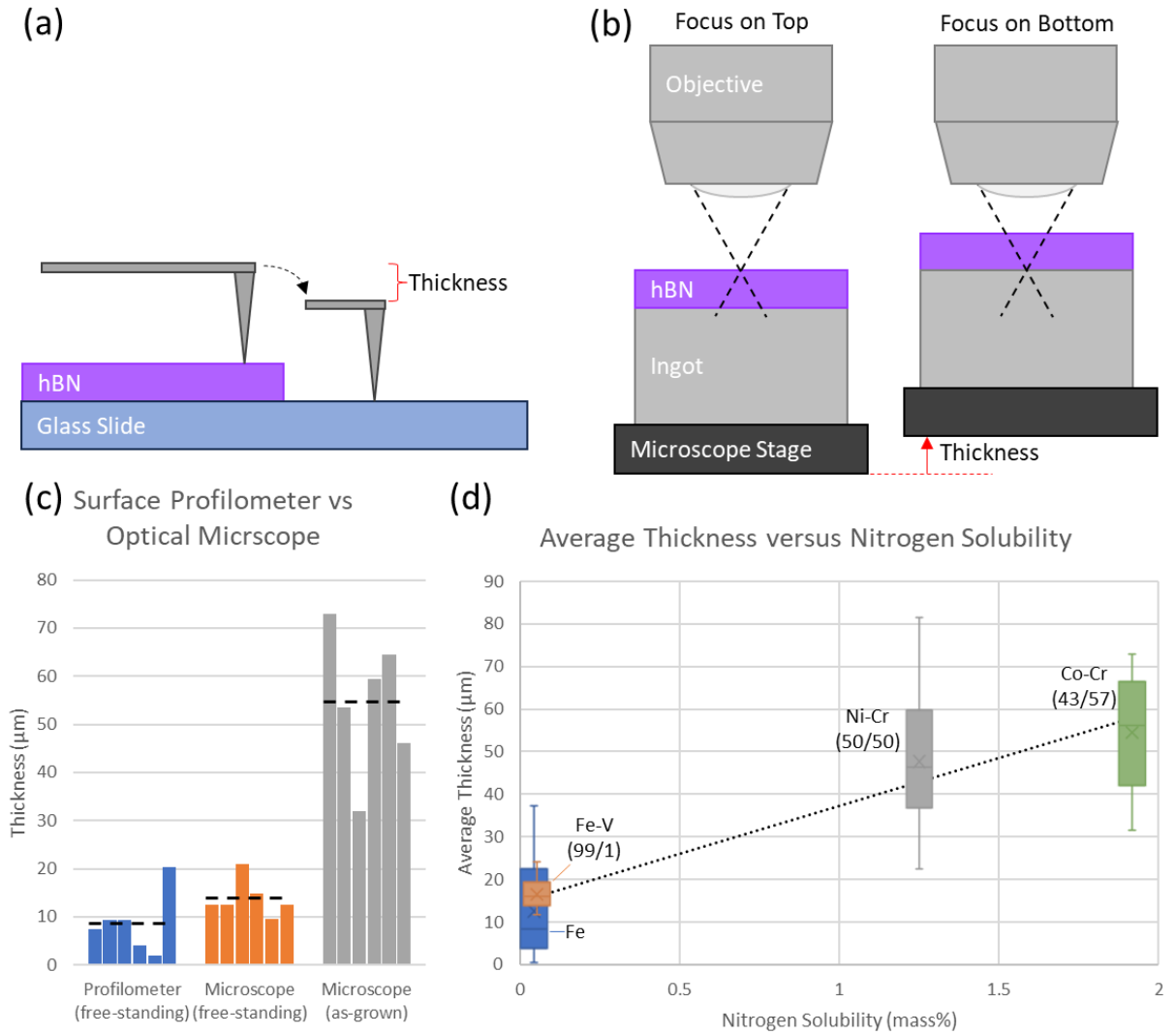


Figure 30 – a) Illustration of thickness of free-standing hBN flake measured with a surface profilometer, which drags a needle off the edge of a flake and measures the drop of the needle with a laser. b) Illustration of thickness of as-grown hBN flake measured with an optical microscope, which was focused on the top and bottom of the transparent crystals so the change in height of the stage measures thickness. c) Thickness of free standing hBN flakes as measured by both a surface profilometer and an optical microscope and as-grown hBN flakes as measured by an optical microscope from the same crystal growth experiment. d) Distribution of thickness of hBN grown from four different solvents shown with boxplots. Horizontal position of the boxplots determined by the nitrogen solubility of each solvent and the dotted line shows the trend of increasing thickness with increasing nitrogen solubility.

To ensure that estimating thickness with an optical microscope could be done consistently and accurately, measurements with both methods were made on random sets of crystals from the same 43/57 Co-Cr experiment. Figure 30c shows these measurements for three different cases: with a surface profilometer on free-standing flakes, with an optical microscope on free-standing flakes, and with an optical microscope on as-grown flakes still adhered to the ingot. The optical microscope consistently measured free-standing crystals to be thicker than those measured with the surface profilometer by about 5 μm on average. Taking the thicknesses measured by the surface profilometer as the “true” values, this indicates that the optical microscope slightly overestimates the thickness of hBN flakes. However, this overestimate is not large enough to account for the much larger thickness measured on as-grown crystals (55 μm on average). Instead, this shows that mechanical exfoliation from the ingot consistently reduces the thickness of the as-grown crystals.

Figure 30d shows boxplots of the distribution of thickness for four different solvents positioned by the nitrogen solubility of the solvent. The thickness of random sets of hBN single crystals still adhered to the solidified metal flux from each experiment were measured using an optical microscope as described above. Clearly, the thickness of the hBN flakes decreases with decreasing nitrogen solubility. hBN grown from pure copper could not be measured with this technique because they were too thin, which means that their thickness was substantially less than 5 μm and continues the trend of decreasing thickness with decreasing nitrogen solubility.

3.3 Effects of Nitrogen Solubility on hBN Growth

The common knowledge throughout the history of hBN solution growth research has been that the solvent with the highest nitrogen solubility produces the largest crystals, but the results presented in this work challenge that idea. As shown in Figure 29, the maximum area of

crystals are similar across all solvents despite having widely varying nitrogen solubilities, so long as each solvent's optimal boron concentration is used. As discussed in Chapter 2, assuming the solution has been saturated with nitrogen, the boron concentration controls how supersaturated or subsaturated the system is at the start of crystal growth, which in turn controls the nucleation rate of hBN single crystals. The more crystals that nucleate, the smaller they will be on average. The nitrogen solubility of the solvent is not directly a factor in the degree of supersaturation, so is not expected to affect the crystal size so long as the boron concentration has been properly optimized. An extreme example to demonstrate the importance (or lack thereof) of nitrogen solubility is hBN solution growth with a copper solvent.

Copper has a nitrogen solubility of 5.4×10^{-5} mass% at 1 bar and 1600°C, which is over 20,000x less than the 1/1 Ni-Cr solvent, but it can still grow hBN single crystals up to 0.01 mm² in area. Figure 31 a and b show optical micrographs of two collections of hBN single crystals from two different copper experiments, which have features that are commonly observed in hBN. They are transparent to visible light, have a hexagonal crystal habit, and have wrinkles in their interior that follow crystallographic directions. To further ensure that these are actually hBN crystals, cathodoluminescence (CL) spectroscopy was performed on them at room temperature with a 20 kV acceleration voltage and 30 μm aperture. Figure 31d shows the average CL spectrum within the area shown in Figure 31c, which has emission peaks that are characteristic of hBN: phonon replica peaks at 207-217 nm, stacking fault peaks at 217-248 nm, and point defect peaks at >248 nm (more details on what these peaks represent is provided in Section 4.2). Thus, the crystals grown in these experiments are certainly hBN rather than some other material.

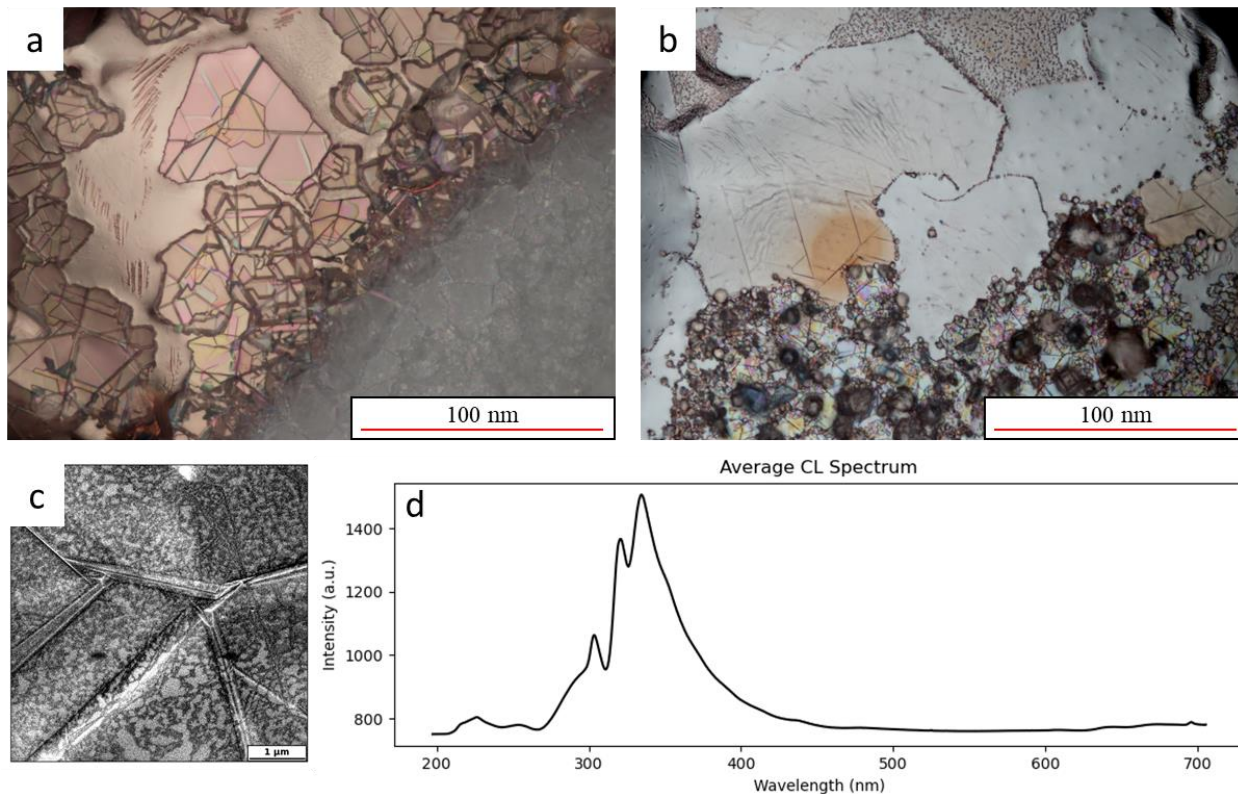


Figure 31 – a & b) Optical micrographs of hBN single crystals grown from a pure Cu solvent. c) SEM image of a Cu-grown hBN single crystal with wrinkles. d) Average cathodoluminescence spectrum of region shown in c) that shows peaks characteristic of hBN.

The hBN single crystals grown from Cu also continue the trend of decreasing thickness with decreasing nitrogen solubility, producing hBN with a thickness $<5 \mu\text{m}$, the thinnest of any solvent tested. This indicates that the nitrogen solubility, and thus the concentration of nitrogen in solution, is important for growth in the c-direction. To understand why, it is important to consider the mechanisms by which hBN can grow.

First, for molecular nitrogen to react with boron and form hBN, both elements must break their initial bonds. Dissolved boron exists as individual atoms in molten metals, fulfilling this requirement, but since its optimal concentration is more than double the solubility of nitrogen in all solvents (see Table 4) and the stoichiometry of B:N is 1:1, it will never be the limiting

reactant. When N_2 dissolves into molten metals, it also splits into individual atoms, making it available to react with the boron already dissolved in the solution.

Since nitrogen is the limiting reactant, its concentration in the solution dictates the kinetics of hBN crystal growth, which is a function of both the nitrogen solubility and the mass transport kinetics of N_2 dissolving into the solution and diffusing through it. Any reactions that occur near the gas-liquid interface will be insensitive to nitrogen solubility because nitrogen depleted by the formation of hBN can be quickly replenished by solvation of nitrogen from the gas. Reactions far from the gas-liquid interface will be much more sensitive to nitrogen solubility because it dictates the maximum nitrogen concentration in the solution. The higher the nitrogen concentration, the slower it will be depleted and the faster the reaction kinetics since nitrogen is the limiting reactant. What constitutes as “near” or “far” from the gas-liquid interface will depend heavily on the mass transport kinetics, which are difficult to predict in multicomponent solutions, but these concepts still provide a way to understand how nitrogen solubility affects thickness.

Crystal growth of hBN can take place in two different crystallographic directions, the *a/b* direction (in-plane, increasing the domain area) and the *c* direction (out of plane, increasing the thickness). The crystals grow at the surface of the solution such that their *a/b* direction is parallel to the surface as illustrated in Figure 32. Some fraction of hBN layers exist near the gas-liquid interface, so their growth is insensitive to nitrogen solubility for the reasons stated above (pathway 1 in Figure 32). The remaining layers exist far from the gas-liquid interface, so their growth is dependent on nitrogen solubility (pathway 2 in Figure 32). Thus, in low nitrogen solubility solvents like Fe or Cu where growth far from the gas-liquid interface would be inhibited, only a thin layer of hBN is capable of growing and the flake becomes thin overall.

Conversely, in high nitrogen solubility solvents like Ni-Cr and Co-Cr, growth in all directions is relatively unimpeded, so thicker crystals can be formed.

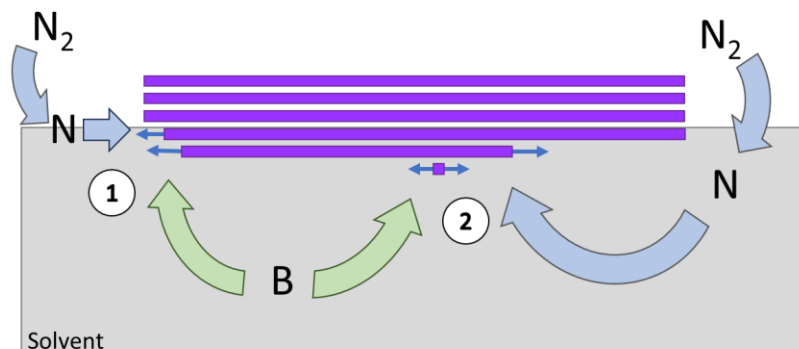


Figure 32 – Illustration of pathways that nitrogen can take to grow hBN single crystals. 1) Nitrogen dissolves into the solvent at the gas-liquid interface and immediately reacts with boron to grow hBN layers near the surface. 2) Nitrogen dissolves into the solvent and diffuses into the bulk where it reacts with boron to grow hBN layers far from the surface or nucleate new hBN layers.

3.4 References

- [1] A. Maity, T. C. Doan, J. Li, J. Y. Lin, and H. X. Jiang, “Realization of highly efficient hexagonal boron nitride neutron detectors,” *Appl. Phys. Lett.*, vol. 109, no. 7, p. 072101, Aug. 2016.
- [2] T. Ishii and T. Sato, “Growth of single crystals of hexagonal boron nitride,” *J. Cryst. Growth*, vol. 61, no. 3, pp. 689–690, Apr. 1983.
- [3] Y. Kubota, K. Watanabe, O. Tsuda, and T. Taniguchi, “Deep Ultraviolet Light-Emitting Hexagonal Boron Nitride Synthesized at Atmospheric Pressure,” *Science*, vol. 317, pp. 932–934, 2007.
- [4] M. Onodera et al., “Hexagonal boron nitride synthesized at atmospheric pressure using metal alloy solvents: Evaluation as a substrate for 2D materials,” *Nano Lett.*, vol. 20, no. 1, pp. 735–740, Jan. 2020.
- [5] Y. Kubota, K. Watanabe, O. Tsuda, and T. Taniguchi, “Hexagonal boron nitride single crystal growth at atmospheric pressure using Ni–Cr solvent,” *Chem. Mater.*, vol. 20, no. 5, pp. 1661–1663, Mar. 2008.
- [6] T. B. Hoffman, B. Clubine, Y. Zhang, K. Snow, and J. H. Edgar, “Optimization of Ni–Cr flux growth for hexagonal boron nitride single crystals,” *J. Cryst. Growth*, vol. 393, pp. 114–118, May 2014.
- [7] S. Liu, R. He, L. Xue, J. Li, B. Liu, and J. H. Edgar, “Single Crystal Growth of Millimeter-Sized Monoisotopic Hexagonal Boron Nitride,” *Chem. Mater.*, vol. 30, pp. 6222–6225, 2018.
- [8] J. Li et al., “Hexagonal Boron Nitride Crystal Growth from Iron, a Single Component Flux,” *ACS Nano*, vol. 15, no. 4, pp. 7032–7039, Apr. 2021.
- [9] S. Liu et al., “Large-scale growth of high-quality hexagonal boron nitride crystals at atmospheric pressure from an Fe–Cr flux,” *Cryst. Growth Des.*, vol. 17, no. 9, pp. 4932–4935, Sep. 2017.

- [10] J. Li et al., “Single crystal growth of monoisotopic hexagonal boron nitride from a Fe–Cr flux,” *J. Mater. Chem. C Mater. Opt. Electron. Devices*, vol. 8, no. 29, pp. 9931–9935, 2020.
- [11] B. Clubine, “Synthesis and characterization of bulk single crystal hexagonal boron nitride from metal solvents,” MSc, Kansas State University, Manhattan, KS, 2010.
- [12] N. Zhang, N. Yang, W. Wang, X. Zhong, and X. Chen, “Growth of hexagonal boron nitride crystals at atmospheric pressure from Cu-Cr flux,” *J. Cryst. Growth*, vol. 562, p. 126074, 2021.
- [13] T. Taniguchi and K. Watanabe, “Synthesis of high-purity boron nitride single crystals under high pressure by using Ba–BN solvent,” *J. Cryst. Growth*, vol. 303, no. 2, pp. 525–529, May 2007.
- [14] N. D. Zhigadlo, “Crystal growth of hexagonal boron nitride (hBN) from Mg–B–N solvent system under high pressure,” *J. Cryst. Growth*, vol. 402, pp. 308–311, Sep. 2014.
- [15] P. Wang, M. C. Peters, U. R. Kattner, K. Choudhary, and G. B. Olson, “Thermodynamic analysis of the topologically close packed σ phase in the Co-Cr system,” *Intermetallics (Barking)*, vol. 105, pp. 13–20, 2019.
- [16] C. Kowanda and M. O. Speidel, “Solubility of nitrogen in liquid nickel and binary Ni–Xi alloys (Xi=Cr, Mo, W, Mn, Fe, Co) under elevated pressure,” *Scr. Mater.*, vol. 48, no. 8, pp. 1073–1078, Apr. 2003.
- [17] F. Ishii and T. Fuwa, “Effect of alloying element on the solubility of nitrogen in liquid iron,” *Tetsu To Hagane*, vol. 68, no. 10, pp. 1560–1568, 1982.
- [18] A. M. Mohd Noor, N. H. Muhd Nor, and S. Yokoyama, “Solubility of nitrogen gas into molten copper at temperature range of 1,993 K to 2,443 K,” *High Temp. Mater. Processes*, vol. 36, no. 10, pp. 1035–1038, Oct. 2017.
- [19] S. Liu, “Experimental and Theoretical Studies of Hexagonal Boron Nitride Single Crystal Growth,” Kansas State University, Manhattan, Kansas, 2018.
- [20] R. F. Abdulrahman and A. Hendry, “Solubility of nitrogen in liquid nickel-based alloys,” *Metall. Mater. Trans. B*, 2001.
- [21] J. Siwka, “Equilibrium Constants and Nitrogen Activity in Liquid Metals and Iron Alloys,” *ISIJ Int.*, vol. 48, no. 4, pp. 385–394, 2008.
- [22] W. Betteridge, “The Properties of Metallic Cobalt,” *Progress in Materials Science*, vol. 24, pp. 51–142, 1979.

Chapter 4 - Understanding Defects in hBN

Previous chapters have focused on how to maximize the grain size of hBN single crystals, which is important because grain boundaries are a significant barrier to charge carrier mobility in devices. However, grain boundaries are just one variety of crystal defects that are frequently visible in optical microscopy, so are relatively easy to study. Many other defects exist in hBN single crystals that may affect device performance but require other techniques to detect and study. These include dislocations, stacking faults, vacancies, and impurities or large defect structures like the wrinkles discussed in section 4.2.3. This chapter discusses the variety of defects in hBN single crystals grown in this work, how they can be identified, and what process parameters caused them to form.

4.1 Impurity Sources and Sinks

Impurities in hBN introduce energy levels into the band gap, which change the electronic properties of the material and can be both beneficial and detrimental to device performance. The most common impurities that are unintentionally present in hBN are carbon and oxygen. Carbon impurities in hBN can function as single photon emitters in the visible range for use in quantum photonic devices [1] or as either an electron donor or acceptor depending on whether the carbon occupies a boron or nitrogen site, respectively [2]. However, carbon has also been shown to degrade carrier mobility in hBN/graphene heterostructures [3]. Oxygen impurities will act as electron donors [4], [5], but can also oxidize the solvent, interfering with hBN crystal growth and potentially preventing hBN from growing at all.

Carbon and oxygen impurities can have several sources in atmospheric pressure solution growth of hBN including the boron and solvent source materials, the nitrogen and hydrogen gases, ambient air that leaks into the system, and the alumina crucible that contains the solution.

Figure 33a shows the concentration of carbon and oxygen in the boron and solvent source materials (summarized in Table 5) used in this work to grow hBN as measured by inert gas fusion at Applied Technical Services, Inc. Two different sources of iron were tested as solvents to directly compare how differences in impurity content of the source material will affect the purity of the final hBN crystals.

Table 5 – Vendors and rated purity of source materials used in experiments.

Source Material	Company	Rated Purity (metals basis)
Fe (high purity)	ESPI	99.995%
Fe (low purity)	Alfa Aesar	99%
V	ESPI	99.8%
Ni	Alfa Aesar	99.7%
Cr	Alfa Aesar	99%
B	Cerac	99%
HPBN	Momentive	99%

To test how the impurity content of the crystal growth solution was affected by the impurity content of the source materials, four ingots formed after standard crystal growth experiments (summarized in Table 6) were measured by chemical analysis at Applied Technical Services, Inc. The carbon content and the oxygen content of these ingots compared to their expected concentrations in Figure 33 b and c, respectively. The expected concentration is calculated by summing the impurity concentrations from the source materials, weighted by their concentration in the ingot. For example, the experiments using Fe as a solvent contained 2.5 mass% B, which contains ~1 mass% oxygen, so the boron is expected to contribute ~0.025 mass% oxygen to the ingot. These calculations assume that all the impurities originate from the source materials and are not removed from the system during the process.

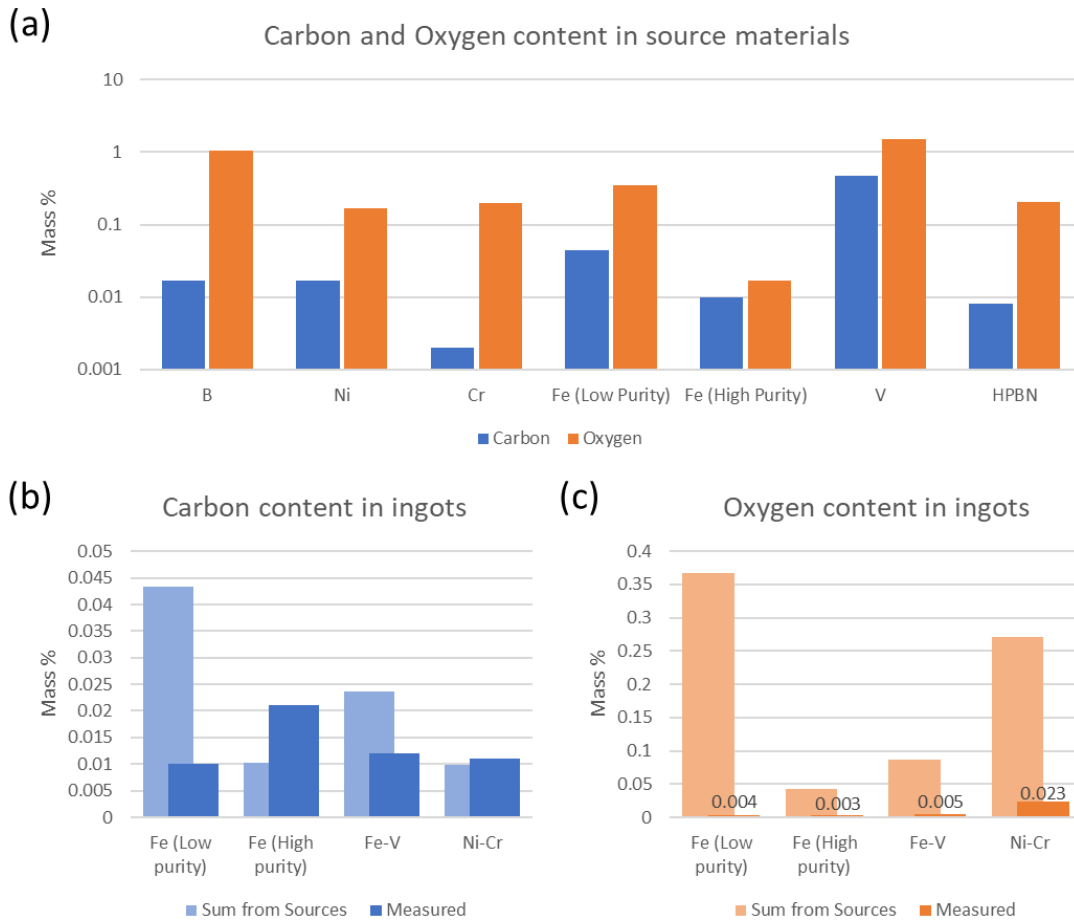


Figure 33 – Carbon and oxygen impurity content in source materials (a) and ingots (b and c). Expected impurity concentrations calculated by summing the carbon and oxygen concentrations from the source materials used to make them, scaled by their relative amounts.

Table 6 – Composition of source materials in ingots tested with chemical analysis.

Ingot	Boron		Solvent 1		Solvent 2	
	Mass%	Source	Mass%	Source	Mass%	Source
Fe (high purity)	2.5	B Powder - Cerac	97.5	Fe Powder - ESPI	--	--
Fe (low purity)	2.5	B Powder - Cerac	97.5	Fe Powder - Alfa Aesar	--	--
Fe-V	2.5	B Powder - Cerac	94.6	Fe Powder - ESPI	2.9	V Powder - ESPI
Ni-Cr	--	HPBN - Momentive	50	Ni Powder - Alfa Aesar	50	Cr Powder - Alfa Aesar

For oxygen, this assumption is clearly invalid because the oxygen concentration measured in the ingots is 1-2 orders of magnitude lower than the expected concentration for all ingots, indicating that most of the oxygen is removed during the crystal growth process. The large reduction in oxygen concentration from the source materials in all samples is likely due to a couple major oxygen sinks present in the process used in this work. A stream of hydrogen gas is added to the furnace atmosphere in all experiments primarily to react with oxygen and oxides present in the solution and carry oxygen out of the system as water vapor. Boron oxide (B_2O_3) is the least likely to be reduced this way because it is the most stable oxide of the materials used, but it fortunately has a relatively high vapor pressure (~ 0.003 bar at $1550^\circ C$ [6], [7]), providing another sink for oxygen by sweeping evaporated boron oxide out of the system.

For carbon, the expected and measured concentrations are much closer, but the origins of their differences is unclear. In the ingot produced with high purity iron, the carbon concentration is approximately double the amount from the source materials, suggesting that this experiment had a carbon source that is unaccounted for. In the ingot produced with low purity iron, the carbon concentration is approximately a quarter of the amount from the source materials, suggesting that this experiment had a carbon sink that is unaccounted for. Some additional carbon sources could be contamination in the alumina crucible and volatile organics carried into the growth atmosphere from the vacuum system. A couple carbon sinks could be carbon reacting with either hydrogen or oxygen to produce methane or carbon monoxide, respectively, that is then swept from the system by the flowing gas phase. The latter reaction is more favorable and has been demonstrated in hBN solution growth research [8], which may explain the discrepancy between the carbon content in the high and low purity Fe. The high oxygen concentration in the

low-purity Fe could react with its high carbon concentration to eliminate both impurities from the solution while the low oxygen concentration in the high-purity Fe could not.

Since hBN grows from the solution, any impurities present in the solution will have a chance of incorporating into the hBN crystal, either by substituting for boron or nitrogen or intercalating between monolayers of hBN. However, crystal growth in general is a purification mechanism, so the impurity concentration in hBN crystals will be significantly lower than in the solution. To quantify this, samples of hBN grown from Fe, Fe-V, and Ni-Cr were analyzed by Eurofins EAG using secondary ion mass spectrometry (SIMS) to measure the impurity content of carbon and oxygen present within the crystals. In all cases, the impurities were below the detection limit of $<2E16$ atoms/cm³ (<0.4 ppm) for carbon and $<2E17$ atoms/cm³ (<4 ppm) for oxygen, suggesting that the level of purity achieved in the process is already sufficient for producing highly pure crystals.

4.2 Classification of Defects

Using cathodoluminescence (CL) spectroscopy, a variety of defects were detected: dispersed defects, spots, wrinkles, and invisible lines. Dispersed defects broadly represent any defects that contributed to defect emission in CL spectra but are spread out across the region mapped rather than concentrated on physical features. Spots are small points in the CL map that have strong emission in a narrow wavelength band. Wrinkles are large defect structures appearing as lines along crystallographic directions that have a topography reminiscent of wrinkled paper. Invisible lines are spectral features that trace thin lines in particular wavelength bands, but do not appear in optical microscopy or SEM images. This section discusses how these defects are identified and classified with CL spectroscopy and describes the properties and

structure of each of category of defects with insights into how they formed and how they might be eliminated.

4.2.1 Characterizing Defects with CL Spectroscopy

Cathodoluminescence (CL) spectroscopy was the primary tool used to quantify and analyze defects, so it is imperative to have a solid understanding of what the various spectral features in the CL spectrum of a hBN sample represent. Prior photoluminescence (PL) spectroscopy studies of hBN [9] provide a good starting point to classify the spectral features of light emitted by hBN. Excitons in hBN recombine by emitting deep UV photons in the range 5.7-6.0 eV (207-217 nm). These are the intrinsic peaks of hBN resulting from the phonon-assisted relaxation of electrons across the indirect band gap (>6 eV), called “phonon replicas”. All other peaks are associated with defects in the material. In the 5-5.7 eV (217-248 nm) range, the emission is associated with bound excitons formed in dislocations, lattice defects, and stacking

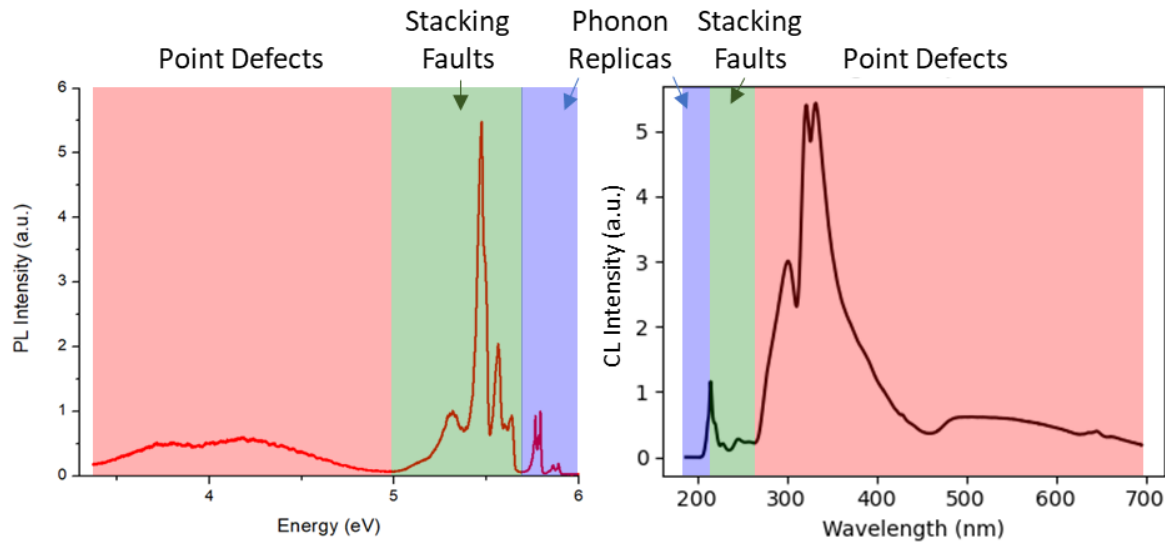


Figure 34 - Comparison of a UV-PL spectrum (left) acquired with 196 nm excitation at 9K and a CL spectrum (right) acquired at room temperature with an acceleration voltage of 10 kV. Both techniques show emission in the same basic spectral regions across the entire UV-Vis range: phonon replicas (blue), stacking faults/dislocations (green) and point defects/color centers (red)

faults while peaks below 5 eV (>248 nm) are attributed to direct emission from point defects and color centers. These ranges can be easily mapped onto a CL spectrum as shown in Figure 34, providing a straightforward way to deduce the basic structure and composition of defects that cause spatially localized defect emission.

A primary benefit of CL spectroscopy over PL spectroscopy is its high spatial resolution, which allows high-resolution hyperspectral CL maps to be created like the one shown at the top of Figure 35. These maps are created by collecting a CL spectrum at every pixel in a region. As an example, the spectrum in the top right of Figure 35 is from the center pixel of the CL map. This allows patterns in the spatial distribution of spectral features to be identified and correlated to specific defects as is discussed in following sections. In this example the spectrum is quite noisy, but another benefit of collecting CL data as a hyperspectral map is that it can be denoised using Singular Value Decomposition (SVD).

SVD is a variety of Blind Source Separation (BSS) and falls under the broad umbrella of machine learning. At a high level, the goal of the algorithm is to find groupings of features ("components") in the data that are as different as possible from each other (mathematically: orthogonal to each other) and will recreate the original data if they are summed together. When applied to hyperspectral CL maps, it produces a series of spectra ("factors") paired with maps ("loadings") that together make each component as shown in the middle right of Figure 35. Each factor represents a distinct spectral pattern pulled from the data and the value at each pixel in the loading represents how much the factor contributes to the original spectrum at that pixel. The first 4 components in this example clearly highlight specific features in the CL map, but components 4, 5, and onward (not shown) all represent the noise that was present in the original data. Therefore, by excluding the "noise" components and summing the remaining components,

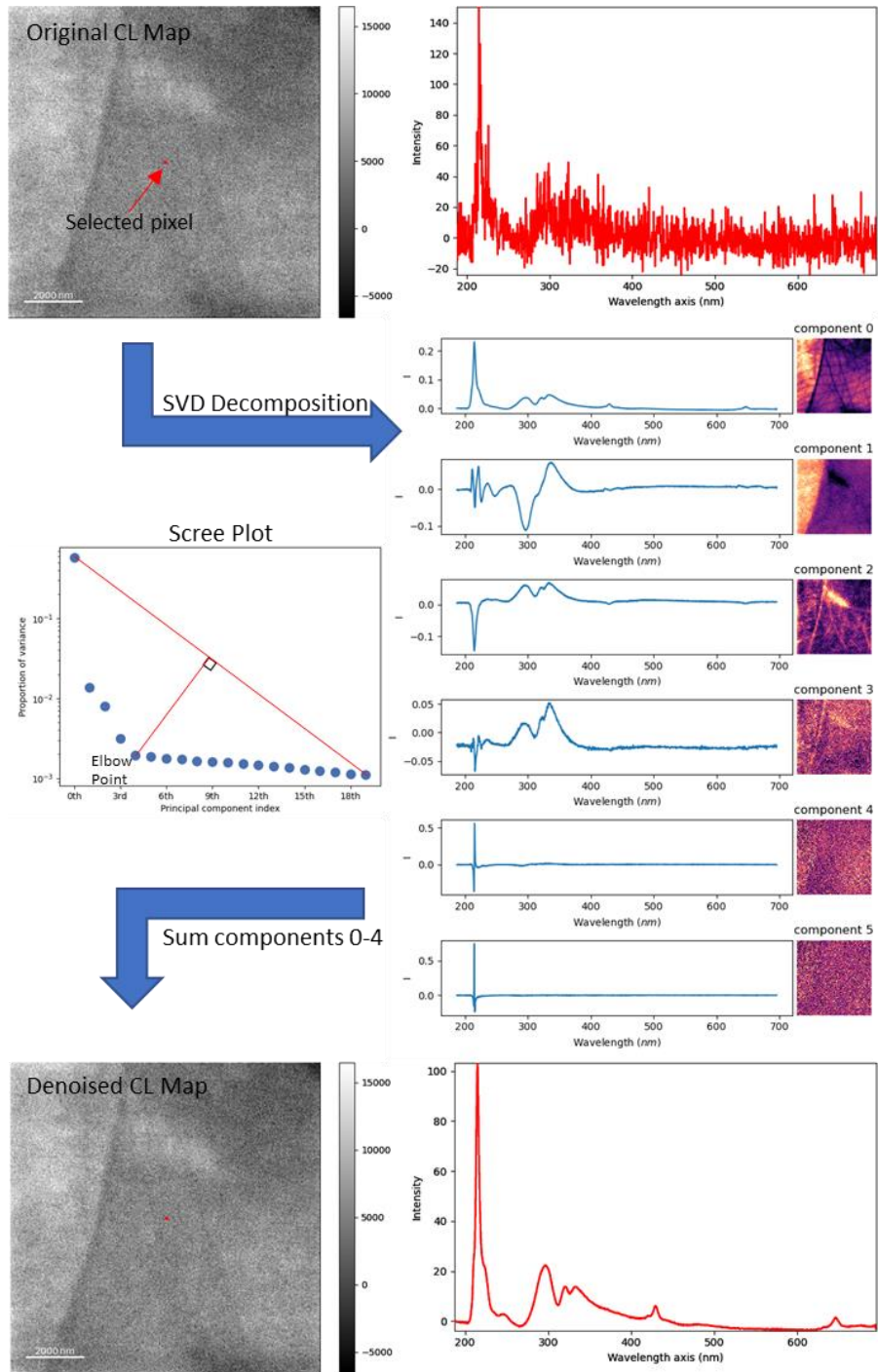


Figure 35 – Example of how a hyperspectral CL map is denoised using SVD decomposition. Top left – Averaged CL map of original data, with the central pixel highlighted in red. Top right – CL spectrum at that pixel. Middle right – First 6 components of SVD decomposition on the original CL map. Middle left – Scree plot of the explained variance versus the component index. The elbow point is the point furthest from a line connecting the first and last components and represents the last significant component. Bottom left – Averaged CL map of denoised data calculated by summing all the SVD components up to the elbow point, with the central pixel highlighted in red. Bottom Right – Denoised CL spectrum at that pixel.

a new hyperspectral map can be created with dramatically improved signal to noise as shown in the bottom of Figure 35. For consistency between CL maps, the decision on what components to exclude can be determined automatically by using a scree plot of the explained variance versus the component index as shown in the middle left of Figure 35. The “elbow point”, the point furthest from a line connecting the first and last components, represents the last significant component which is the first noise component in this example.

Defects can also be identified with SVD applied to CL maps, but other algorithms are typically better for this purpose. In Figure 35, components 0 and 2 both highlight “invisible lines” (discussed in section 4.2.3), but the spectra are difficult to interpret. Non-Negative Matrix Factorization (NMF), another variety of BSS, works similarly to SVD but mandates that all components are positive, which tends to produce spectra that are more realistic. An example of NMF is shown in Figure 36 (left), which was performed on the data presented in Figure 35. The spectra in each of these components show specific peaks that are correlated with specific regions and patterns, but it can be made more interpretable through Independent Component Analysis (ICA). ICA is yet another variety of BSS that operates on the results of NMF (or another BSS algorithm), an example of which is shown in Figure 36 (right). Here, we can identify the physical meaning of each component. Component 0 represents the noise in the CL spectrum, Component 1 represents the base material that is mostly free of defects, Component 2 reveals that the domain on the left has an increase in emission at 221 nm and 335 nm, and component 3 reveals that the invisible lines emit in the ranges 221-265 nm and 310-400 nm are the primary source of emission at the peak centered on 295 nm. This separation is useful because it allows spectral features to be correlated to physical defects. If the physical nature of the defects can be determined through more rigorous analysis of the material such as what is described in sections 4.2.3 and 4.2.3, other

materials that exhibit the same spectral patterns can be concluded to have the same defects without needing to go through the same rigorous analysis. The code written to perform these calculations and analyses is given in Appendix B.1.

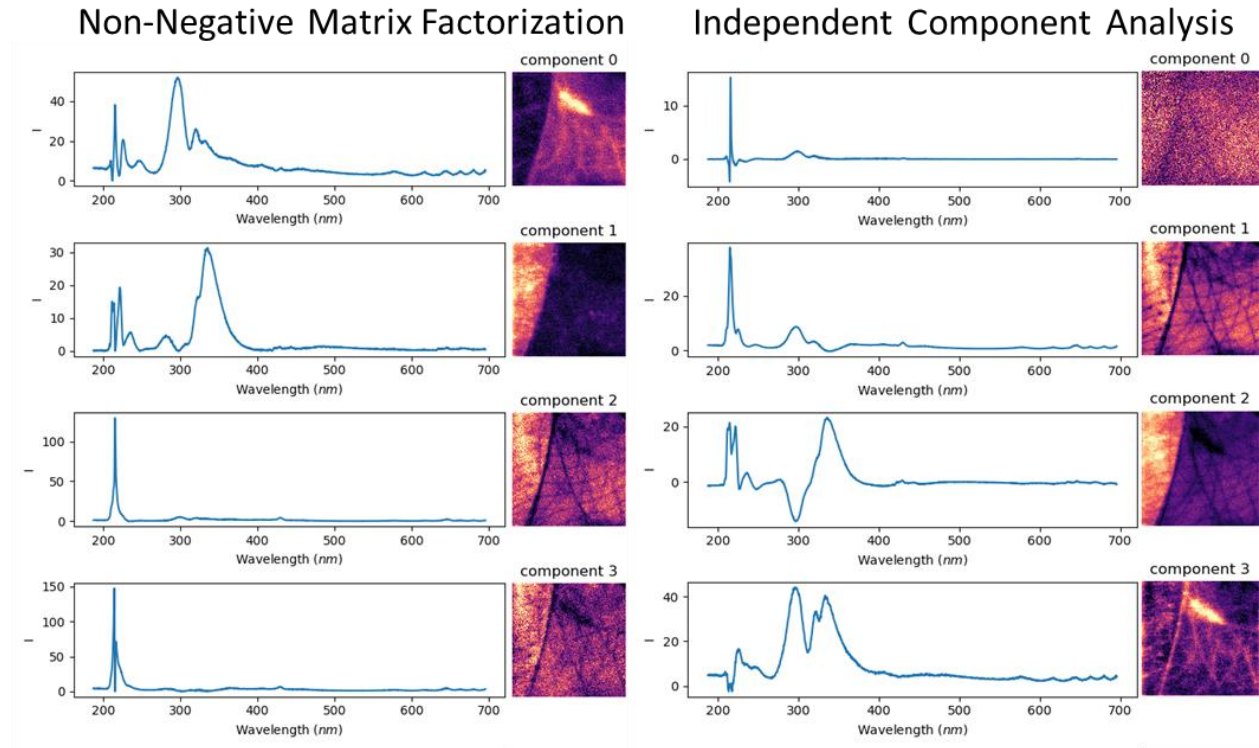


Figure 36 – Example of Non-Negative Matrix Factorization (NMF) and Blind Source Separation (BSS) performed on the data presented in Figure 35. The number of components here were set equal to the elbow point from SVD.

4.2.2 Spots

Spots are classified as small points in the CL map that have strong emission in a narrow wavelength band and are notable due to their potential to be color centers. Color centers are important for quantum information technology due to their ability to become optically-addressable qubits [10]. Therefore, determining which process parameters cause them to form will be beneficial for developing a reliable method to create them. In this work, spots that may be color centers were observed in two wavelength ranges as shown in Figure 37. In Figure 37a, faint

spots are visible at wavelengths near 320 nm, which falls in the same range as the color centers presented in refs. [11] and [12]. In Figure 37b, the small spot near the bottom of the map only appears in a very narrow wavelength band near 440 nm. In Figure 37c, many small spots across the entire region emit in the range 425-480 nm. Both of these spots fall in the same wavelength range as the blue color centers presented in ref. [12]. More work is necessary to positively identify these spots as color centers and to correlate them to process parameters, but they are strong evidence that color centers are formed naturally during the crystal growth process used in this work.

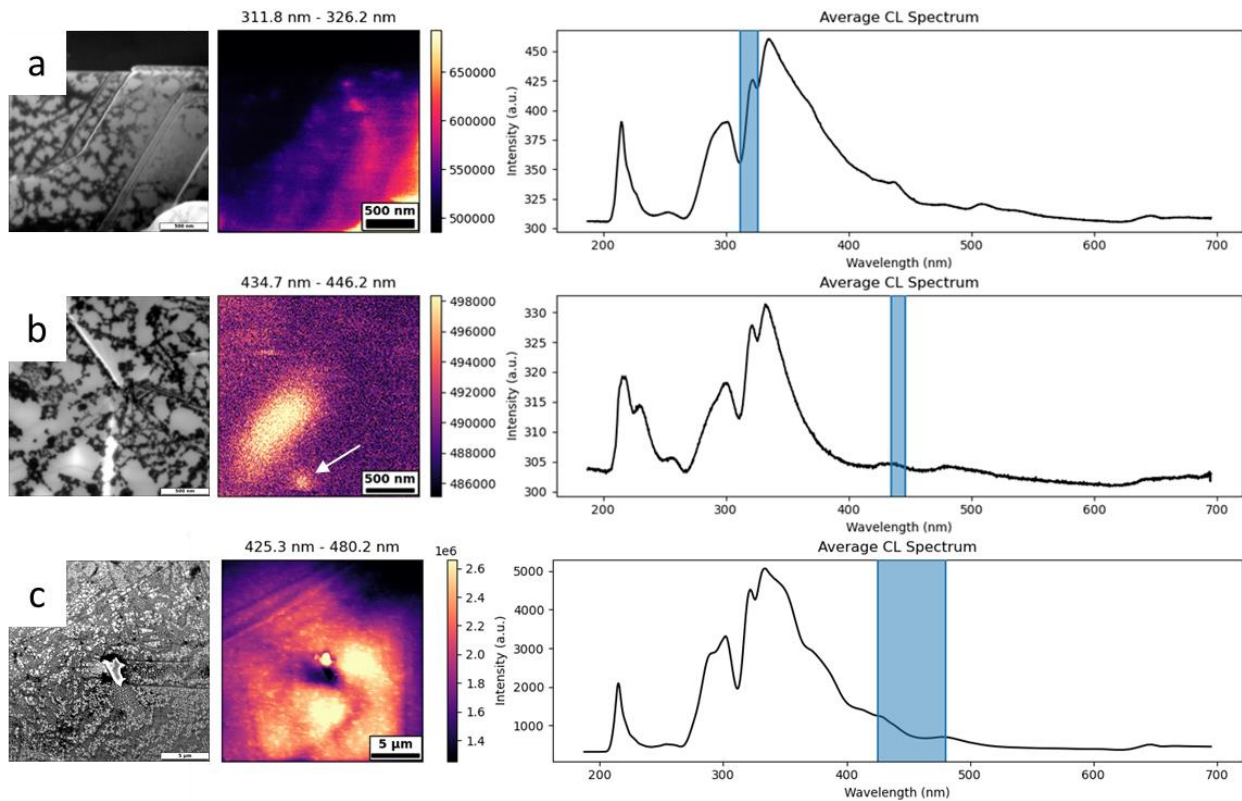


Figure 37 – Three examples of spots observed in hBN crystals using CL spectroscopy. Each example is shown with an SEM image (left), a CL map within a selected range (middle), and the average CL spectrum of the imaged region with the selected range highlighted (right) a) Steps on the edge of a crystal that exhibited faint spots near 320 nm. b) Mostly smooth region that showed two spots – the larger had increased emission across the entire wavelength range and the smaller only emitted in a narrow band near 440 nm. c) A smooth region that showed many small spots speckled across the entire area that emitted in the range 425-480 nm.

However, not every spot that appears in CL data is a color center. For example, the large spot in Figure 37b showed elevated emission across the entire spectral range, not just in the selected range. This suggests that it is formed by a variety of defects that emit at many different wavelengths rather than being a simple point defect. Furthermore, its relatively large size and oblong shape suggest that the emission is spread across multiple lattice defects rather than confined to a single point defect, as is the case for color centers.

4.2.3 Wrinkles

Wrinkles are of particular interest because they are visible with optical microscopy and cause confusion in identifying grain boundaries. They form highly ordered triangles along crystallographic directions (Figure 38 b & c) that can span several millimeters before a shift in alignment occurs (Figure 38a). With only optical microscopy, it is not clear if the smooth regions bounded by wrinkles are single crystal domains that formed independently and fused into a polycrystalline solid or if they are crystallographically oriented such that they are (or were) parts of a much larger single crystal. Based on TEM data, the wrinkles are hypothesized to be akin to wrinkles in a piece of paper and formed by plastic deformation during crystal growth on top of the metal melt.

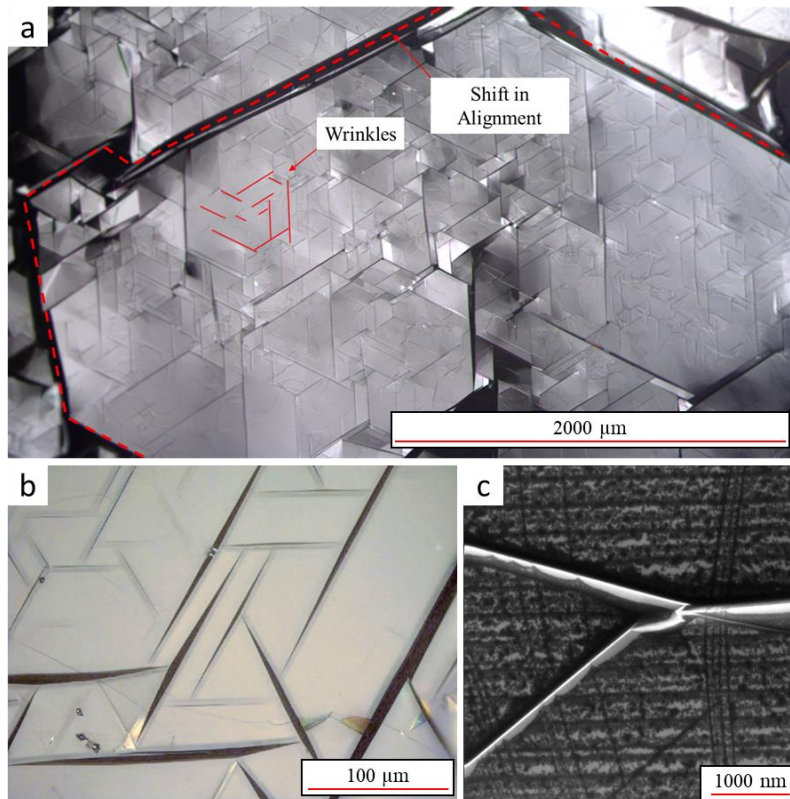


Figure 38 – Examples of wrinkles in hBN crystals. a) Optical micrograph of an hBN flake containing many wrinkles (scale bar is 2 mm). b) High magnification optical micrograph of an equilateral triangle formed by wrinkles (scale bar is 100 μm). c) SEM image of an intersection of 3 wrinkles (scale bar is 1 μm).

Cross-sectional samples were cut from wrinkles using Focused Ion Beam (FIB) and studied with Transmission Electron Microscopy (TEM) as shown in Figure 39. Each sample consisted of a few distinct crystal domains surrounding voids. Figure 39b is the diffraction pattern from the sample in Figure 39a, which shows just three lattice orientations highlighted by red, green, and blue lines in both figures. This indicates that the lattice structure of the wrinkle is highly ordered rather than consisting of randomly oriented hBN fused into a continuous structure. Figure 39c is a high-magnification TEM image of the boundary between two domains from Figure 39d that reveals the lattice structure at the boundary.

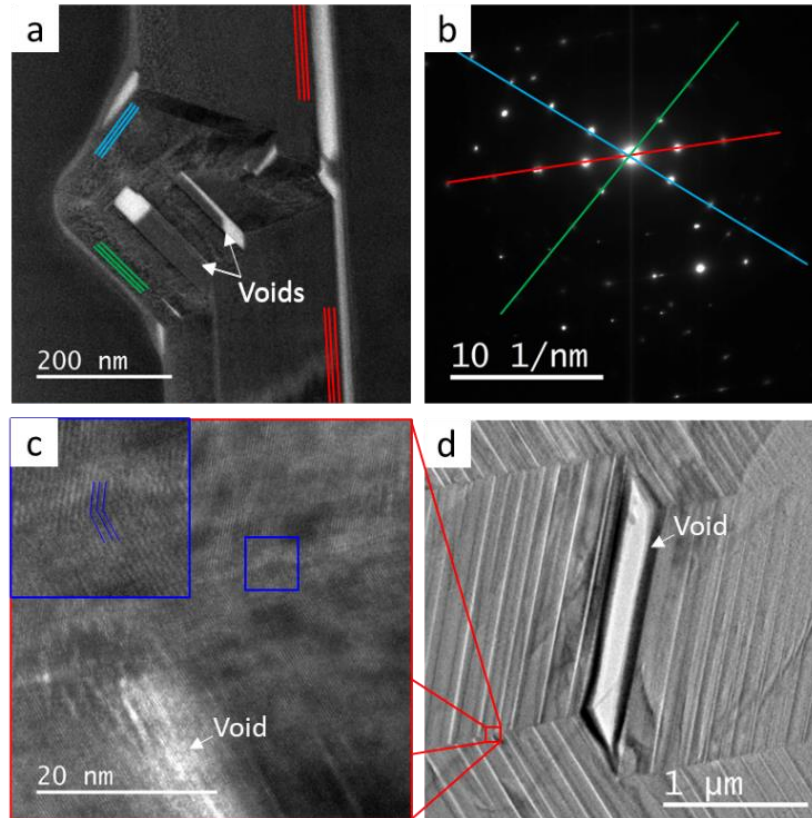


Figure 39 – TEM images of cross-sectional samples cut from wrinkles using FIB a) TEM image of a cross-sectional sample of a wrinkle with crystallographic directions highlighted. b) Diffraction pattern of sample shown in a that indicates three highly-crystalline regions are present. Red, blue, and green lines highlight the three lattice orientations present in the sample. c) TEM image of the boundary between two of the crystal domains shown in d, with inset highlighting its lattice structure. d) STEM image of another cross-sectional sample cut from a wrinkle using FIB.

This TEM data informs two hypotheses about how the wrinkles formed. First, the crystals may have grown into that shape due to twinning mechanisms or by filling in gaps left by a fractured crystal. However, it would be unlikely that in this case the boundaries would grow into being almost perfect planar defects in near perfect crystallographic orientations. Furthermore, the presence of voids in every cross-sectional sample of wrinkles made so far suggests that this is not the case since a growing crystal will tend to fill any gaps it can expand into. Second, the crystals may have started as a single domain, but due to forces external to the crystal, they were pushed into wrinkles akin to how colliding tectonic plates form mountains. This is supported by the high degree of order throughout the wrinkle, the perfect alignment of domains separated by microns,

and the formation of voids. However, the source of the external force necessary to cause this remains unclear. Two neighboring crystals growing into each other could introduce lateral stress into the crystals, but so could the thermal expansion mismatch between hBN and the cooling flux. If the former is true, wrinkles could be eliminated by ensuring only a single crystal nucleates, which is difficult to achieve in practice. If the latter is true, the wrinkles could be eliminated by separating the hBN from the flux before it cools substantially. Regardless, eliminating these wrinkles would dramatically increase the domain size from $\sim 100 \mu\text{m}$ to several millimeters, enabling larger devices to be produced.

CL spectroscopy on the wrinkles provides information on how it affects hBN's optical properties, but the emission from wrinkles is always convoluted with emission from the base material. Non-Negative Matrix Factorization and independent component analysis (discussed in Section 4.2.1) were used to isolate components of the hyperspectral CL maps. Figure 40 shows the output of this process performed on a wrinkle. The top figure is the average CL spectrum and map before data analysis was performed. In the middle figure, the emission unique to the wrinkle has been isolated from the emission from the base material, which is shown in the bottom figure. Notably, the spectral pattern shown in the top image looks very similar to the CL spectrum of twisted hBN layers produced in other work [11], suggesting that a similar defect has happened naturally here. In this case, the hBN layers likely became misaligned and the (0001) hBN planes were twisted relative to each other at the boundaries during the deformation that caused the wrinkle.

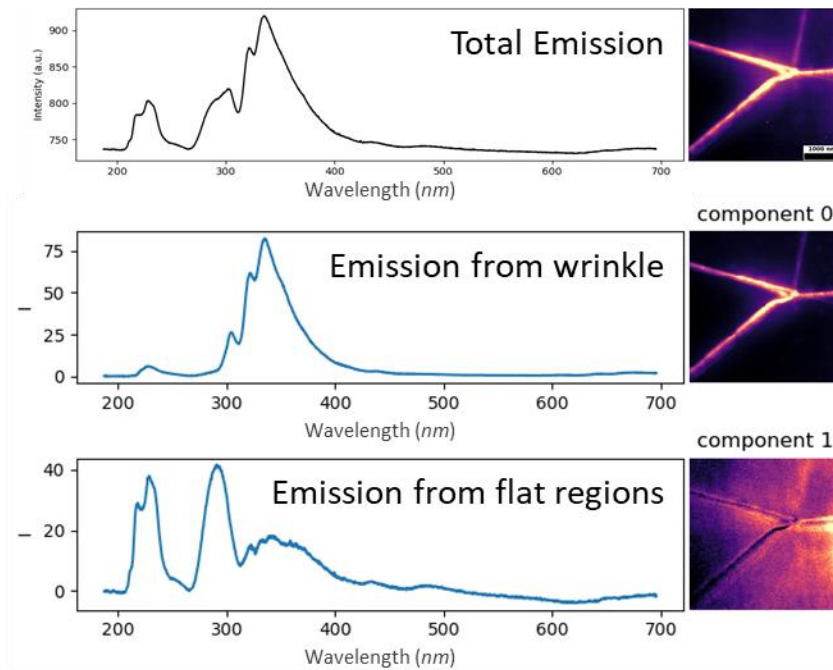


Figure 40 – Result of a combination of Non-Negative Matrix Factorization and Independent Component Analysis on an intersection of three wrinkles. Top) – Average CL spectrum and map prior to analysis. Middle) – Component showing emission unique to wrinkles isolated from data. Bottom) – Component showing emission representative of the base material. The sum of the two components recreates the average spectra in the top figure.

4.2.4 Invisible Lines

Invisible lines appear with a variety of features as shown in Figure 41, but are always associated with a reduction of band edge emission (200-220 nm) along thin lines as shown in the first column of bandpass images. These lines are invisible in optical micrographs and rarely correlate with features visible in SEM images, hence their name. They sometimes emit in the near band edge (220-265 nm) region as shown in the third sample or at long wavelengths (440-620 nm) as shown in the first and third samples. They also typically form two types of networks: either roughly parallel to one another as shown in the first sample or in a disordered network as shown in the second and third samples. In the cases where the invisible lines do not emit in these wavelength ranges, it is not clear whether the defects are physically different, or they do emit at these wavelengths but their emission is washed out by emission from other defects. If the latter is

true, their emission could potentially be extracted using the machine learning techniques showcased in Section 4.2.1 and Figure 36, which is reserved for future work. To determine if the former is true, the lattice structure of various examples of invisible lines must be determined through techniques such as TEM.

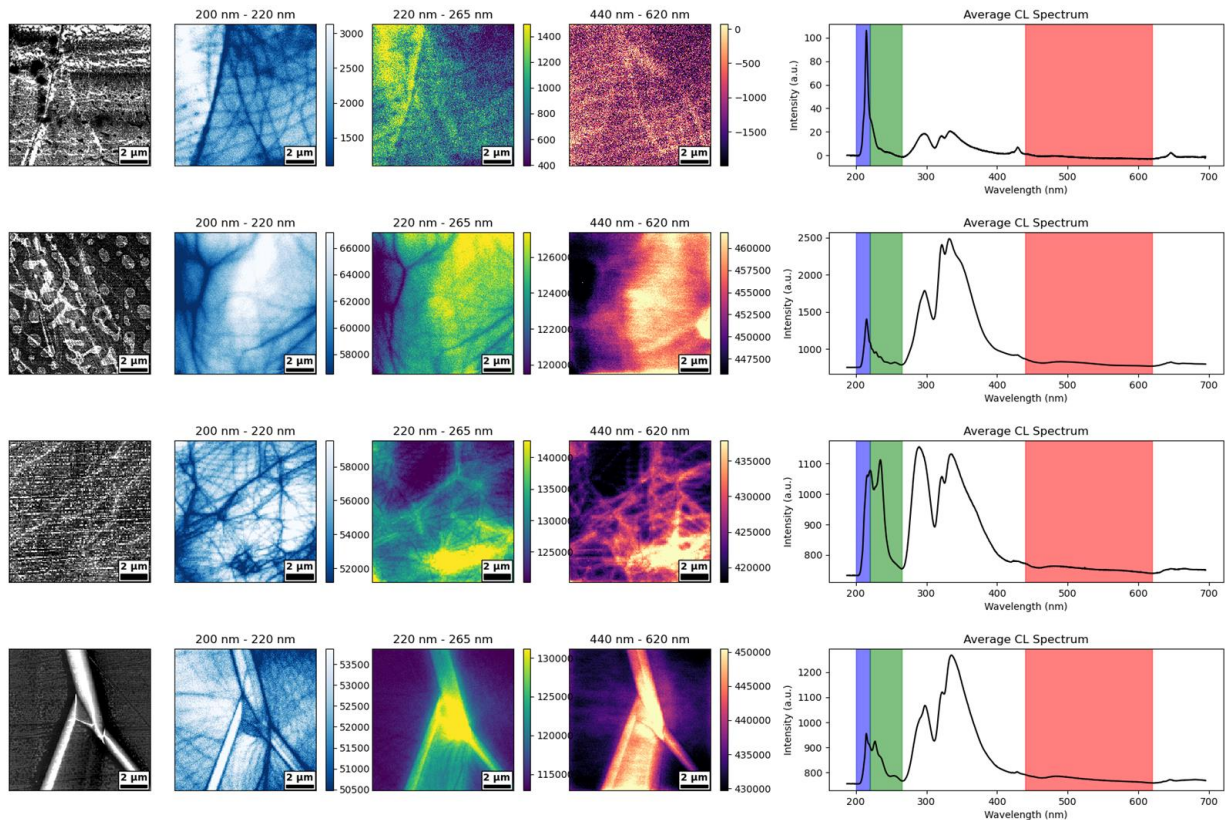


Figure 41 – Examples of CL maps that showed “invisible lines”. Each row is data from a selected sample and the first image in each row is an SEM image of the region mapped. The middle three columns are bandpass images created by summing the CL emission within a range of wavelengths. The right column is the average CL spectrum from each map with the bands used to create each bandpass image highlighted.

To gather structural information about these defects, hBN samples <100nm thick were exfoliated and deposited on perforated SIN membranes for TEM analysis as shown in Figure 42a. CL maps of this sample showed that invisible lines were present (Figure 42c), while TEM images revealed lines of local strain visible as wavy bright lines with dark shadows on both sides in Figure 42d. Edge dislocations, which take the form of half-inserted sheets inserted between

the 0001 planes in hBN as illustrated in Figure 42e, would cause both local strain and defect emission along the lines of their boundaries, indicating that this is what the invisible lines are. More detailed TEM work is needed to classify the different variations of invisible lines, but the perfectly hexagonal diffraction pattern of the area (inset of Figure 42d) indicates that these half planes don't disturb its crystallinity and aren't rotated with respect to the hBN lattice.

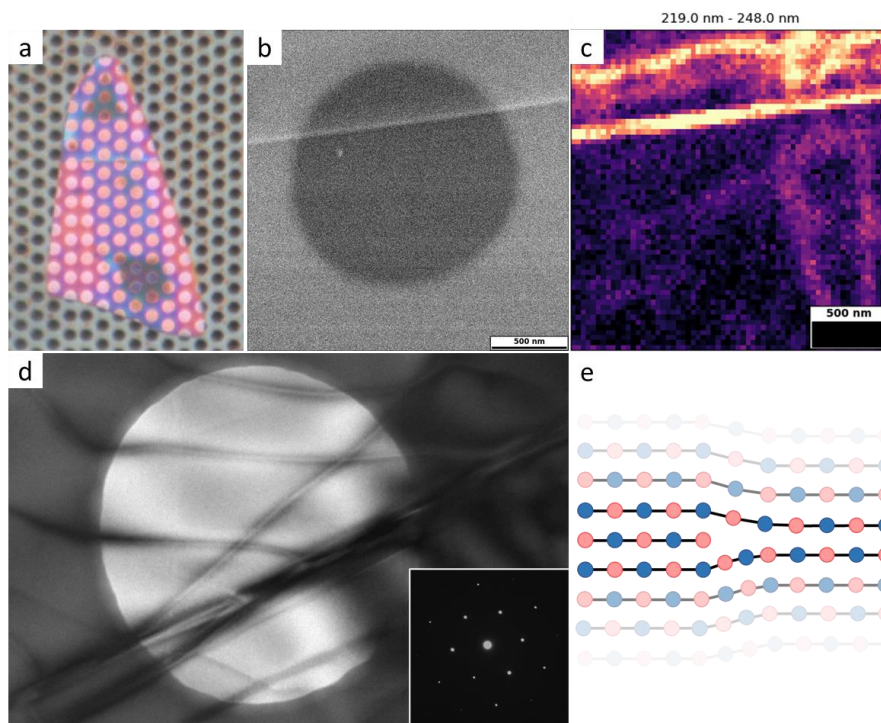


Figure 42 - Optical image of hBN crystal on a perforated SiN membrane (a), SEM image (b), and CL bandpass image (c) of one region on this crystal showing a small wrinkle and invisible lines emitting in the range 219-248 nm. d) In-plane TEM image and diffraction pattern (inset) of another region showing local strain along thin lines. e) Diagram of an inserted plane in hBN.

4.3 Correlating Crystal Quality to Solvent Species

Crystal quality is a broad term that encompasses dislocations, stacking faults, point defects, and impurities, each of which affect the crystal's properties in different ways, so quantifying "quality" is not straightforward. Still, several methods exist for comparing crystal quality between samples. The peak width of the Raman E_{2g} peak is the most commonly used quality metric for hBN, where any distortion of the lattice will cause the peak to broaden. This

gives a simple way to judge how defective the material is in general but does not give insight into what defects are present. Photoluminescence (PL) spectroscopy is another common tool for judging hBN crystal quality where the intensity of defect peaks can be used to judge the abundance of the defects associated with those peaks. Cathodoluminescence (CL) can be used in the same way as PL but can also be simultaneously used to identify specific defects as discussed in section 4.2. This section presents how each of these three techniques is used to determine how hBN crystal quality is affected by the solvent used to grow them.

4.3.1 Raman Spectroscopy

Raman spectroscopy is a common method for analyzing the crystal quality of hBN. Typically, the full width at half maximum (FWHM) of the E_{2g} peak located at $\sim 1366 \text{ cm}^{-1}$ is used to quantify crystal quality relative to other samples, and a peak width $< 8 \text{ cm}^{-1}$ is considered high quality by current standards. This is determined by fitting a Lorentzian peak to the Raman data as shown in Figure 43a, using the equation below:

$$Intensity = \frac{I}{1 + 4 \left(\frac{x - x_0}{FWHM} \right)^2}$$

Where I is the peak height, x_0 is the peak position, and $FWHM$ is the full width at half maximum. This was done for a set of 50 samples precipitated from a Fe, Fe-V, Ni-Cr, or Co-Cr solvent using a Raman microscope with a 532 nm laser. Figure 43b shows box plots of these measurements for each of the four solvents. Nearly all the samples measured had an E_{2g} FWHM less than 8 cm^{-1} indicating that high-quality hBN can be grown from any of these solvents.

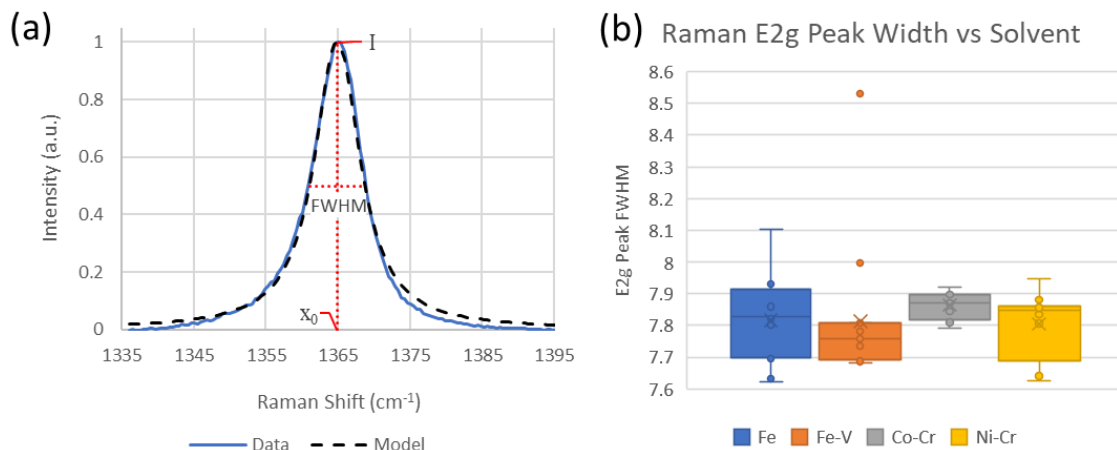


Figure 43 – a) Example of a Raman E_{2g} peak from an hBN sample generated in this work and b) boxplots of the range of Raman E_{2g} peak widths of samples grown from four different solvents.

4.3.2 Photoluminescence Spectroscopy

Photoluminescence spectroscopy provides another way to quantify defects in hBN crystals. As discussed in Section 4.2.1, emission from different regions of an hBN PL spectrum can be correlated to two broad categories of defects: stacking faults (5-5.7 eV) and point defects (<5 eV). The intensity of emission in these regions will correlate to the relative quantity of their corresponding defects, but to compare intensities between samples, the data must be normalized. The absolute intensity of PL spectra can depend on the focus and alignment of optical components, the temperature of the sample, and the thickness of the sample, all of which can vary from measurement to measurement. To normalize the intensities, an intrinsic feature is usually chosen as the normalization factor. Since intrinsic emission will be consistent regardless of experimental and sample variability (e.g. optical alignment or thickness), defect emission from separate samples can be compared by using the ratio of its intensity to this feature. In this work, the intensity of the TO phonon replica peak was the normalization parameter since it is the most intense phonon replica.

Figure 44a) shows an example of a PL spectrum of an hBN sample acquired with 196 nm excitation at 9K and normalized to its TO phonon peak. The normalized intensity at 5.47 eV was used as the metric to represent the relative quantity of stacking faults and the normalized intensity at 4.16 eV was used as the metric to represent the relative quantity of point defects. This was done for five samples from each solvent (Fe, Fe-V, Co-Cr, and Ni-Cr) as shown in Figure 44 b and c. In both regions, samples grown from Ni-Cr and Co-Cr had lower normalized defect peak intensities on average (shown by dashed lines), indicating that they typically produce higher quality crystals, than those grown from Fe or Fe-V.

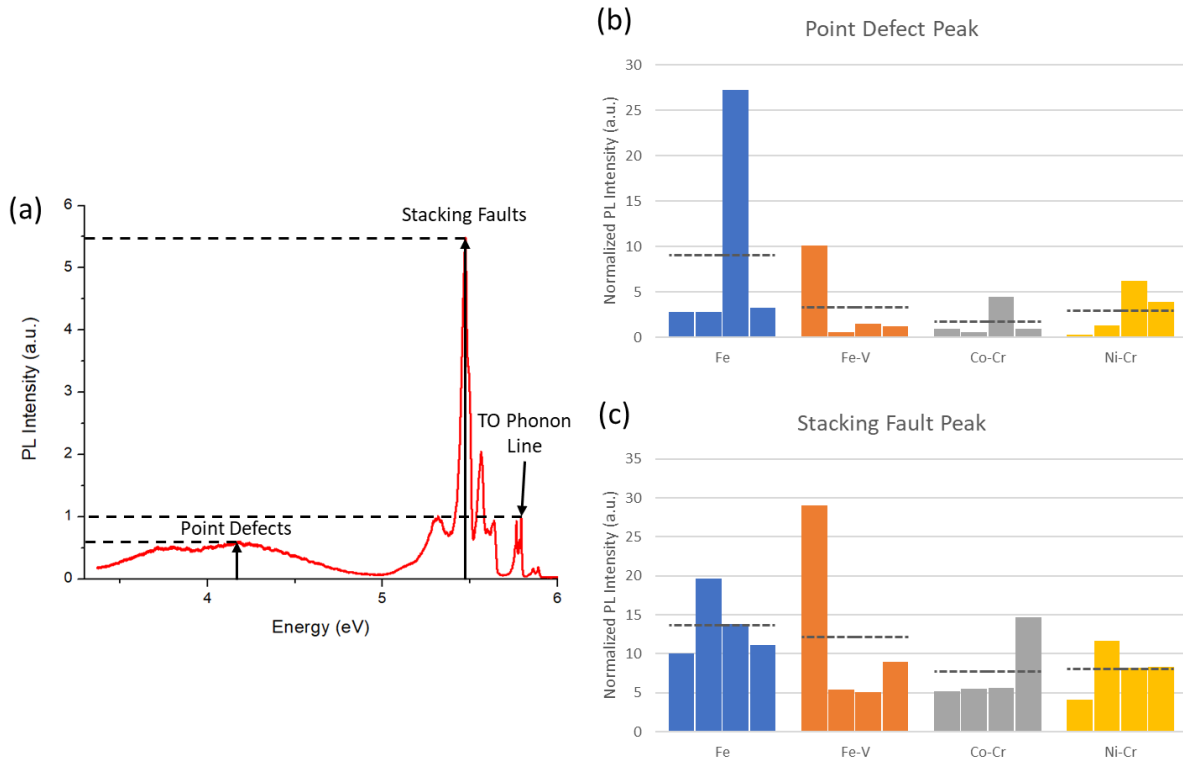


Figure 44 – a) Example of a hBN PL spectrum normalized by its TO Phonon Line. The normalized intensity at 5.47 eV correlates to the relative abundance of stacking faults and the normalized intensity at 4.16 eV correlates to the relative abundance of point defects. These intensities from several samples grown from each solvent (Fe, Fe-V, Co-Cr, and Ni-Cr) are shown for point defects (b) and stacking faults (c). Dashed lines are the average intensities from each solvent.

4.3.3 Cathodoluminescence Spectroscopy

As discussed in Section 4.2, CL provides a way to identify differences in optical defect emission between samples and link emissions to particular defects. However, to compare defects between samples, the data must be normalized. The absolute intensity of a CL spectrum depends on a wide variety of factors stemming from experimental conditions such as acquisition parameters, alignment of the light collection mirror, and variation in the electron beam intensity or from physical characteristics of the sample such as its thickness or interaction with its substrate. All these factors can change from measurement to measurement and cannot be easily accounted for.

As with the PL data analyzed in this work, the CL data was normalized to the optical phonon replica. However, in CL spectroscopy, the phonon replica peaks are convoluted with defect peaks (Figure 34), making normalization this way more difficult. However, the intensity at wavelengths below 215 nm is almost entirely from the phonon replicas (Figure 45a). Thus, the intensity of the phonon replica peaks can be extracted by fitting two gaussian peaks to this region of the spectrum. The code written to accomplish this is given in Appendix B.2.

To compare differences in defects between samples grown from each of the 5 solvents tested, the normalized emission was integrated over two wavelength ranges. Figure 45c shows boxplots of the integrated intensity between 200 nm and 265 nm, which encompasses the intrinsic emission and peaks associated with stacking faults. Figure 45d shows boxplots of the integrated intensity between 265 nm and 650 nm, which encompasses peaks associated with point defects and color centers. In both ranges, the defect emission of hBN grown from Ni-Cr, Co-Cr, and Fe-V were roughly equal, indicating that they have similar defect densities. In contrast, hBN grown from Fe and Cu generally had higher defect emission than the others,

indicating that they tend to have higher defect densities. Thus, to form the highest quality hBN, any of the Ni-Cr, Co-Cr, or Fe-V solvents should be used. Moreover, it tells us that the individual domains as exfoliated flakes display near-perfect hBN properties with minimal contribution from edge dislocations and point defects.

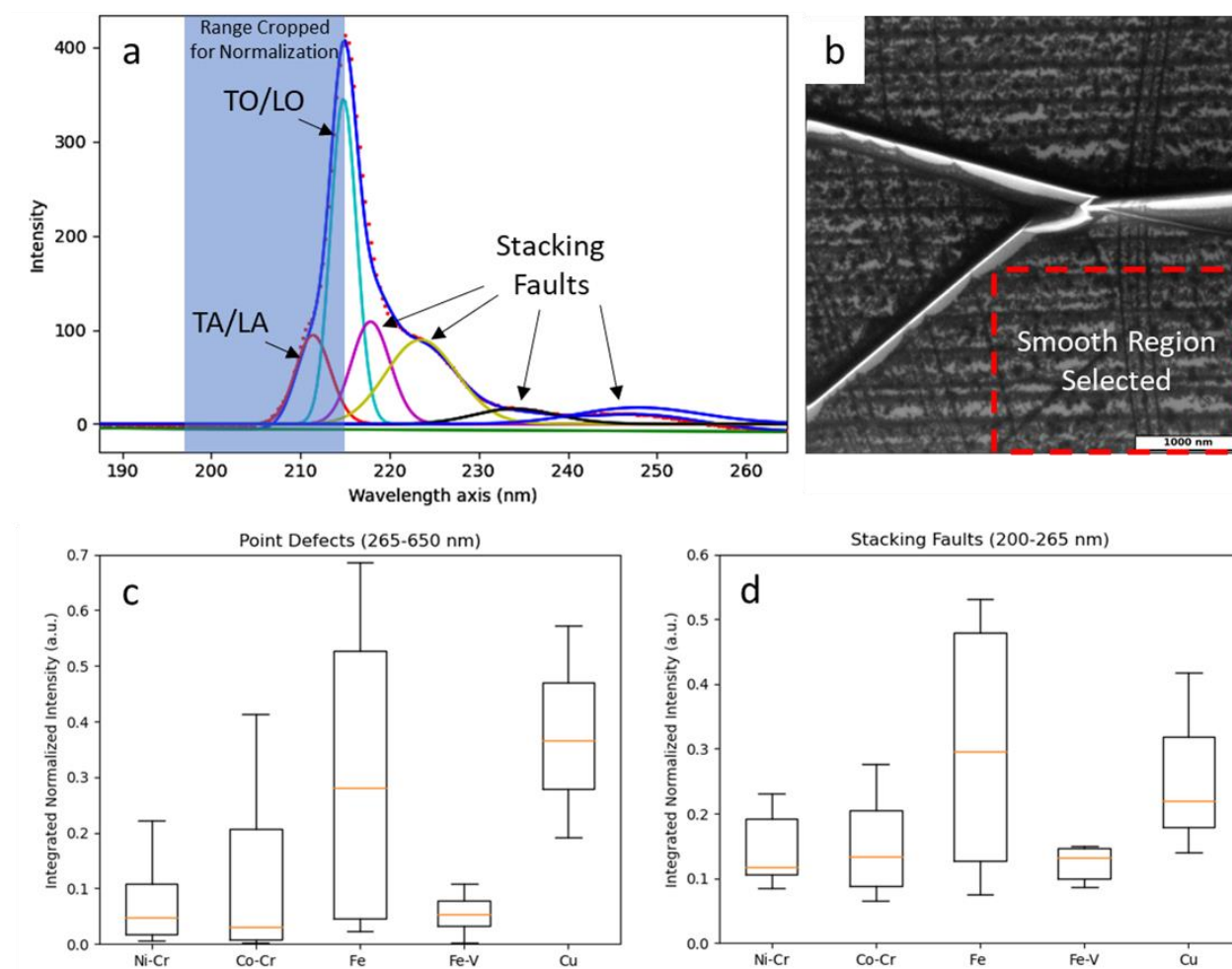


Figure 45 - a) CL spectrum fit with 6 gaussian peaks - two for optical and acoustic phonon replicas and 4 for defect emission. b) Example of a region manually selected for comparisons. Obvious defects like wrinkles, cracks, and folds were avoided to be more representative of the material in general. c) Box plots showing the range of the integrated intensity within the range 265-650 nm (representing point defects) for hBN samples grown from each solvent. d) Box plots showing the range of the integrated intensity within the range 200-265 nm (representing stacking faults) for hBN samples grown from each solvent.

4.4 References

- [1] N. Mendelson et al., “Identifying carbon as the source of visible single-photon emission from hexagonal boron nitride,” *Nat. Mater.*, vol. 20, no. 3, pp. 321–328, Mar. 2021.
- [2] M. R. Uddin, J. Li, J. Y. Lin, and H. X. Jiang, “Probing carbon impurities in hexagonal boron nitride epilayers,” *Appl. Phys. Lett.*, vol. 110, no. 18, p. 182107, May 2017.
- [3] M. Onodera et al., “Carbon-Rich Domain in Hexagonal Boron Nitride: Carrier Mobility Degradation and Anomalous Bending of the Landau Fan Diagram in Adjacent Graphene,” *Nano Lett.*, vol. 19, pp. 7782–7286, 2019.
- [4] S. J. Grenadier, A. Maity, J. Li, J. Y. Lin, and H. X. Jiang, “Origin and roles of oxygen impurities in hexagonal boron nitride epilayers,” *Appl. Phys. Lett.*, vol. 112, 2018.
- [5] S. Li and A. Gali, “Identification of an oxygen defect in hexagonal boron nitride,” *J. Phys. Chem. Lett.*, vol. 13, no. 41, pp. 9544–9551, Oct. 2022.
- [6] R. Speiser, S. Naiditch, and H. L. Johnston, “The vapor pressure of inorganic substances. II. B₂O₃,” *J. Am. Chem. Soc.*, vol. 72, no. 6, pp. 2578–2580, Jun. 1950.
- [7] F. T. Greene and J. L. Margrave, “The vapor pressure of boron oxide over the range 1946–2419°K,” *J. Phys. Chem.*, vol. 70, no. 7, pp. 2112–2115, Jul. 1966.
- [8] S.-Y. Zhang, K. Xu, X.-K. Zhao, Z.-Y. Shao, and N. Wan, “Improved hBN single-crystal growth by adding carbon in the metal flux,” *Cryst. Growth Des.*, vol. 19, no. 11, pp. 6252–6257, Nov. 2019.
- [9] T. Q. P. Vuong et al., “Overtones of interlayer shear modes in the phonon-assisted emission spectrum of hexagonal boron nitride,” *Phys. Rev. B Condens. Matter*, vol. 95, no. 4, p. 045207, Jan. 2017.
- [10] N. P. de Leon et al., “Materials challenges and opportunities for quantum computing hardware,” *Science*, vol. 372, no. 6539, Apr. 2021.
- [11] C. Su et al., “Tuning colour centres at a twisted hexagonal boron nitride interface,” *Nat. Mater.*, vol. 21, no. 8, pp. 896–902, Aug. 2022.
- [12] B. Shevitski et al., “Blue-light-emitting color centers in high-quality hexagonal boron nitride,” *Phys. Rev. B.*, vol. 100, no. 15, Oct. 2019.

Chapter 5 - Isotopic Control in hBN Synthesis

Chapter 5 is reproduced in part with permission from:

E. Janzen, H. Schutte, J. Plo, A. Rousseau, T. Michel, W. Desrat, P. Valvin, V. Jacques, G. Cassabois, B. Gil, and J.H. Edgar, “Boron and nitrogen isotope effects on hexagonal boron nitride properties,” arXiv:2306.13358 [cond-mat.mtrl-sci], Jun. 2023.

5.1 Introduction

Hexagonal boron nitride (hBN) is the second most important two-dimensional material after graphite and its monolayer derivative, graphene. Although hBN and graphite have similar crystal structures and lattice parameters, their properties are quite different. Graphite is electrically conductive; hBN is an electrical insulator. Graphite is opaque; hBN is optically transparent from deep ultraviolet through the infrared. Graphite reacts with oxygen and air at low ($\sim 400^\circ\text{C}$) temperatures, while hBN is chemically inert. Thus, in many ways, the properties of hBN and graphite are complimentary.

The properties of crystalline hBN are advantageous for a wide range of nanophotonic [1], electronic [2,3], and quantum [4,5] devices. Because its optical properties are hyperbolic, it can compress infrared light to extremely small volumes, through the use of hyperbolic phonon polaritons. This is useful in nanophotonics as it increases light-matter interactions, and thereby chemical and biological sensing [6]. It also enables much higher image resolutions, hyperlensing [7], than is possible using the source free-space light. hBN analogue switches with high power handling and switching speeds have shown promise for high frequency devices [8], while hBN-based memristors integrated into CMOS devices for computation had superior endurance

compared to more mature technologies [9]. hBN is appealing for quantum devices due its ability to host bright, stable, single photon emitters, some of which are magnetically addressable [10,11]. Boron nitride is also an excellent platform for near zero index photonics in the infrared [12]. Near-zero-index materials exhibit unique features in the area of light–matter interaction: when the values of the relative permittivity reach zero, at the operating frequency, the wavelength in these media is “stretched,” and the phase of the signal is approximately uniform across this structure, which shapes the time oscillating waves to a static-like spatial distribution. An eclectic series of interesting and exciting phenomena can thus be initiated, including the levitation of electrically polarized nanoparticles in the vicinity of such material [13].

We have previously demonstrated that the properties of hBN can be varied by controlling its concentrations of boron isotopes. There are two stable boron isotopes, which are naturally distributed as approximately 20% ^{10}B and 80% ^{11}B . These isotopes have distinctly different properties. Their nuclear spins are 3/2 and 3 for ^{10}B and ^{11}B respectively. ^{10}B has one of the largest neutron capture cross section of any isotope of any element, approximately 3855 barns for neutrons with velocities of 2200 m/s [14]. For the majority of element isotopes, the neutron capture cross section is on the order of one or less.

The hBN crystalline flakes enriched to nearly 100% ^{10}B and 100% ^{11}B (described as monoisotopic), as well as in variable proportions, were grown by precipitating from molten metal solutions at atmospheric pressure [15-19]. Typically, the solvents were nickel plus chromium [15], but hBN crystals were also grown using an iron plus chromium solvent [16]. The source materials necessary to synthesize this hBN were isotopically-enriched boron powder and ultra-high purity nitrogen gas with its natural isotope distribution (99.6% ^{14}N , 0.4% ^{15}N). The nitrogen was supplied by continuously flowing nitrogen gas over the solution during the

entire process. A small concentration of hydrogen was added to the gas flow during crystal growth, to reduce and remove any oxides present. The molten solution was created by heating the components (contained in an alumina crucible) to 1550 °C, then slowly cool at 1 to 4 °C/h to precipitate the crystals.

The properties of boron isotope enriched hBN were characterized in several studies. Vuong *et al* [17] demonstrated that the energy band gap of hBN was slightly reduced or increased when enriched in ^{10}B or ^{11}B , respectively. The E_{2g}^{high} peak position in the Raman spectra shifted up from 1,366 cm^{-1} for hBN with the natural distribution of boron isotopes to 1,393 cm^{-1} for $h^{10}\text{BN}$ and down to 1,357 cm^{-1} for $h^{11}\text{BN}$, [17-19]. The FWHM of the E_{2g}^{high} peak at room temperature of the boron monoisotopic hBN was also reduced to 3.0 cm^{-1} from 7.5 cm^{-1} for natural hBN, due to less isotopic disorder [19]. The maximum peak width was predicted to occur with isotope concentrations of 65% ^{11}B and 35% ^{10}B [19]. The phonon lifetime for monoisotopic hBN is increased by a factor of 2.7 from $h^{\text{nat}}\text{BN}$ [20]. Using scattering type near field optical microscopy (S-NOM) Giles *et al* [18] first showed the phonon-polariton propagation length is significantly increased in monoisotopic hBN. Pavlidis *et al* [21] measured the maximum hyperbolic phonon polariton lifetimes as 4.2 ps with propagation lengths of 25 μm , and an eight-fold increased figure of phonon propagating merit in comparison to $h^{\text{nat}}\text{BN}$.

The longer phonon lifetimes achieved by eliminating isotopic disorder increases the thermal conductivity of hBN. Lindsay and Broido [22], first predicted the thermal conductivity of hBN increase by eliminating isotopic disorder, ie for hBN with a single boron isotope. They also predicted the thermal conductivity of atomically thin layers of hBN would be much higher than bulk hBN [22]. Yuan *et al* [23] measured a maximum in-plane room temperature thermal conductivity of 585 $\text{W}/(\text{m}\cdot\text{K})$ for bulk $h^{10}\text{BN}$ and 550 $\text{W}/(\text{m}\cdot\text{K})$ for $h^{11}\text{BN}$, compared to 408

W/(m·K) for h^{nat}BN. Mercado *et al* [24] reported a similar value of 630 W/(m·K) for h¹⁰BN five layers thick. Subsequently, on a h¹¹BN monolayer, Cai *et al* [25,26] measured an in-plane thermal conductivity of 1009 W/(m·K), compared to 751 W/(m·K) for h^{nat}BN, as well as noting differences in the coefficients of thermal expansion with boron isotope. Hot carriers cool faster when generated in graphene in contact with higher thermal conductivity monoisotopic hBN than hBN with the natural distribution of boron isotopes [27].

Monoisotopic hBN has also proven advantageous in several applications. The longer hyperbolic phonon polariton propagation distance in isotopically enriched h¹⁰BN enabled Li *et al* [28] to produce an anomalous, concave wave front on a h¹⁰BN metasurface. Demonstrating hyperlensing, objects as small as 44 nm separated by distances of 25 nm were resolved via N-SOM using light with a free-space wavelength of 6.76 μm and h¹¹BN [7]. Vibrational strong coupling between phonon polaritons in hBN and organic molecules was reported by Bylinkin *et al* [29]. This has the potential to reduce the size and enhance the sensitivity of on-chip spectroscopes. Folland *et al* [30] changed the optical properties of h¹¹BN by placing it in contact with VO₂ which was changed from a dielectric to a metal by changing its temperature. Finally, isotopic purification with ¹⁰B leads to an improvement of the spin coherence properties of optically-active point defects in hBN, which are currently attracting a deep scientific interest for applications in quantum sensing and metrology [31].

In the present study, we demonstrate further control over the properties of hBN by changing the concentration of the nitrogen isotope in crystalline hBN. Natural nitrogen is predominantly ¹⁴N (99.6%) with a small amount of ¹⁵N (0.4%). Changing the nitrogen isotopes as well as the boron isotopes offers the possibility of shifting its Reststrahlen band for better matching to the infrared absorption of specific organic molecules, to achieve greater sensitivity

[32]. ^{14}N and ^{15}N have different nuclear spins, 1 and $\frac{1}{2}$ respectively, which may prove important in quantum applications. Unlike ^{14}N , ^{15}N reacts with high energy protons to form carbon and an alpha particle [33].

There have only been a few prior publications on the effects of ^{15}N in boron nitride [32,34,35]. He *et al* [32] examined the impacts of changes with both boron and nitrogen isotopes on dielectric properties of cubic boron nitride. Jesche *et al* [34] studied the nuclear magnetic resonance spectra combination of all stable boron and nitrogen isotopes in both cubic boron nitride (cBN) and hBN containing the natural distributions of isotopes (i.e. no isotope enrichment). The present study is distinguished from these prior studies by focusing on high quality hBN crystals enriched with the nitrogen-15 isotope.

5.2 Synthesis

Previous work on atmospheric pressure solution growth of hBN with monoisotopic boron (^{10}B or ^{11}B) and natural abundance nitrogen (99.6% ^{14}N) used a continuous stream of nitrogen gas that both provides nitrogen for the formation of hBN and sweeps volatile impurities out of the system. However, the high cost of monoisotopic ^{15}N gas would make continuous $^{15}\text{N}_2$ gas flow financially unsustainable. Therefore, for the synthesis of hBN with monoisotopic ^{15}N , a new two-step process was developed to make more efficient use of nitrogen.

The first step, termed ingot formation, was done to purify the source materials and thoroughly mix them into an isotropic solution without any nitrogen. Isotopically pure (>99%) ^{10}B or ^{11}B powder was mixed with Ni and Cr powder in an alumina crucible in the mass ratio 12/12/1 Ni/Cr/B, respectively. This was then placed in a horizontal tube furnace, evacuated of air, and purged with a mixture of 93/7 argon/hydrogen flowing continuously at 270 sccm and 850

torr. The furnace was heated to 1550°C, held there for 24 hours, and cooled back down as illustrated by the dashed line in Figure 46.

Separating this step from crystal growth has a couple notable benefits. First, it enables a precise and reproducible concentration of components to be used by ensuring all the source materials melt together into a cohesive flux. If nitrogen is used in this step, undissolved powder usually remains separated from the solidified flux, which changes the concentration of the flux by an unknown amount. Furthermore, if nitrogen were used in this step, it would need to be isotopically pure $^{15}\text{N}_2$ gas to avoid producing hBN that has a mixture of ^{14}N and ^{15}N . Second, hydrogen diluted with argon for safety is included to react with residual oxygen in the gas phase and to reduce oxides in the source materials to produce water vapor. Since no expensive $^{15}\text{N}_2$ gas is used in this step, the gas flow can be continuous, sweeping the oxygen impurities from the system, thus purifying the flux for crystal growth.

In the crystal growth step, the ingot is heated and slowly cooled in the presence of $^{15}\text{N}_2$ gas to precipitate hBN enriched with ^{15}N . The ingot produced in the first step is placed in the same horizontal tube furnace purged of air using argon, then backfilled with a mixture isotopically pure $^{15}\text{N}_2$ gas and hydrogen. To limit the use of ^{15}N , the tube was sealed off once the pressure rose to atmospheric pressure and hydrogen was included to react with any residual oxygen. Then the furnace was heated to 1550°C, held there for 24 hours, and slowly cooled at 1°C/hr to 1500°C to precipitate hBN single crystals as illustrated by the solid line in Figure 46. Once the system has cooled, the alumina boat contains a solidified metal ingot with a layer of hBN crystals covering its top surface, as shown in Figure 47. Mechanical exfoliation of the hBN from the ingot produces free-standing hBN flakes like the one shown in Figure 48, which were used in Raman and photoluminescence measurements.

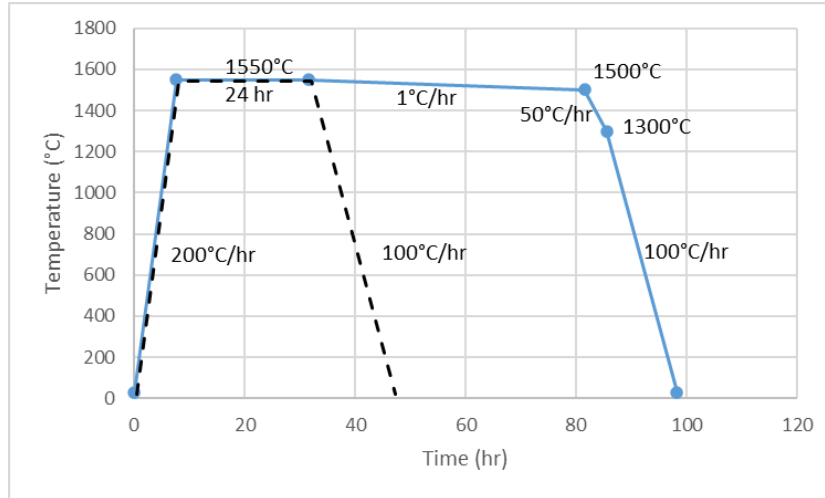


Figure 46 – Temperature profile of two-part process used to produce isotopically-controlled hBN crystals. In the first part (dashed line), the system is heated and dwelled at 1550°C under an Ar/H₂ atmosphere to form a homogenous ingot. In the second part (solid line), the system is heated to 1550°C and slowly cooled under a ¹⁵N₂/H₂ atmosphere to precipitate hB¹⁵N crystals.

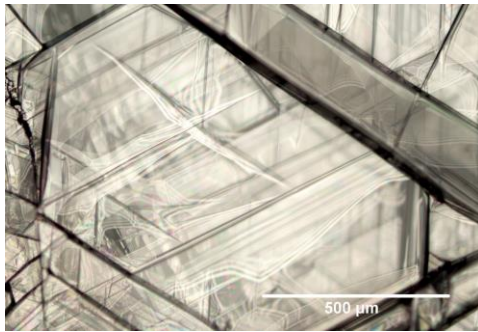


Figure 47 – Micrograph of a h¹⁰B¹⁵N single crystal mechanically exfoliated from a solidified ingot.

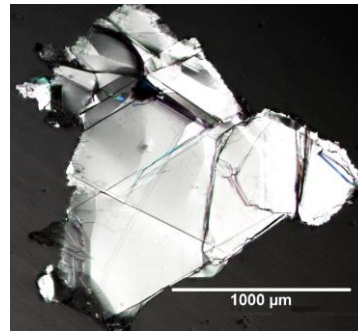


Figure 48 – Image of the surface of the Ni-Cr-B ingot after an experiment with hB¹⁵N single crystals on its surface.

Since isotopically pure boron (¹⁰B or ¹¹B) and isotopically pure ¹⁵N are the only boron and nitrogen sources present in the system during the process, any hBN that forms will have these isotopes. Thus, hBN can now be produced with any combination of boron and nitrogen isotopes: h¹⁰B¹⁴N, h¹¹B¹⁴N, h¹⁰B¹⁵N, or h¹¹B¹⁵N. This process also has the flexibility to produce hBN with precise mixtures of isotopes by controlling how much ¹⁰B and ¹¹B powder is added in

the first step and the ratio of $^{14}\text{N}_2$ and $^{15}\text{N}_2$ gas introduced to the system, though that was not attempted in this study.

5.3 Results

Raman spectroscopy was carried out at room temperature. The Raman mode at $\sim 1360\text{ cm}^{-1}$ was measured with a Renishaw Invia spectrometer (2400 lines/mm) and the mode at $\sim 50\text{ cm}^{-1}$ was measured using a Horiba T64000 (1800 lines/mm) in the subtractive mode for which we used the oversampling method implemented in Ref.[17]. For the low- (resp. high-) frequency measurement of the E_{2g} Raman phonon, a 660 (resp. 532) nm laser was focused under a 50x objective (N.A. 0.5) with the power at the sample kept below $300\text{ }\mu\text{W}$ to avoid heating effects. The high-energy Raman mode (E_{2g}^{high}) was studied in monoisotopic $\text{h}^{10}\text{B}^{14}\text{N}$, $\text{h}^{10}\text{B}^{14}\text{N}$, $\text{h}^{10}\text{B}^{15}\text{N}$, and $\text{h}^{11}\text{B}^{15}\text{N}$ crystals, together with a reference $\text{h}^{\text{nat}}\text{BN}$ crystal with natural abundance of the boron and nitrogen isotopes (Figure 49). Compared to previous Raman results [17], in the data set of Figure 49, the new $\text{h}^{10}\text{B}^{15}\text{N}$ and $\text{h}^{11}\text{B}^{15}\text{N}$ configurations incorporate Raman lines that are roughly the mirror images of $\text{h}^{10}\text{B}^{14}\text{N}$ and $\text{h}^{10}\text{B}^{14}\text{N}$ with respect to $\text{h}^{\text{nat}}\text{BN}$. This results in a progressive red-shift of the E_{2g}^{high} mode as a function of the reduced mass in the unit cell, from $\sim 1393\text{ cm}^{-1}$ in $\text{h}^{10}\text{B}^{14}\text{N}$ to $\sim 1335\text{ cm}^{-1}$ in $\text{h}^{11}\text{B}^{15}\text{N}$ (Figure 49b). The experimental blue-shifts (red-shifts) of $+27.8$ and $+9.7\text{ cm}^{-1}$ (-8.3 and -27.6 cm^{-1}) in $\text{h}^{10}\text{B}^{14}\text{N}$ and $\text{h}^{10}\text{B}^{14}\text{N}$ ($\text{h}^{10}\text{B}^{14}\text{N}$ and $\text{h}^{11}\text{B}^{15}\text{N}$) with respect to $\text{h}^{\text{nat}}\text{BN}$ are in excellent agreement with the $+30.9$ and $+11.1\text{ cm}^{-1}$ (-7.0 and -27.4 cm^{-1}) values computed by means of DFT calculations within the QuantumEspresso package, respectively. Remarkably, all monoisotopic crystals display narrow Raman lines with a width $\sim 4\text{ cm}^{-1}$, significantly smaller than the $\sim 8\text{ cm}^{-1}$ width in $\text{h}^{\text{nat}}\text{BN}$. This effect stems from the suppression of isotopic disorder in monoisotopic crystals [17], and direct evidence of the equally-high crystalline quality of the $\text{h}^{10}\text{B}^{14}\text{N}$, $\text{h}^{10}\text{B}^{14}\text{N}$, $\text{h}^{10}\text{B}^{15}\text{N}$, and $\text{h}^{11}\text{B}^{15}\text{N}$ crystals.

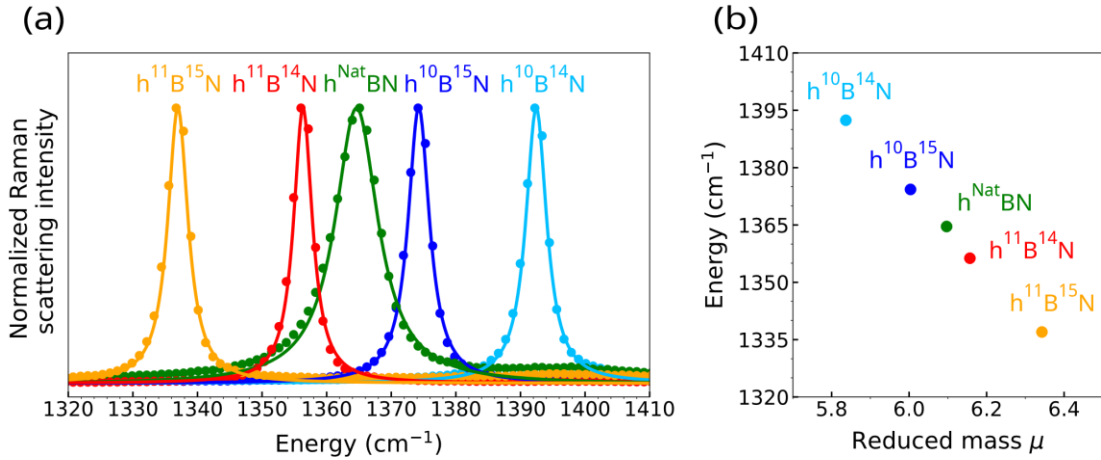


Figure 49 – High-energy Raman mode (E_{2g}^{high}) from hBN synthesized with different isotope combinations. a) Normalized peak for each isotope combination. b) Raman shift of each sample plotted versus its reduced mass.

For the low-energy Raman mode (E_{2g}^{low}), the behavior is different (Figure 50). This mode corresponds to the shear rigid motion between adjacent layers, with a frequency around 50 cm^{-1} (Figure 50a). In contrast to the smooth variations of the E_{2g}^{high} frequency as a function of the reduced mass and the related mirror symmetry of the Raman lines with respect to h^{nat}BN [Figure 49], the E_{2g}^{low} mode does not shift monotonously with the isotopic composition, as seen in Figure 50b. First, the E_{2g}^{low} frequency recorded in the reference h^{nat}BN crystal is no longer the average value of the ones in h¹⁰B¹⁴N and h¹¹B¹⁵N. Second, for h¹⁰B¹⁵N, a red-shift of the E_{2g}^{low} mode is recorded, instead of the blue-shift for the high-frequency Raman line (Figure 49), which is naturally explained by the variation of the reduced mass. Strikingly, the E_{2g}^{low} frequency turns out to be approximately the same for h¹⁰B¹⁵N and h¹⁰B¹⁴N. This complex phenomenon reveals the non-trivial variations of the interlayer shear mode frequency with the isotopic composition, and thus the subtle impact of the isotopic content on the weak van der Waals interaction between adjacent layers. Although the E_{2g}^{high} mode grossly varies linearly versus the reduced mass (Figure 49b), the E_{2g}^{low} one does not and Figure 50b indicates a parallelogram-like locus with

four corners defined by the energies of the $^{10}\text{B}^{14}\text{N}$, $^{10}\text{B}^{15}\text{N}$, $^{11}\text{B}^{15}\text{N}$ and $^{11}\text{B}^{14}\text{N}$ samples. This locus is the experimental evidence of the delicate dependences of the phonon modes with isotopic composition. Note for the sake of the completeness that the $^{\text{nat}}\text{BN}$ value sits on the line connecting $^{10}\text{B}^{14}\text{N}$ to $^{11}\text{B}^{14}\text{N}$. The deviation is linked to alloy disorder in the boron sublattice [36].

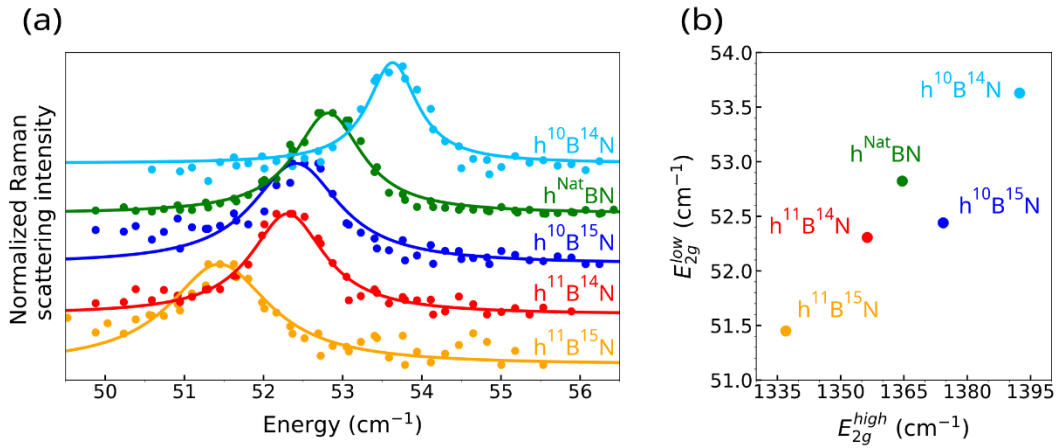


Figure 50 - Low-energy Raman mode (E_{2g}^{low}) from hBN synthesized with different isotope combinations. a) Normalized peak for each isotope combination. b) Evolution of the low energy Raman active mode versus the high energy one, which indicates the delicate dependences of the phonon modes with isotopic composition.

These results are quantitatively interpreted by our DFT calculations of the dispersion relations of the phonon modes in these samples that are offered in Figure 51. Four specific regions have been zoomed in four inserts dedicated to the E_{2g}^{low} and the E_{2g}^{high} normal vibration modes. The plots on the left-hand side correspond to the center of the Brillouin Zone while the plots on the right-hand side represent the dispersions relations of the (TA,LA) and (TO,LO) couples at the T point of the Brillouin Zone. The values of the energies of the latter are useful for an accurate determination of the values of the indirect excitons versus isotopic purification as we shall discuss it later in this manuscript. They also account for the asymmetric shifts of the E_{2g}^{low} mode in $h^{10}\text{B}^{14}\text{N}$ and $h^{11}\text{B}^{15}\text{N}$ with theoretical estimations of +0.9 and -1.3 cm⁻¹ with

respect to $h^{\text{nat}}\text{BN}$, in fair agreement with the experimental values of $+0.8$ and -1.4 cm^{-1} . Moreover, DFT calculations predict the same frequency within an accuracy of 0.1 cm^{-1} for the E_{2g}^{low} mode in $h^{10}\text{B}^{15}\text{N}$ and $h^{10}\text{B}^{14}\text{N}$, with a red-shift of -0.2 cm^{-1} with respect to $h^{\text{nat}}\text{BN}$, thus providing a consistent interpretation of our experimental data where the measured red-shift is $\sim -0.45 \text{ cm}^{-1}$.

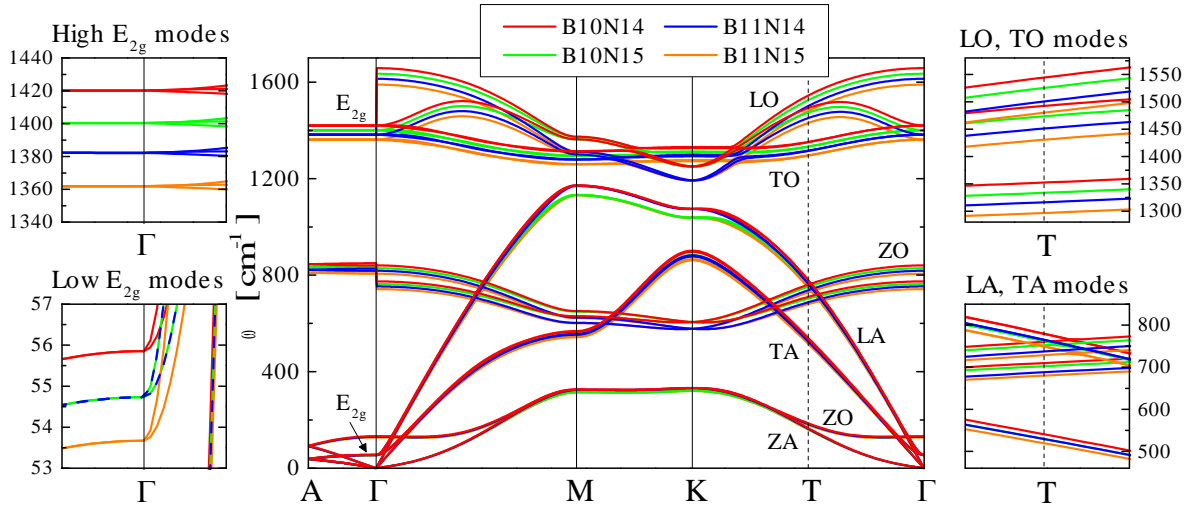


Figure 51 – Phonon dispersion relations in the four hBN isotopically purified samples. Left-hand side are zoomed the energy regions corresponding to the E_{2g}^{low} (bottom) and E_{2g}^{high} (top) phonons at Γ . Right-hand side are zoomed the energy regions corresponding to the (TA,LA) couple (bottom) and (TO,LO) couple (top) of phonon at the T point of the Brillouin Zone.

We performed photoluminescence (PL) spectroscopy in the deep-ultraviolet to further characterize the monoisotopic hBN crystals and assess their optical properties. By means of the experimental setup described previously [17], we recorded the intrinsic emission at the hBN band-edge at wavelengths $\sim 200 \text{ nm}$ for samples at cryogenic temperatures ($T=8\text{K}$). For all $h^{10}\text{B}^{14}\text{N}$, $h^{10}\text{B}^{15}\text{N}$, and $h^{11}\text{B}^{15}\text{N}$ crystals, and the reference $h^{\text{nat}}\text{BN}$ one, intense emission with narrow PL lines is recorded, attesting again to high crystalline quality of the samples (Figure 52a). As with the high-energy Raman mode (Figure 49), the PL spectrum varies

smoothly with the isotopic content, with a progressive blue-shift as a function of the reduced mass (Figure 52a). Similar to the E_{2g}^{high} Raman-mode, the new $h^{10}\text{B}^{15}\text{N}$ and $h^{11}\text{B}^{15}\text{N}$ configurations appear as “mirror images” of $h^{10}\text{B}^{14}\text{N}$ and $h^{11}\text{B}^{14}\text{N}$ with respect to $h^{\text{nat}}\text{BN}$ in the PL data set of (Figure 52). The shift of the PL spectra with isotopic composition stems from the indirect nature of the bandgap in bulk hBN, where the intrinsic emission results from phonon-assisted recombination [17,36-39]. Since all PL lines are phonon replicas in Figure 52a, their spectral position directly depends on the energy of the specific phonon mode involved in the recombination process [17], hence on the isotopic composition of the hBN crystal. The lines at ~ 5.77 eV are the most detuned from the indirect bandgap because they correspond to the emission of LO phonons, of highest energy in the phonon band structure [36]. As a consequence, the isotopic shift is also maximal for LO phonons, thus explaining the increasing isotopic shift of the PL lines on reducing the detection energy in the PL spectra of Figure 52a. We performed a quantitative interpretation of the PL spectra following the procedure previously employed in Ref.[17]. By plotting the energy of the different phonon replicas as a function of the calculated values of the phonon energy at the T point of the Brillouin zone, we extracted the energy of the fundamental indirect exciton for each monoisotopic hBN crystal (Figure 52b). Such an analysis reveals the few-meV variations of hBN bandgap with the isotopic composition, which come from the zero-point renormalization of the bandgap energy [17]. The possibility to investigate such a fine effect is again a signature of the high crystalline quality of all $h^{10}\text{B}^{14}\text{N}$, $h^{11}\text{B}^{14}\text{N}$, $h^{10}\text{B}^{15}\text{N}$, and $h^{11}\text{B}^{15}\text{N}$ crystals.

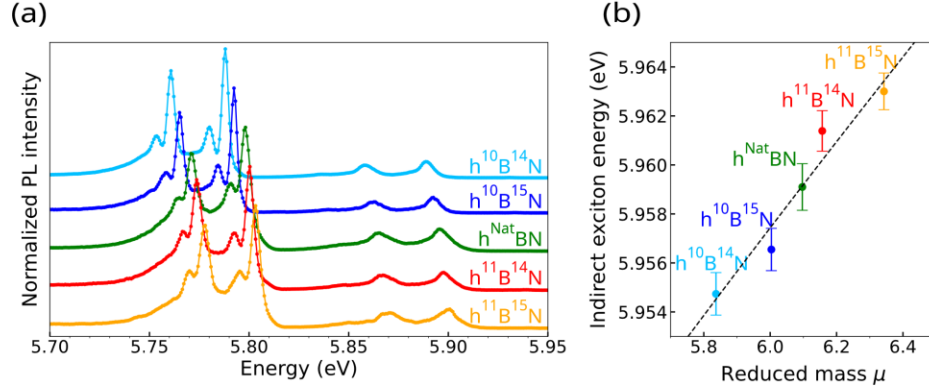


Figure 52 – a) Normalized photoluminescence spectra from hBN synthesized from different isotope combinations. b) Energy of the fundamental indirect exciton of each sample plotted versus its reduced mass.

5.4 Conclusions

In this work, we have developed a new 2-step process for the crystal growth of hBN with monoisotopic ^{15}N that efficiently uses $^{15}\text{N}_2$ gas and can produce hBN crystals with any isotope combination: $\text{h}^{10}\text{B}^{14}\text{N}$, $\text{h}^{10}\text{B}^{15}\text{N}$, $\text{h}^{11}\text{B}^{14}\text{N}$, or $\text{h}^{11}\text{B}^{15}\text{N}$. The first step consists of the formation of an homogenous ingot from isotopically pure boron powder (^{10}B or ^{11}B) mixed with Ni and Cr powder while removing oxygen impurities. The second step consists of the growth of hBN crystals from the ingot using a sealed tube containing $^{15}\text{N}_2$ gas and hydrogen. This step produces hBN crystals with a comparable size and clarity to those achieved by previous methods.

Raman spectroscopy reveals the achievement of ^{15}N -purified hBN crystals of the same high-quality as for ^{14}N , as demonstrated by the experimental $\sim 4\text{ cm}^{-1}$ -width of the high-energy Raman line. On the one hand, the frequency of the high-energy Raman mode progressively red-shifts with the reduced mass in the unit cell, from $\sim 1393\text{ cm}^{-1}$ in $\text{h}^{10}\text{B}^{14}\text{N}$ to $\sim 1335\text{ cm}^{-1}$ in $\text{h}^{11}\text{B}^{15}\text{N}$. On the other hand, the behavior of the low-energy Raman line corresponding to the interlayer shear mode is non-monotonous, with strikingly the same approximate frequency in

$h^{10}B^{14}N$ and $h^{10}B^{15}N$ crystals. Our results agree with our ab-initio calculations of the vibrational properties as a function of the isotopic composition.

The high-quality of the four isotopically-purified hBN crystals is further proven by photoluminescence (PL) spectroscopy excited in the UV-C spectral range, above the hBN bandgap. Intense and narrow PL lines are recorded, with a smooth blue-shift of the PL spectrum as a function of the reduced mass, as expected for indirect-gap bulk hBN where the intrinsic band-edge emission stems from phonon-assisted recombination. Quantitative analysis of the PL spectra allows to extract the variations of the indirect bandgap with the isotopic composition.

The work expands the range of properties that can be achieved by varying the isotopic composition of hBN. This will be a major benefit for tailoring the properties to optimize the performance of electronic, optoelectronic, nanophotonic, and quantum devices based on hBN.

5.5 References

- [1] J.D. Caldwell, I. Aharonovich, G. Cassabois, J.H. Edgar, B. Gil, and D. Basov, *Nat. Rev. Mater.* 2019, 4, 552.
- [2] T. Knobloch, Y.Yu. Illarionov, F. Ducry, C. Schleich, S. Wachter, K. Watanabe, T. Taniguchi, T. Mueller, M. Walzl, M. Lanza, M.I. Vexler, M. Luisier, and T. Grasser, *Nat. Electron.* 2021, 4, 98.
- [3] S. Das, A. Sebastian, E. Pop C.J. McClellan, A.D. Franklin, T. Grasser, T. Knobloch, Y. Illarionov, A.V. Panumatcha, J. Appenzeller, Z.H. Chen, W.J. Zhu, I. Asselberghs, L.J. Li, U.E. Avci, N. Bhat, T.D. Anthopoulos, and R. Singh, *Nat. Electron.* 2021, 4, 786.
- [4] A. Gottscholl, M. Kianinia, V. Soltamov, S. Orlinskii, G. Mamin, C. Bradac, C. Kasper, K. Krambrock, A. Sperlich, M. Toth, I. Aharonovich, and V. Dyakonov, *Nat. Mater.* 2020, 19, 540.
- [5] V. Ivády, G. Barcza, G. Thiering, S. Li, H. Hamdi, J.-P. Chou, Ö. Legeza and A. Gali, *NPJ Comp. Mater.* 2020 6 41.
- [6] I. Dolado, C. Maciel-Escudero, E. Nikulina, E. Modin, F. Calavalle, S. Chen, A. Bylinkin, F.J. Alfaro-Mozaz, J. Li, J.H. Edgar, F. Casanova, S. Vélez, L.E. Hueso, R. Esteban, J. Aizpurua, and R. Hillenbrand, *Nat. Comm.* 2022, 13,6850.
- [7] M. He, G.R. S. Iyer, S. Aarav, S.S. Sunku, A.J. Giles, T.G. Folland, N. Sharac, X. Sun, J. Matson, S. Liu, J.H. Edgar, J.W. Fleischer, D.N. Basov and J.D. Caldwell, *Nano Lett.* 2021, 21, 7912.
- [8] K. Zhu, S. Pazos, F. Aguirre, Y. Shen, Y. Yuan, W. Zheng, O. Alharbi, M.A. Villena, B. Fang, X. Li, A. Milozzi, M. Farronato, M. Muñoz-Rojo, T. Wang, R. Li, H. Fariborzi, J.B.

- Roldan, G. Benstetter, X. Zhang, H. Alshareef, T. Grasser, H. Wu, D. Ielmini and M. Lanza, *Nature* 2023, 618, 57.
- [9] M. Kim, E. Pallecchi, R. Ge, X. Wu, G. Ducournau, J.C. Lee, H. Happy, and D. Akinwande, *Nat. Electron.* 2020, 3, 479.
- [10] H.L. Stern, J. Jarman, Q. Gu, S.E. Barker, N. Mendelson, D. Chugh, S. Schott, H.H. Tan, H. Siringhaus, I. Aharonovich and M. Atatüre, *Nat. Comm.* 2022, 13, 618.
- [11] H. Korkut and I. Sarpkaya, *2D Mater.* 2023, 10, 015004.
- [12] N. Kinsey, C. DeVault, A. Boltasseva and V.M. ShalaeV, *Nat. Rev. Mater.* 2019, 4, 742.
- [13] F. J. Rodríguez-Fortuño, A., Vakil, and N. Engheta, *Phys. Rev. Lett.* 2014, 112, 033902.
- [14] J.W. Meadows and J.F. Whalen, *Nucl. Sci. Eng.* 1970, 40, 12.
- [15] S. Liu, R. He, L. Xue, J. Li, B. Liu, and J.H. Edgar, *Chem. Mater.* 2018 30, 6222.
- [16] J. Li, C. Elias, Z. Ye, D. Evans, S. Liu, R. He, G. Cassabois, B. Gil, P. Valvin, B. Liu and J.H. Edgar, *J. Mater. Chem. C* 2020, 8, 9931.
- [17] T.Q.P. Vuong, S. Liu, A. Van der Lee, R. Cuscó, L. Artús, T. Michel, P. Valvin, J.H. Edgar, G. Cassabois, and B. Gil, *Nat. Mater.* 2018, 17, 152.
- [18] A.J. Giles, S. Dai, I. Vurgaftman, T. Hoffman, S. Liu, L. Lindsay, C.T. Ellis, N. Assefa, I. Chatzakis, T.L. Reinecke, J.G. Tischler, M.M. Fogler, J.H. Edgar, D.N. Basov, and J.D. Caldwell, *Nat. Mater.* 2018, 17, 134.
- [19] R. Cuscó, J.H. Edgar, J. Li, S. Liu, and L. Artus, *Phys. Rev. Lett.* 2020, 124, 167402.
- [20] R. Cuscó, J.H. Edgar, S. Liu, G. Cassabois, B. Gil, and L. Artús, *J. Phys. D* 2019, 52, 303001.
- [21] G. Pavlidis, J. J. Schwartz, J. Matson, T. Folland, S. Liu, J. Edgar, J. D. Caldwell, and A. Centrone, *Appl. Phys. Lett. Mater.* 2021, 9, 091109.
- [22] L. Lindsay and D.A. Broido, *Phys. Rev. B* 2011, 84, 155421.
- [23] C. Yuan, J. Li, S. Liu, J.H. Edgar, L. Lindsay, D. Cherns, *Commun. Phys.* 2019, 2, 43.
- [24] E. Mercado, C. Yuan, Y. Zhou, J. Li, J.H. Edgar, and M. Kuball, *ACS Appl. Nano Mater.* 2020, 3, 12148.
- [25] Q. Cai, D. Scullion, W. Gan, A. Falin, P. Cizek, S. Liu, J.H. Edgar, R. Liu, B.C.C. Cowie, E.J.G Santos, and L.H. Li, *Phys. Rev. Lett.* 2020, 125, 085902.
- [26] Q. Cai, D. Scullion, W. Gan, A. Falin, S. Zhang, K. Watanabe, T. Taniguchi, Y. Chen, E.J. G. Santos and L.H. Li, *Sci. Adv.* 2019, 5, eaav0129.
- [27] A. Brasington, S. Liu, T. Taniguchi, K. Watanabe, J.H. Edgar, B. LeRoy, and A. Sandhu, *Phys. Status Solidi Rapid Res. Lett.* 2022, 16, 2200030.
- [28] P. Li, I. Dolado, F.J. Alfaro-Mozaz, F. Casanova, L.E. Hueso, S. Liu, J.H. Edgar, A.Y. Nikitin, S. Vélez, and R. Hillenbrand, *Science* 2018, 359, 892.
- [29] A. Bylinkin, M. Schnell, M. Autore, F. Calavalle, J. Taboada-Gutiérrez, S. Liu, J.H. Edgar, F. Casanova, L.E Hueso, P. Alonso-Gonzalez, A.Y. Nikitin, and R. Hillenbrand, *Nat. Photon* 2021, 15, 197.
- [30] T.G. Folland, A. Fali, S.T. White, J.R. Matson, S. Liu, N. Aghamiri, J.H. Edgar, R.F. Haglund, Jr., Y. Abate, and J.D. Caldwell, *Nat. Comm.* 2018, 9, 4371.
- [31] A. Haykal, R. Tanos, N. Minotto, A. Durand, F. Fabre, J. Li, J. Edgar, V. Ivady, A. Gali, T. Michel, A. Dréau, B. Gil, G. Cassabois, and V. Jacques, *Nat. Comm.* 2022, 13, 4347.
- [32] M. He, L. Lindsay, T.E. Beechem, T. Folland, J. Matson, K. Watanabe, A. Zavalin, A. Ueda, W. E. Collins, T. Taniguchi and J.D. Caldwell, *J. Mater. Res.* 2021, 35, 4394.
- [33] W. Cochrane and A.G. Hester, *Proc. Royal Soc. London Ser A* 1949, 199, 458.
- [34] G. Jeschke, W. Hoffbauer, and M. Jansen, *Solid State Nucl. Magn. Reson.* 1998, 12, 1.

- [35] C.M. Marian and M. Gastreich, Quantitative structure-property relationships in boron nitrides: the N-15 and B-11 chemical shifts, *Solid State Nuclear Magnetic Resonance* 2001, 19, 29.
- [36] R. Cusco, B. Gil, G. Cassabois, and L. Artus, *Phys. Rev. B* 2016, 94, 155435.
- [37] G. Cassabois, P. Valvin, and B. Gil, *Nat. Phot.* 2016, 10, 262.
- [38] T.Q.P. Vuong, G. Cassabois, P. Valvin, V. Jacques, A. Van Der Lee, A. Zobelli, K. Watanabe, T. Taniguchi, and B. Gil, *2D Mater.* 2017, 4, 011004.
- [39] T.Q.P. Vuong, G. Cassabois, P. Valvin, V. Jacques, R. Cusco, L. Artus, and B. Gil, *Phys. Rev. B* 2017, 95, 045207.

Chapter 6 – Conclusions and Recommendations

A new methodology was developed to rapidly optimize the boron concentration for hBN solution growth in an arbitrary solvent with the CALPHAD Method (Section 2.1). This accurately the optimal initial boron concentration in two systems, Ni-Cr and Fe, indicating that it will likely be accurate in other systems as well (Section 2.2). This opens up some new possibilities for hBN solution growth research. First, a survey of many different solvents, solvent ratios, and additives could be explored with this procedure to quickly find new solvents that are optimal for this process. This also doesn't need to be limited only to predicting hBN precipitation but could potentially predict precipitation of impurities of impurities like C and O as well, allowing methods of purification to be rapidly explored as well. Second, the CALPHAD predictions performed in this work showed that the liquidus curve of hBN versus temperature has a different slope for each solvent. This determines how quickly the hBN solubility changes with temperature, and thus how quickly hBN precipitates from solution. Future work should explore if this has a measurable effect on hBN solution growth and determine how to adjust growth parameters to compensate for it if it does.

The hBN solution growth process was demonstrated to be kinetically limited due to observed deviations from CALPHAD predictions and the ability to precipitate more hBN from recycled source material (Section 2.3). The kinetic limitation was attributed to the formation of a layer of hBN at the gas-liquid interface that blocked mass transport of N_2 into the solution and starved the reaction of one of its two components. Therefore, an experimental setup should be developed to maximize the gas-liquid surface area to volume ratio so that a maximal amount of boron can be converted to hBN using a minimal amount of solvent. Until then, recycling source materials multiple times also enables more efficient use of source materials.

In experiments comparing the size of crystals grown from different solvents with different nitrogen solubilities, the crystal area was determined to be insensitive to the nitrogen solubility so long as it was properly optimized while the optimal boron concentration and thickness increased with increasing nitrogen solubility (Sections 3.1 and 3.2). The insensitivity of crystal area was hypothesized to be due to nucleation being primarily controlled by the degree of supersaturation. The increase in hBN crystal thickness was hypothesized to be caused by an increase in nitrogen concentration in the bulk of the solvent that accompanies an increase in nitrogen solubility (Section 3.3). This trend in thickness could be used to engineer crystals to be a certain thickness without needing to mechanically exfoliate them, which could cause damage. The trend between the optimal boron concentration and the nitrogen solubility provides an estimate for the optimal conditions for future solvents, accelerating research, though mid-range nitrogen solubility solvents are needed to confirm the trend.

Carbon and oxygen impurities present in the source materials, crystal growth solution, and hBN crystals were analyzed using a combination of inert gas fusion and secondary ion mass spectrometry (Section 4.1). The results show that oxygen impurities are significantly reduced through a few different mechanisms including reaction with hydrogen, vaporization of boron oxide, or reaction with carbon impurities. Carbon impurities that originate with the source material may need to react with oxygen to be removed from the solution. To further reduce carbon in the system, oxygen could be intentionally introduced to the system, then removed in a subsequent step by reaction with hydrogen. Regardless, SIMS analysis on hBN crystals could not positively identify either carbon or oxygen, suggesting that the purity of the process is already sufficient. Future work should include using quantifying impurity content with

cathodoluminescence or photoluminescence spectroscopy, which are expected to be more sensitive to impurities than SIMS.

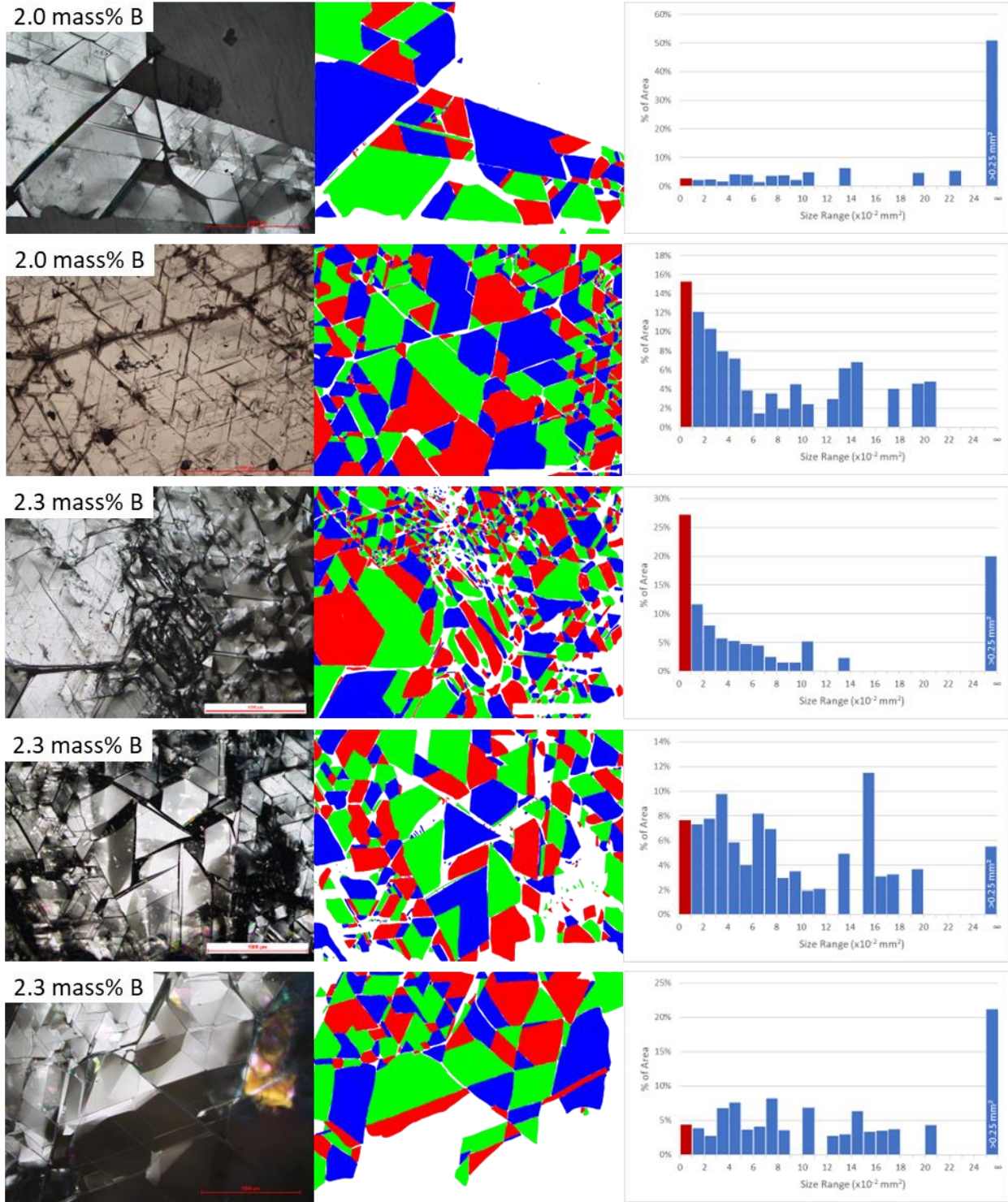
Two new classes of defects were discovered and identified in this work: invisible lines and wrinkles (Section 4.2). The former was identified as half-inserted planes, which are unlikely to be a major detriment to carrier mobility in devices, while the latter was formed by post-growth deformation of the crystals. Determining why this deformation occurs will inform how to prevent it from forming and dramatically increase the size of pristine domains. A potential method to discover why the wrinkles form is to carefully strain pristine crystals that have been separated from the solvent, attempting to recreate the formation of wrinkles in a controlled environment.

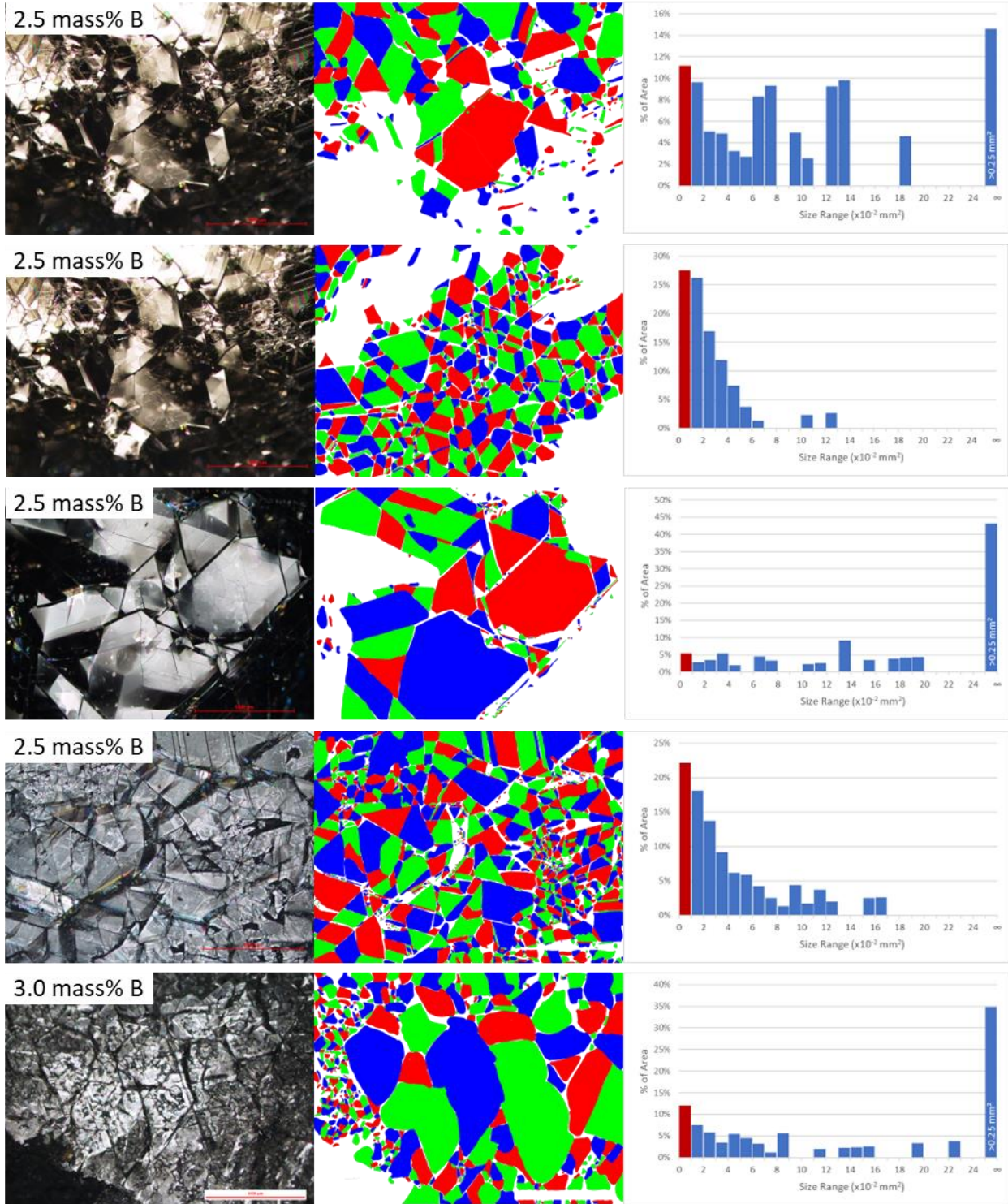
Crystal quality was quantified with Raman, photoluminescence, and cathodoluminescence spectroscopy, which showed that crystals grown from Fe-V, Ni-Cr, and Co-Cr were typically higher quality than those grown from Fe or Cu (Section 4.3). Of these, Co-Cr seems to be the most promising solvent, having frequently produced the highest-quality crystals some of the largest, so production of hBN would benefit from using it. In addition, more work should be done with Fe-V solvents because it consistently grew high-quality hBN despite not being properly optimized.

In the process of using cathodoluminescence spectroscopy to analyze defects and crystal quality, an algorithm was developed that can be used to quantify quality both between different samples and within an hBN flake (Sections 4.2.1, 4.3.3, and Appendix B). This will be a helpful tool for quantifying the effect of process parameters in the future but could also identify the highest-quality regions within a flake. For example, in manufacturing a device that is highly sensitive to defects, a CL map could be taken, pristine regions could be identified with this tool, and the device could be constructed to make use of this region.

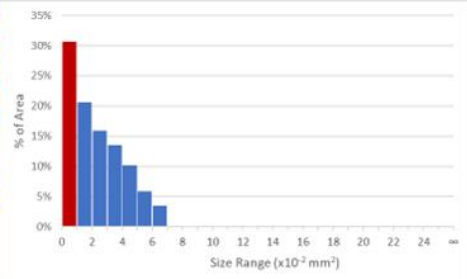
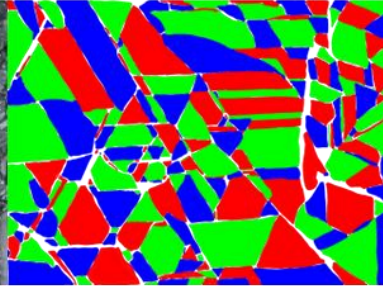
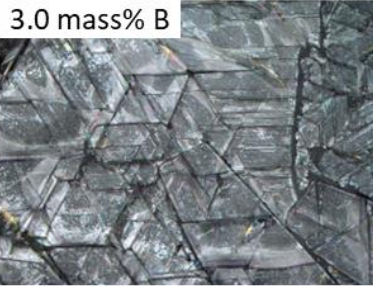
A new process was developed to extend the capabilities of monoisotopic hBN to include $h^{10}B^{15}N$ and $h^{11}B^{15}N$ in addition to $h^{10}B^{15}N$ and $h^{11}B^{15}N$ developed in past work (Chapter 5). These crystals will be especially useful in applications where coherence of phonons is especially important such as sub-wavelength optical microscopy and quantum sensing. This process could be further improved by reducing the volume that must be filled with $^{15}N_2$ to make more efficient use of the expensive gas. Furthermore, any future advances to more traditional hBN solution growth could be easily adapted to improve this process as well.

Appendix A- Images for Determining Domain Size Distribution

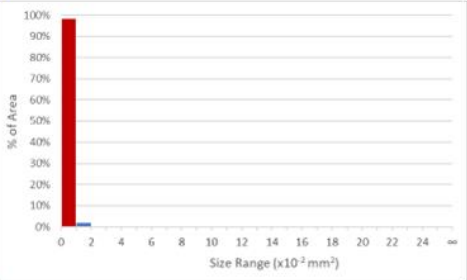
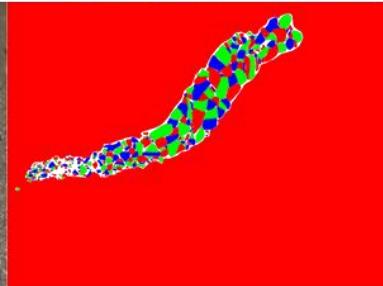
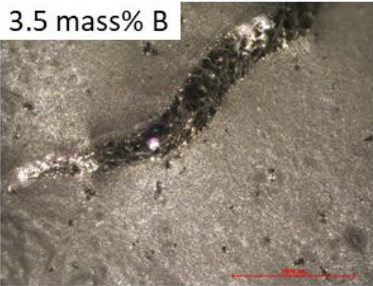




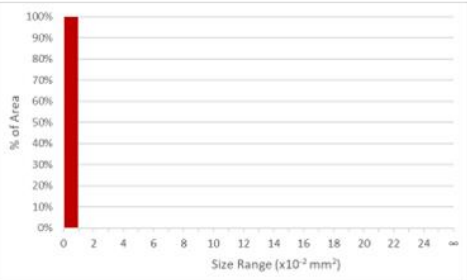
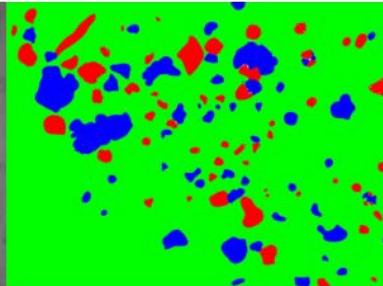
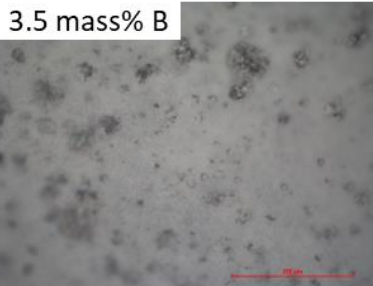
3.0 mass% B



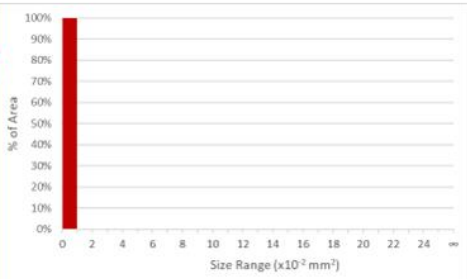
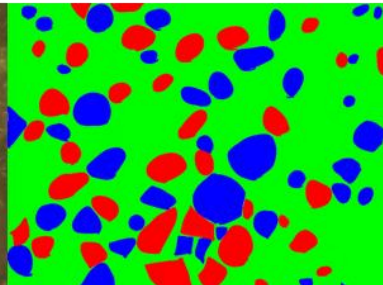
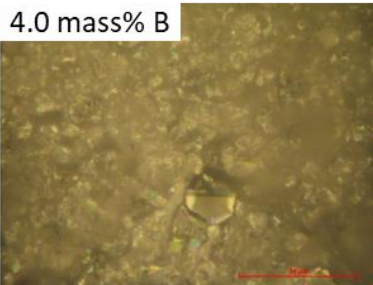
3.5 mass% B



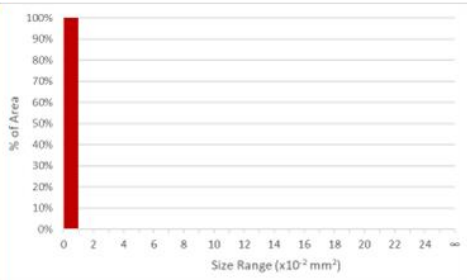
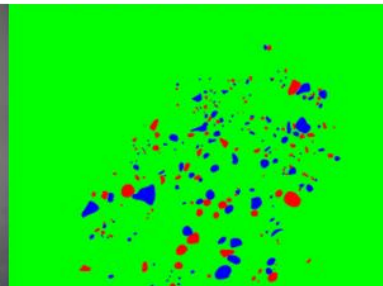
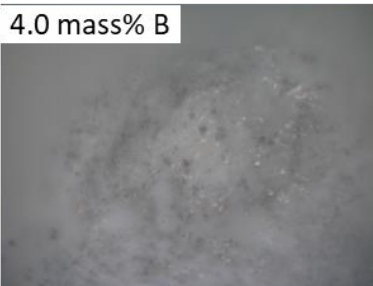
3.5 mass% B



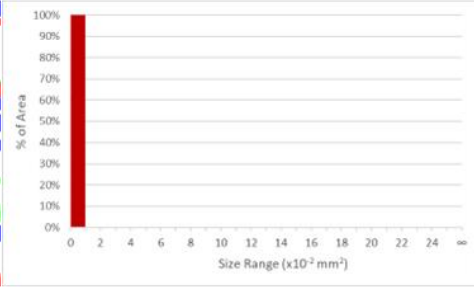
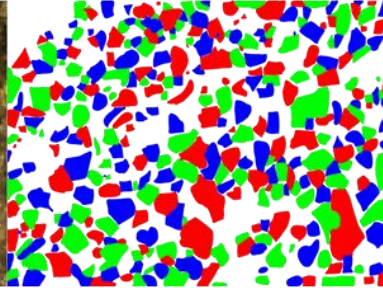
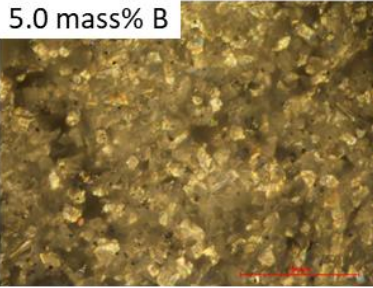
4.0 mass% B



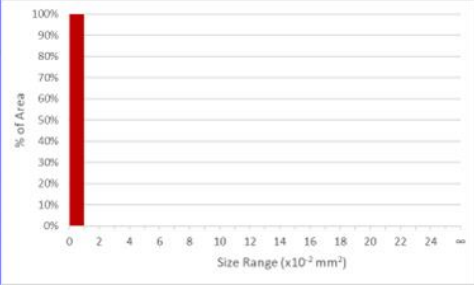
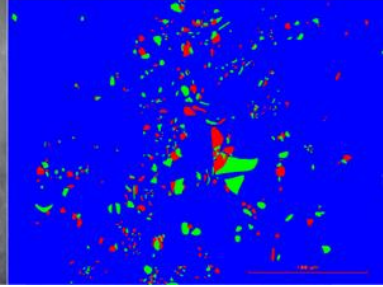
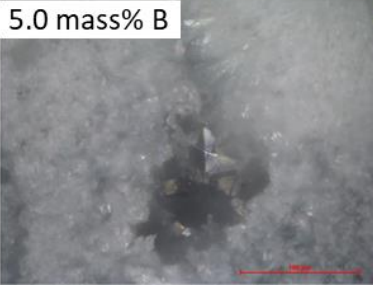
4.0 mass% B



5.0 mass% B



5.0 mass% B



Appendix B - Code for CL Data Analysis

B.1 Code for Decomposition

The code below was written in Python 3.9 to perform decomposition on CL maps collected with the software package ScopeFoundry (available here: <https://www.scopefoundry.org/>) and is intended to be run interactively in a Jupyter Notebook.

```
1. #libs
2.
3. import os
4. from pathlib import Path, PurePath
5. import numpy as np
6. import math
7. import h5py
8. import matplotlib as mpl
9. import matplotlib.pyplot as plt
10. import copy
11. import csv
12.
13. import hyperspy.api as hs
14. import hyperspy_gui_ipywidgets
15.
16. #SCOPEFOUNDRY CLASS
17. from hyperspy.misc.utils import DictionaryTreeBrowser
18. import matplotlib.pyplot as plt
19. from matplotlib import gridspec
20. import hyperspy.api as hs
21. class ScopeFoundryLoader:
22.     #usage load scope foundry h5 into a dict
23.     def __init__(self, fname):
24.         self.fname = fname
25.         #util funcs
26.         def myinterp(x,y,xnew,method='linear') :
27.             from scipy.interpolate import interp1d
28.             finterp=interp1d(x,y,kind=method,axis=-1)
29.             ynew=finterp(xnew)
30.             return ynew
31.
32.         #add check if file corrupt from chris
33.
34.         #recursive crawlers making dict of dicts
```

```

35.
36.     def load_dict_from_hdf5(filename):
37.         with h5py.File(filename, 'r') as h5file:
38.             return
39.             recursively_load_dict_contents_from_group(h5file, '/')
40.     def recursively_load_dict_contents_from_group(h5file,
41. path):
42.         ans = {}
43.         for key, item in h5file[path].items():
44.             if isinstance(item, h5py._hl.dataset.Dataset):
45.                 ans[key] = item[()]
46.             elif isinstance(item, h5py._hl.group.Group):
47.                 ans[key] =
48.                 recursively_load_dict_contents_from_group(h5file, path + key +
49.                 '/')
50.                 for k,v in h5file[path].attrs.items():
51.                     ans[k]=v
52.
53.             return ans
54.
55.     #interpret file type
56.     def interpret_scope_foundry(self):
57.         if 'hyperspec_picam_mcl' in
58.         self.data_dict['measurement']:
59.             #hyperspectral HIP microscope data
60.             #creating easy access important metadata as
61.             Dicttree tree
62.             self.metadata = DictionaryTreeBrowser()
63.             # hardware settings
64.             self.metadata.experiment_type = 'Raman/PL
65.             hyperspectral image'
66.             self.metadata.grating_name =
67.             self.data_tree.hardware.acton_spectrometer.settings.grating_name
68.             self.metadata.center_wl =
69.             self.data_tree.hardware.acton_spectrometer.settings.center_wl
70.             self.metadata.exposure_time =
71.             self.data_tree.hardware.picam.settings.ExposureTime
72.             self.metadata.length = 1340
73.             #a.data_tree.hardware.settings.picam.xxxxxx
74.             self.metadata.laser_power =
75.             self.data_tree.hardware.power_wheel.settings.position
76.             self.metadata.laser_wl = 532.0
77.             self.metadata.calibration = 'wls'
78.             #measurments settings

```

```

69.         self.metadata.x_size =
self.data_tree.measurement.hyperspec_picam_mcl.settings.Nh
70.         self.metadata.y_size =
self.data_tree.measurement.hyperspec_picam_mcl.settings.Nv
71.         self.metadata.x_pix_size =
self.data_tree.measurement.hyperspec_picam_mcl.settings.dh
72.         self.metadata.y_pix_size =
self.data_tree.measurement.hyperspec_picam_mcl.settings.dv
73.         self.metadata.FOV = [self.metadata.x_size *
self.metadata.x_pix_size,
74.                             self.metadata.y_size *
self.metadata.y_pix_size]
75.         self.metadata.pix_size_unit = 'um'
76.         self.metadata.pix_time =
self.data_tree.measurement.hyperspec_picam_mcl.settings.pixel_time
77.         #data
78.         self.description =
self.data_tree.app.settings.sample
79.         self.spec_map =
self.data_tree.measurement.hyperspec_picam_mcl.spec_map
80.         self.wls
= self.data_tree.measurement.hyperspec_picam_mcl.wls #calibrated at acquisition
81.         self.wns
= self.data_tree.measurement.hyperspec_picam_mcl.wave_numbers
#calculated at acquisition
82.         self.dwns =
self.data_tree.measurement.hyperspec_picam_mcl.raman_shifts
#calculated at acquisition
83.
84.         elif 'picam_asi_hyperspec_scan' in
self.data_dict['measurement']:
85.             #hyperspectral HIP microscope data
86.             #creating easy access important metadata as
Dicttree tree
87.             self.metadata = DictionaryTreeBrowser()
88.             # hardware settings
89.             self.metadata.experiment_type = 'Raman/PL
hyperspectral image'
90.             self.metadata.grating_name =
self.data_tree.hardware.acton_spectrometer.settings.grating_name
91.             self.metadata.center_wl =
self.data_tree.hardware.acton_spectrometer.settings.center_wl
92.             self.metadata.exposure_time =
self.data_tree.hardware.picam.settings.ExposureTime

```

```

93.             self.metadata.length = 1340
           #a.data_tree.hardware.settings.picam.xxxxxx
94.             self.metadata.laser_power =
           self.data_tree.hardware.power_wheel.settings.position
95.             self.metadata.laser_wl = 532.0
96.             self.metadata.calibration = 'wls'
97.             #measurements settings
98.             self.metadata.x_size =
           self.data_tree.measurement.picam_asi_hyperspec_scan.settings.Nh
99.             self.metadata.y_size =
           self.data_tree.measurement.picam_asi_hyperspec_scan.settings.Nv
100.            self.metadata.x_pix_size =
           self.data_tree.measurement.picam_asi_hyperspec_scan.settings.dh
101.            self.metadata.y_pix_size =
           self.data_tree.measurement.picam_asi_hyperspec_scan.settings.dv
102.            self.metadata.FOV = [self.metadata.x_size *
           self.metadata.x_pix_size,
103.                                self.metadata.y_size *
           self.metadata.y_pix_size]
104.            self.metadata.pix_size_unit = 'um'
105.            self.metadata.pix_time =
           self.data_tree.measurement.picam_asi_hyperspec_scan.settings.pixe
           l_time
106.            #data
107.            self.description =
           self.data_tree.app.settings.sample
108.            self.spec_map =
           self.data_tree.measurement.picam_asi_hyperspec_scan.spec_map
109.            self.wls
           = self.data_tree.measurement.picam_asi_hyperspec_scan.wls #cali
           brated at acquisition
110.            #self.wns
           = self.data_tree.measurement.picam_asi_hyperspec_scan.wave_numbe
           rs #calculated at acquisition
111.            #self.dwns =
           self.data_tree.measurement.picam_asi_hyperspec_scan.raman_shifts
           #calculated at acquisition
112.
113.            elif 'hyperspec_cl' in
           self.data_dict['measurement']:
114.                #hyperspectral cl microscope data
115.                #creating easy access important metadata as
           Dicttree tree
116.                self.metadata = DictionaryTreeBrowser()
117.                # hardware settings

```

```

118.         self.metadata.experiment_type = 'CL spectral
map'
119.         self.metadata.grating_name =
self.data_tree.hardware.andor_spec.settings.grating_name
120.         self.metadata.center_wl =
self.data_tree.hardware.acton_spectrometer.settings.center_wl
121.         self.metadata.exposure_time =
self.data_tree.hardware.andor_ccd.settings.exposure_time
122.         self.metadata.em_gain =
self.data_tree.hardware.andor_ccd.settings.em_gain
123.         self.metadata.length = 1600
124.         self.metadata.calibration = 'wls'
125.         self.metadata.kV=self.data_tree.hardware.sem_re
mcon.settings.kV
126.         self.metadata.magnification=self.data_tree.hard
ware.sem_remcon.settings.magnification
127.         #measurments settings
128.         self.metadata.x_size =
self.data_tree.measurement.hyperspec_cl.settings.Nh
129.         self.metadata.y_size =
self.data_tree.measurement.hyperspec_cl.settings.Nv
130.         self.metadata.x_pix_size =
self.data_tree.measurement.hyperspec_cl.settings.dh*4.25*2.54e7/(
20*self.metadata.magnification)
131.         self.metadata.y_pix_size =
self.data_tree.measurement.hyperspec_cl.settings.dv*4.25*2.54e7/(
20*self.metadata.magnification)
132.         self.metadata.FOV = [self.metadata.x_size *
self.metadata.x_pix_size,
133.                               self.metadata.y_size *
self.metadata.y_pix_size]
134.         self.metadata.pix_size_unit = 'nm'
135.         self.metadata.pix_time =
self.data_tree.measurement.hyperspec_cl.settings.pixel_time
136.         self.metadata.description=self.data_tree.measur
ement.hyperspec_cl.settings.description
137.         #data
138.         self.description =
self.data_tree.app.settings.sample
139.         self.spec_map =
self.data_tree.measurement.hyperspec_cl.spec_map
140.         self.wls =
self.data_tree.measurement.hyperspec_cl.wls #calibrated at
acquisition
141.         self.adc =
self.data_tree.measurement.hyperspec_cl.adc_map

```

```

142.             self.ctr =
143.             self.data_tree.measurement.hyperspec_cl.ctr_map
144.             elif 'sync_raster_scan' in
145.             self.data_dict['measurement']:
146.                 #imaging cl microscope data
147.                 #creating easy access important metadata as
148.                 Dicttree tree
149.                 self.metadata = DictionaryTreeBrowser()
150.                 # hardware settings
151.                 self.metadata.experiment_type = 'CL bandpass
152.                 map'
153.                 self.metadata.kV=self.data_tree.hardware.sem_re
154.                 mcon.settings.kV
155.                 self.metadata.magnification=self.data_tree.hard
156.                 ware.sem_remcon.settings.magnification
157.                 #measurments settings
158.                 self.metadata.x_size =
159.                 self.data_tree.measurement.sync_raster_scan.settings.Nh
160.                 self.metadata.y_size =
161.                 self.data_tree.measurement.sync_raster_scan.settings.Nv
162.                 self.metadata.x_pix_size =
163.                 self.data_tree.measurement.sync_raster_scan.settings.dh*4.25*2.54
164.                 e7/(20*self.metadata.magnification)
165.                 self.metadata.y_pix_size =
166.                 self.data_tree.measurement.sync_raster_scan.settings.dv*4.25*2.54
167.                 e7/(20*self.metadata.magnification)
168.                 self.metadata.FOV = [self.metadata.x_size *
169.                 self.metadata.x_pix_size,
170.                 self.metadata.y_size *
171.                 self.metadata.y_pix_size]
172.                 self.metadata.pix_size_unit = 'nm'
173.                 self.metadata.pix_time =
174.                 self.data_tree.measurement.sync_raster_scan.settings.pixel_time
175.                 #data
176.                 self.description =
177.                 self.data_tree.app.settings.sample
178.                 self.adc =
179.                 self.data_tree.measurement.sync_raster_scan.adc_map
180.                 self.ctr =
181.                 self.data_tree.measurement.sync_raster_scan.ctr_map
182.
183.             return self
184.
185.             # add as dictionary
186.             self.data_dict = load_dict_from_hdf5(self.fname)

```

```

170.         #add as hyperspys dictionary tree [cute display easy to
        use]
171.         self.data_tree = DictionaryTreeBrowser(self.data_dict)
172.         try:
173.             self = interpret_scope_foundry(self)
174.         except KeyError:
175.             print('Interpreter Error!')
176.
177.     def deepcopy(self):
178.         return copy.deepcopy(self)
179.
180.     #Create new Scope Foundry Loader object with a section of
        the original data
181.     #Currently only tested on CL data
182.     def crop(self, shape):
183.         for i,s in enumerate(shape):
184.             if s is None:
185.                 shape[i]=[0,self.spec_map.shape[i]]
186.
187.             new_datum=self.deepcopy()
188.             new_datum.spec_map=new_datum.spec_map[shape[0][0]:shape
        [0][1],shape[1][0]:shape[1][1],shape[2][0]:shape[2][1],shape[3][0
        ]:shape[3][1],shape[4][0]:shape[4][1]]
189.             new_datum.wls=new_datum.wls[shape[4][0]:shape[4][1]]
190.             return new_datum
191.
192.     #hyperspy maker
193.     def make_hspy_si(datacube,spec_vect,
194.                     pix_size = [1,1],
195.                     x_units='nm',spec_units='nm',
196.                     title='experiment'):
197.         #returns hyperspy object of equally spaced
198.         # datacube is x-y-wavelength spectral map
199.         # spec_vect is the wavelength values and has to be the
        same length and the third dimation of datacube
200.         # pix_size is [ x y ] pixel size in x_units
201.         # x_units is units string
202.         # spec_units is control variable
203.         # converts to eV using jacobian transform if not 'ev'
204.         # converts to wavenumbers using jacobian transform if
        not 'wavenumbers'
205.         # converts to wavenumbers using jacobian transform if
        not 'wavenumbers'
206.
207.     def myinterp(x,y,xnew,method='linear') :
208.

```

```

209.         from scipy.interpolate import interp1d
210.         finterp=interp1d(x,y,kind=method,axis=-1)
211.         ynew=finterp(xnew)
212.         return ynew
213.
214.
215.     #Squeezing datacube to 3D (x,y,wavelength)
216.     I_wls=np.squeeze(datacube)
217.     wls=spec_vect
218.     #output spectral dimension (set same as input spatial
    dimation)
219.     dim = datacube.shape
220.
221.     #spec axis - forcing equal spacing
222.     new_wls=np.linspace(spec_vect[0],spec_vect[-
    1],len(spec_vect))
223.     newdatacube=myinterp(spec_vect,datacube,new_wls)
224.
225.     si = hs.signals.Signal1D(newdatacube)
226.
227.     # wls units in nm
228.     si.axes_manager[2].name = 'Wavelength'
229.     si.axes_manager[2].offset = new_wls[0]
230.     si.axes_manager[2].scale = new_wls[1]-new_wls[0]
231.     si.axes_manager[2].units = 'nm'
232.
233.     si.metadata.General.title = title
234.
235.     # xunits in nm
236.     si.axes_manager[0].name = 'x'
237.     si.axes_manager[0].scale = pix_size[0]
238.     si.axes_manager[0].units = x_units
239.
240.     #y units in nm
241.     si.axes_manager[1].name = 'y'
242.     si.axes_manager[1].scale = pix_size[1]
243.     si.axes_manager[1].units = x_units
244.
245.
246.     return si
247.
248. #Display components from decomposition in one figure
249. def compsplo(loadings,factors,xff,comps =
    [0,1,2,3],xlabelstr="Wavelength ($nm$)"):
250.     #plots the components from 1 to 3
251.     #from loadings and factors

```

```

252.
253.     no_of_comps=len(comps)
254.     plt.figure(figsize=[10 ,2*len(comps)])
255.     idx=1
256.     for i in comps:
257.
258.         plt.subplot(no_of_comps,2,2*idx-1)
259.         plt.plot(xff,factors[i,:])
260.         #plt.xlim(-10,800)
261.         plt.xlabel(xlabelstr)
262.         plt.ylabel(" I ")
263.
264.         plt.subplot(no_of_comps,2,2*idx)
265.         plt.imshow(loadings[i,:,:],cmap='magma',
266.                    vmin=np.percentile(loadings[i,:,:],1),
267.                    vmax=np.percentile(loadings[i,:,:],99))
268.         plt.axis('image')
269.         plt.axis('off')
270.         plt.colorbar()
271.         plt.axis('image')
272.         plt.title('component ' + str(i))
273.
274.         idx+=1
275.     plt.tight_layout()
276.
277. #Creates an average spectrum from a CL map with appropriate
    axis labels
278. def ave_spectrum(datum,ax=None):
279.     ### Unresolved: Need to add ability to plot vs eV as well as nm
280.
281.     fig=plt.gcf()
282.     ax=ax or plt.gca()
283.
284.     ax.plot(datum.wls,datum.spec_map.squeeze().mean(axis=(0,1))
    ,color='black')
285.     ax.set_xlabel('Wavelength (nm)')
286.     ax.set_ylabel('Intensity (a.u.)')
287.     ax.set_title('Average CL Spectrum')
288.     return ax
289.
290. #Creates an image from a 2D array of data and applies a scale
    bar based on the given arguments
291. def
    plot_2D_map(im2d,ax=None,percentile=2,colormap='magma',x_pix_size
    = 1,x_pix_unit = 'pix',show_color_bar=True):

```

```

292. #This does the same things that myimshow does, with some added
    functionality
293.
294.     from mpl_toolkits.axes_grid1.anchored_artists import
    AnchoredSizeBar
295.     import matplotlib.font_manager as fm
296.
297.
298.     fig=plt.gcf()
299.     ax=ax or plt.gca()
300.
301.     imd = ax.imshow(im2d, cmap=colormap,
302.                    vmin=np.percentile(im2d,percentile),
303.                    vmax=np.percentile(im2d,100-percentile),
304.                    origin='lower')
305.
306.     #Add a color bar if show_color_bar = True
307.     if show_color_bar: fig.colorbar(imd,ax=ax)
308.
309.     #Remove the x and y axis tick marks
310.     ax.xaxis.set_visible(False)
311.     ax.yaxis.set_visible(False)
312.
313.     #Adjust units for scale bar
314.     if x_pix_unit=='pix':
315.         fov=x_pix_size*im2d.shape[0]
316.     else:
317.         #Calculate the pixel size and field of view in units of
    nm
318.         factor={'pm':0.001, 'nm':1, 'µm':1000, 'um':1000,
    'mm':1000000, 'm':1000000000}
319.         x_pix_size=x_pix_size*factor[x_pix_unit]
320.         fov=x_pix_size*im2d.shape[0]
321.
322.         #scale the pixel size and fov and change units
    appropriately
323.         if fov/5>=1000000000:
324.             x_pix_unit='m'
325.             x_pix_size=x_pix_size/1000000000
326.             fov=x_pix_size*im2d.shape[0]
327.         elif fov/5>=1000000:
328.             x_pix_unit='mm'
329.             x_pix_size=x_pix_size/1000000
330.             fov=x_pix_size*im2d.shape[0]
331.         elif fov/5>=1000:
332.             x_pix_unit='µm'

```

```

333.         x_pix_size=x_pix_size/1000
334.         fov=x_pix_size*im2d.shape[0]
335.     elif fov/5>=1:
336.         x_pix_unit='nm'
337.     else:
338.         x_pix_unit='pm'
339.         x_pix_size=x_pix_size*1000
340.         fov=x_pix_size*im2d.shape[0]
341.
342.     #Determine scalebar dimensions that make it about as long
    as 1/5th of the image
343.     label_vals =
    np.array([1,2,5,10,20,50,100,200,500,1000,2000,5000])
344.     lval = label_vals[np.argmin(np.abs(label_vals-fov/5))]
345.     sb_pixs =np.ceil( lval/x_pix_size )
346.
347.     fontprops = fm.FontProperties(size=10, weight=1000)
348.     scalebar = AnchoredSizeBar(ax.transData,
349.                               sb_pixs, str(lval)+'
    '+x_pix_unit , 'lower right',
350.                               pad=0.2,
351.                               frameon=True,
352.                               size_vertical=5,
353.                               color='black',
354.                               label_top = True,
355.                               fontproperties=fontprops)
356.
357.     ax.add_artist(scalebar)
358.
359.     return ax
360.
361. #Plots a summary of the CL maps with the average spectra color
    coded to the image produced by each detector
362. def si_summary_banded(datum,title='CL Spectral Map Summary'):
363. #data is a scopefoundryloader object
364. ### Unresolved: Still need to add input argument for wavelength
    range on counters
365. #         Add titles to the figures (e.g. "SEM image",
    "CL map 190-310 nm", "Average Spectrum")
366.
367.     width=12 #Width of the figure in inches
368.     fig=plt.figure(layout='tight',
    figsize=[width,width/4*3*0.75])
369.     fig.suptitle(title,fontsize=20)
370.

```

```

371.     mosaic=[[ 'Metadata' , 'Metadata' , 'Secondary SEM' , 'In-Lens
SEM' ],
372.             [ 'Counter 1' , 'Counter 2' , 'Counter 3'      , 'Counter
4'   ] ,
373.             [ 'Sum Map'   , 'Ave Spec' , 'Ave Spec'      , 'Ave
Spec'   ]]
374.     axs = fig.subplot_mosaic(mosaic=mosaic)
375.     percentile=1.
376.
377.     im_name='Metadata'
378.     metadata = ('File Name: ' + PurePath(datum.fname).name
379.                + '\nMagnification = ' +
str(round(datum.metadata.magnification)) + ' X'
380.                + '\nField of View = ' +
str(round(datum.metadata.FOV[0],2)) + ' nm'
381.                + '\nResolution = ' + str(datum.metadata.x_size) + ' x
' + str(datum.metadata.y_size)
382.                + '\nAcceleration Voltage = ' + str(datum.metadata.kV)
+ ' kV'
383.                + '\nCenter Wavelength = ' +
str(datum.metadata.center_wl) + ' nm'
384.                + '\nExposure Time = ' +
str(datum.metadata.exposure_time*1000) + ' ms')
385.     axs[im_name].text(0.02,0.2,metadata,fontsize=10)
386.     axs[im_name].axis('off')
387.
388.     im_name='Secondary SEM'
389.     plot_2D_map(datum.adc.squeeze()[:,:,1],axs[im_name],
390.                percentile=percentile,
391.                colormap='gray',
392.                x_pix_size=datum.metadata.x_pix_size,
393.                x_pix_unit=datum.metadata.pix_size_unit,
394.                show_color_bar=False)
395.
396.     im_name='In-Lens SEM'
397.     plot_2D_map(datum.adc.squeeze()[:,:,2],axs[im_name],
398.                percentile=percentile,
399.                colormap='gray',
400.                x_pix_size=datum.metadata.x_pix_size,
401.                x_pix_unit=datum.metadata.pix_size_unit,
402.                show_color_bar=False)
403.
404.     im_name='Counter 1'
405.     plot_2D_map(datum.ctr.squeeze()[:,:,0],axs[im_name],
406.                percentile=percentile,
407.                colormap='Blues',

```

```

408.         x_pix_size=datum.metadata.x_pix_size,
409.         x_pix_unit=datum.metadata.pix_size_unit,
410.         show_color_bar=True)
411.
412.     im_name='Counter 2'
413.     plot_2D_map(datum.ctr.squeeze()[(:,:,1)],axs[im_name],
414.                percentile=percentile,
415.                colormap='Greens',
416.                x_pix_size=datum.metadata.x_pix_size,
417.                x_pix_unit=datum.metadata.pix_size_unit,
418.                show_color_bar=True)
419.
420.     im_name='Counter 3'
421.     plot_2D_map(datum.ctr.squeeze()[(:,:,2)],axs[im_name],
422.                percentile=percentile,
423.                colormap='Oranges',
424.                x_pix_size=datum.metadata.x_pix_size,
425.                x_pix_unit=datum.metadata.pix_size_unit,
426.                show_color_bar=True)
427.
428.     im_name='Counter 4'
429.     plot_2D_map(datum.ctr.squeeze()[(:,:,3)],axs[im_name],
430.                percentile=percentile,
431.                colormap='Reds',
432.                x_pix_size=datum.metadata.x_pix_size,
433.                x_pix_unit=datum.metadata.pix_size_unit,
434.                show_color_bar=True)
435.
436.     im_name='Sum Map'
437.     plot_2D_map(datum.spec_map.squeeze().sum(-1),axs[im_name],
438.                percentile=percentile,
439.                colormap='plasma',
440.                x_pix_size=datum.metadata.x_pix_size,
441.                x_pix_unit=datum.metadata.pix_size_unit,
442.                show_color_bar=True)
443.
444.     im_name='Ave Spec'
445.     ave_spectrum(datum,axs[im_name])
446.     axs[im_name].axvspan(190, 310, alpha=0.5, color='blue')
447.     axs[im_name].axvspan(310, 409, alpha=0.5, color='green')
448.     axs[im_name].axvspan(409, 482, alpha=0.5, color='orange')
449.     axs[im_name].axvspan(482, 650, alpha=0.5, color='red')
450.
451.     return fig
452.

```

```

453. #Creates an interactive figure where a region of the spectra
    can be selected and a CL map updates to show the total
454. # luminescence within the selected band.
455. def band_selector(datum):
456.
457.     import matplotlib.widgets as wgt
458.     from mpl_toolkits.axes_grid1.inset_locator import
    InsetPosition
459.     import textwrap
460.
461.     #Create a figure with space for the CL map and the average
    CL spectra side by side
462.     mosaic=[['CLmap'      , 'Spectrum'],
463.             ['Range/Area', 'Buttons']]
464.     fig=plt.figure(constrained_layout=True, figsize=[12,4])
465.     axs = fig.subplot_mosaic(mosaic=mosaic,
    width_ratios=[1,3],height_ratios=[3,1])
466.     CLmap_ax=axs['CLmap']
467.     spec_ax=axs['Spectrum']
468.     axs['Buttons'].axis('off')
469.     axs['Range/Area'].axis('off')
470.     fig.return_data=datum
471.
472.     #Writes text into a box in the figure
473.     position = InsetPosition(axs['Buttons'], [0, 0, 0.4, 1])
    #posx, posy, width, height in percent of axis
474.     fig.text_ax = fig.add_axes([0,0,0.2,0.2]) #Initialize axis
    (size and position specified here don't matter)
475.     fig.text_ax.set_axes_locator(position)
476.     def write_text(text):
477.         fig.text_ax.cla()
478.         fig.text_ax.axis('off')
479.         text = text.split("\n")
480.         text = [textwrap.wrap(line,40) for line in text]
481.         text = "\n".join("\n".join(line) for line in text)
482.         fig.text_ax.text(0,1,text,fontsize=9,fontfamily='monosp
    ace',
483.                         horizontalalignment='left',vertical
    alignment='top')
484.         write_text('Cool stuff will go here eventually...')
485.
486.
487.
488.     #Initialize average spectrum of data set with ability to
    select a specific range of wavelengths
489.     spec_ax=ave_spectrum(datum,ax=spec_ax)

```

```

490.
491.     def span_on_select(xmin, xmax):
492.         pos=[np.searchsorted(datum.wls,xmin),np.searchsorted(da
         tum.wls,xmax)]
493.         band=np.sum(a=datum.spec_map.squeeze()[ :, :, pos[0]:pos[1
         ]],axis=2)
494.         CLmap_ax.imshow(band,cmap='magma',
495.             vmin=np.percentile(band,percentile),
496.             vmax=np.percentile(band,100-percentile),
497.             origin='lower')
498.         CLmap_ax.set_title(f'{round(xmin,1)} nm -
         {round(xmax,1)} nm')
499.         write_text(f'({fig.span.extents[0]},
         {fig.span.extents[1]})')
500.
501.         #remove rectangle selector and reset its extents
502.         fig.area.clear()
503.         fig.area.extents =
         (0,datum.spec_map.shape[2],0,datum.spec_map.shape[3])
504.
505.         fig.canvas.draw_idle()
506.
507.         fig.span = wgt.SpanSelector(
508.             spec_ax,
509.             span_on_select,
510.             "horizontal",
511.             useblit=True, #Set useblit=True on most backends for
         enhanced performance.
512.             props=dict(alpha=0.5, facecolor="tab:blue"),
513.             interactive=True,
514.             drag_from_anywhere=True)
515.
516.
517.
518.         #Initialize spectral map with the ability to select a
         specific area
519.         band=np.sum(a=datum.spec_map.squeeze(),axis=2)
520.         percentile=3
521.         CLmap_ax=plot_2D_map(band,CLmap_ax,
522.             percentile=percentile,
523.             colormap='magma',
524.             x_pix_size=datum.metadata.x_pix_size,
525.             x_pix_unit=datum.metadata.pix_size_unit,
526.             show_color_bar=True)
527.         CLmap_ax.set_title(f'{round(datum.wls[0],1)} nm -
         {round(datum.wls[-1],1)} nm')

```

```

528.
529.     def map_on_select(eclick, erelease):
530.         #Reset CL map to it's original state
531.         band=np.sum(a=datum.spec_map.squeeze(),axis=2)
532.         CLmap_ax.imshow(band,cmap='magma',
533.             vmin=np.percentile(band,percentile),
534.             vmax=np.percentile(band,100-percentile),
535.             origin='lower')
536.         CLmap_ax.set_title(f'{round(datum.wls[0],1)} nm -
           {round(datum.wls[-1],1)} nm')
537.
538.         #Remove span selector and reset its extents
539.         fig.span.clear()
540.         fig.span.extents=(datum.wls[0],datum.wls[-1])
541.
542.         #Get extents of selected area
543.         y1, y2, x1, x2 = np.array(fig.area.extents).astype(int)
544.         write_text(f'x1={x1}, x2={x2}\ny1={y1}, y2={y2}')
545.
546.         #Re-generate average spectrum based on selected area
547.         spec_ax.clear()
548.         spec_ax.plot(datum.wls,datum.spec_map.squeeze()[x1:x2,y
           1:y2,:].mean(axis=(0,1)),color='black')
549.         spec_ax.set_xlabel('Wavelength (nm)')
550.         spec_ax.set_ylabel('Intensity (a.u.)')
551.         spec_ax.set_title('Average CL Spectrum')
552.
553.         fig.canvas.draw_idle()
554.
555.         fig.area = wgt.RectangleSelector(
556.             CLmap_ax,
557.             map_on_select,
558.             useblit=True, #Set useblit=True on most backends for
           enhanced performance.
559.             props=dict(alpha=0.4, facecolor="tab:blue",
           edgecolor='white'),
560.             handle_props=dict(alpha=0), #make handles invisible
561.             interactive=True)
562.
563.
564.
565.         #Initialize the three buttons to close the figure, save the
           figure, and generate a new sliced dataset based on
566.         # the selected area/range.
567.         def close_fig(event):
568.             write_text("Close")

```

```

569.         fig.canvas.draw_idle()
570.         plt.close(fig)
571.     def save_fig(event):
572.         try:
573.             parent_dir = Path.cwd().parents[0]
574.             with open(str(parent_dir / 'Averaged Clear Regions
- new.csv'), 'a',newline='') as file:
575.                 csvwriter = csv.writer(file)
576.                 ind = [path.name for path in
sorted(Path.cwd().glob('*hyperspec_cl.h5'))].index(datum.fname.name)
577.                 #First row is (name, x1 pixel, x2 pixel, y1
pixel, y2 pixel, pixel size, pixel units)
578.                 csvwriter.writerow(tuple([f'{Path.cwd().name} -
{ind}'] ) + tuple({datum.fname.name}) +
tuple(map(int,fig.area.extents)) +
(datum.metadata.x_pix_size,datum.metadata.pix_size_unit))
579.                 csvwriter.writerow(datum.wls)
580.                 y1, y2, x1, x2 =
np.array(fig.area.extents).astype(int)
581.                 csvwriter.writerow(datum.spec_map.squeeze()[x1:
x2,y1:y2,:].mean(axis=(0,1)))
582.
583.                 write_text(f"Average spectrum for selected
region saved in {str(parent_dir / 'Averaged Clear Regions -
new.csv')}")
584.         except Exception as e:
585.             write_text(str(e))
586.
587.         fig.canvas.draw_idle()
588.     def slice_data(event):
589.         try:
590.             shape=[None]*len(datum.spec_map.shape)
591.             y1, y2, x1, x2 =
np.array(fig.area.extents).astype(int)
592.             w1 = np.searchsorted(datum.wls,fig.span.extents[0])
593.             w2 = np.searchsorted(datum.wls,fig.span.extents[1])
594.             shape[2]=[x1,x2]
595.             shape[3]=[y1,y2]
596.             shape[4]=[w1,w2]
597.             fig.return_data=datum.crop(shape)
598.
599.             write_text(f'Data sliced to index ranges
x=[{x1},{x2}], y=[{y1},{y2}], w=[{w1},{w2}].\nObtain sliced data
set with fig.return_data')
600.         except Exception as e:

```

```

601.         write_text(str(e))
602.
603.         fig.canvas.draw_idle()
604.
605.         fig.buttons=ObjectWithAttributes()
606.         fig.buttons_ax=ObjectWithAttributes()
607.
608.         position = InsetPosition(axes['Buttons'], [0.82, 0.05, 0.16,
609.         0.4]) #posx, posy, width, height in percent of axis
610.         fig.buttons_ax.close = fig.add_axes([0,0,0.2,0.2])
611.         #Initialize axis (size and position specified here don't matter)
612.         fig.buttons_ax.close.set_axes_locator(position)
613.         fig.buttons.close=wgt.Button(fig.buttons_ax.close, 'Close')
614.         fig.buttons.close.on_clicked(close_fig)
615.
616.         position = InsetPosition(axes['Buttons'], [0.62, 0.05, 0.16,
617.         0.4]) #posx, posy, width, height in percent of axis
618.         fig.buttons_ax.save = fig.add_axes([0,0,0.2,0.2])
619.         #Initialize axis (size and position specified here don't matter)
620.         fig.buttons_ax.save.set_axes_locator(position)
621.         fig.buttons.save=wgt.Button(fig.buttons_ax.save, 'Save')
622.         fig.buttons.save.on_clicked(save_fig)
623.
624.         position = InsetPosition(axes['Buttons'], [0.42, 0.05, 0.16,
625.         0.4]) #posx, posy, width, height in percent of axis
626.         fig.buttons_ax.slice = fig.add_axes([0,0,0.2,0.2])
627.         #Initialize axis (size and position specified here don't matter)
628.         fig.buttons_ax.slice.set_axes_locator(position)
629.         fig.buttons.slice=wgt.Button(fig.buttons_ax.slice, 'Slice')
630.         fig.buttons.slice.on_clicked(slice_data)
631.
632.
633.         plt.show()
634.
635.         return fig
636.
637.
638. #Convert each raster file to a .png and save them in a
639.     directory within the data directory
640. def convert_raster_files(files,save_dir):
641.     #files and save_dir should be pathlib objects
642.     from ipywidgets import IntProgress
643.     from IPython.display import display
644.
645.     plt.ioff() #Prevent the figures from showing in the
646.     notebook
647.
648.

```

```

639.     #If given save directory does not exist, create it.
640.     if Path.is_dir(save_dir)==False:
641.         Path.mkdir(save_dir)
642.
643.     progressBar=IntProgress(min=0, max=len(files),
        description='0/' + str(len(files)), style={'bar_color':'green'})
644.     print('Converting raster images and saving them in ' +
        str(save_dir))
645.     display(progressBar)
646.
647.     for ind, f in enumerate(files):
648.         #Update progress bar
649.         progressBar.value=ind+1
650.         progressBar.description=str(ind+1) + '/' +
        str(len(files))
651.
652.         datum=ScopeFoundryLoader(f)
653.         SEMimage=datum.adc.squeeze()[:,:,1]
654.
655.         figSize = [6,6] #[width,height] of final image in
        inches
656.         #dpi = SEMimage.shape[0]/figSize[0] #Dots per inch
        calculated to be same resolution as original image
657.         dpi = 2048/figSize[0]
658.         fig=plt.figure(ind,figSize,dpi,clear=True)
659.
660.         axx=plot_2D_map(SEMimage,
        percentile=1.,
661.             colormap='gray',
662.             x_pix_size=datum.metadata.x_pix_size,
663.             x_pix_unit=datum.metadata.pix_size_unit,
664.             show_color_bar=False)
665.
666.         # Save the figure with the same name as the data file,
        but with .h5 replaced with .png
667.         #plt.savefig(os.path.join(path,os.path.splitext(f)[0]+'
        .png'))
668.         plt.savefig(save_dir /
        Path(f.name).with_suffix('.png'))
669.         plt.close(fig)
670.
671.     plt.ion() #Turn automatic plotting back on for future
        figures
672.     progressBar.close()
673.     print('Done')
674.
675. #Lets you add attributes to an object

```

```

676. class ObjectWithAttributes(object):
677.     #Attributes can be added to object during call, e.g.
        var=ObjectWithAttributes(a=1,b='text'), or can be added
678.     # after the object is created, e.g. var.a=1, var.b='text'.
679.     #Iterating over this object will return each of its
        attributes (<attribute name="">, <attribute value="">).
680.
681.     def __init__(self, /, **kwargs):
682.         self.__dict__.update(kwargs)
683.
684.     def __iter__(self):
685.         for attr in vars(self):
686.             value=vars(self)[attr]
687.             yield attr, value
688.
689.     def __repr__(self):
690.         items = (f"{k}={v!r}" for k, v in
        self.__dict__.items())
691.         return "{}({})".format(type(self).__name__, ",
        ".join(items))
692.
693. #Sorts files in given directory (current working directory if
        none provided) into types and summarizes their metadata
694. #Returns the data directory as a pathlib object along with
        lists of the data files in that directory
695. def sort_files_from_directory(data_dir=None,
        show_metadata=True):
696.
697.     #If no data directory is specified, the current working
        directory will be used.
698.     if data_dir is None:
699.         data_dir=Path.cwd()
700.     else:
701.         data_dir=Path(data_dir)
702.     print('\033[1mData directory being used:\033[0m')
703.     print(str(data_dir) + '\n')
704.
705.     #Sort files
706.     sorted_files={}
707.     sorted_files['txts']=sorted(data_dir.glob('*.txt'))
708.     sorted_files['sifs']=sorted(data_dir.glob('*.sif'))
709.     sorted_files['hdf5s']=sorted(data_dir.glob('*.h5'))
710.     sorted_files['clmaps']=sorted(data_dir.glob('*hyperspec_cl.
        h5'))
711.     sorted_files['clims']=sorted(data_dir.glob('*sync_raster_sc
        an.h5'))

```

```

712.     sorted_files['raman']=sorted(data_dir.glob('*hyperspec_pica
      m_mcl.h5'))
713.
714.     #Print metadata
715.     if show_metadata==True:
716.         #for file_type in
      [[txts,'txts'],[sifs,'sifs'],[clmaps,'clmaps'],[clims,'clims']]:
717.         for file_type,files in sorted_files.items():
718.             #Only try to print metadata for file types when
      files of that type exist in given directory
719.             exclude_list=['hdf5s']
720.             if len(files)>0 and file_type not in exclude_list:
721.                 print_metadata(files, file_type)
722.
723.     return data_dir, sorted_files
724.
725. def print_metadata(files,file_type):
726.     #Collect metadata from files
727.     if file_type=='clmaps':
728.         print('\033[1m' + 'These are your CL maps:' +
      '\033[0m')
729.         headings=['#','File Name','Array
      Dimensions','Voltage','Wavelength Range','Field of View']
730.         metadata=[['' for a in range(len(headings))] for b in
      range(len(files)+2)]
731.         metadata[0]=headings
732.
733.         for i,file_path in enumerate(files):
734.             with h5py.File(file_path) as file:
735.                 try:
736.                     metadata[i+2][0]=str(i)
737.                     metadata[i+2][1]=file_path.name
738.                     metadata[i+2][2]=str(file['/measurement/hyp
      erspec_cl/spec_map/'].shape)
739.                     metadata[i+2][3]=f"{file['/hardware/sem_rem
      con/settings/'].attrs['kV']} kV "
740.                     metadata[i+2][4]=f"[{format(file['/measurem
      ent/hyperspec_cl/wls/'][0], '5.1f')} ,
      {format(file['/measurement/hyperspec_cl/wls/'][-1], '5.1f')}] nm"
741.                     Nh=file['/measurement/hyperspec_cl/settings
      /'].attrs['Nh']
742.                     dh=file['/measurement/hyperspec_cl/settings
      /'].attrs['dh']
743.                     Mag=file['/hardware/sem_remcon/settings/'].
      attrs['magnification']

```

```

744.             metadata[i+2][5]=f"{round(Nh*dh*4.25*2.54e7
/20/Mag)} nm"
745.             except:
746.                 metadata[i+2][0]=str(i)
747.                 metadata[i+2][1]=file_path.name
748.                 metadata[i+2][2]='\033[1mError reading
file\033[0m'
749.     elif file_type=='clims':
750.         print('\033[1m' + 'These are your SEM images:' +
'\033[0m')
751.         headings=['#', 'File Name', 'Array
Dimensions', 'Voltage', 'Field of View']
752.         metadata=[['' for a in range(len(headings))] for b in
range(len(files)+2)]
753.         metadata[0]=headings
754.
755.         for i,file_path in enumerate(files):
756.             with h5py.File(file_path) as file:
757.                 try:
758.                     metadata[i+2][0]=str(i)
759.                     metadata[i+2][1]=file_path.name
760.                     metadata[i+2][2]=str(file['measurement/sync
_raster_scan/adc_map/'].shape)
761.                     metadata[i+2][3]=f"{file['/hardware/sem_rem
con/settings/'].attrs['kV']} kV "
762.                     Nh=file['/measurement/sync_raster_scan/sett
ings/'].attrs['Nh']
763.                     dh=file['/measurement/sync_raster_scan/sett
ings/'].attrs['dh']
764.                     Mag=file['/hardware/sem_remcon/settings/'].
attrs['magnification']
765.                     metadata[i+2][4]=f"{round(Nh*dh*4.25*2.54e7
/20/Mag)} nm"
766.                 except:
767.                     metadata[i+2][0]=str(i)
768.                     metadata[i+2][1]=file_path.name
769.                     metadata[i+2][2]='\033[1mError reading
file\033[0m'
770.
771.     elif file_type=='txts':
772.         print('\033[1m' + 'These are your text files:' +
'\033[0m')
773.         headings=['#', 'File Name']
774.         metadata=[['' for a in range(len(headings))] for b in
range(len(files)+2)]
775.         metadata[0]=headings

```

```

776.
777.     for i,file_path in enumerate(files):
778.         metadata[i+2][0]=str(i)
779.         metadata[i+2][1]=file_path.name
780.
781.     elif file_type=='sifs':
782.         print('\033[1m' + 'These are your sifs files:' +
783.             '\033[0m')
784.         headings=['#','File Name']
785.         metadata=[['' for a in range(len(headings))] for b in
786.             range(len(files)+2)]
787.         metadata[0]=headings
788.
789.     for i,file_path in enumerate(files):
790.         metadata[i+2][0]=str(i)
791.         metadata[i+2][1]=file_path.name
792.
793.     elif file_type=='hdf5s':
794.         print('\033[1m' + 'These are your hdf5s files:' +
795.             '\033[0m')
796.         headings=['#','File Name']
797.         metadata=[['' for a in range(len(headings))] for b in
798.             range(len(files)+2)]
799.         metadata[0]=headings
800.
801.     for i,file_path in enumerate(files):
802.         metadata[i+2][0]=str(i)
803.         metadata[i+2][1]=file_path.name
804.
805.     elif file_type=='raman':
806.         print('\033[1m' + 'These are your Raman map files:' +
807.             '\033[0m')
808.         headings=['#','File Name','Array Dimensions','Laser
809.             λ','Raman Shift Range','Field of View']
810.         metadata=[['' for a in range(len(headings))] for b in
811.             range(len(files)+2)]
812.         metadata[0]=headings
813.
814.     for i,file_path in enumerate(files):
815.         with h5py.File(file_path) as file:
816.             try:
817.                 metadata[i+2][0]=str(i)
818.                 metadata[i+2][1]=file_path.name
819.                 metadata[i+2][2]=str(file['measurement/hype
820.                     rspec_picam_mcl/spec_map/'].shape)

```

```

813.             metadata[i+2][3]=str('532 nm') #This value
               not yet stored in file metadata (as of Jan. 2023), so manually
               set
814.             metadata[i+2][4]=f"{{round(file['measurement/hyperspec_picam_mcl/wls'][0],1)}} ,
               {{round(file['measurement/hyperspec_picam_mcl/wls'][-1],1)}}"
815.             metadata[i+2][5]=f"{{round(file['measurement
               /hyperspec_picam_mcl/imshow_extent'][1]-
               file['measurement/hyperspec_picam_mcl/imshow_extent'][0],1)}} μm"
816.             except:
817.                 metadata[i+2][0]=str(i)
818.                 metadata[i+2][1]=file_path.name
819.                 metadata[i+2][5]='\033[1mError reading
               file\033[0m'
820.
821.             else:
822.                 print(f"\033[1mSelected data type not yet
               supported:\033[0m {file_type}")
823.                 metadata=['']
824.
825.
826.             #Get length of longest element in each column of metadata
               so they can be properly justified
827.             for col in range(len(metadata[0])):
828.                 length=len(max([row[col] for row in metadata],key=len))
829.                 for row in metadata:
830.                     row[col]=row[col].ljust(length)
831.
832.                 #Bold the headings
833.                 metadata[0][col]=f"\033[1m{metadata[0][col]}\033[0m"
834.                 #Replace spaces in dividing line with dashes
835.                 metadata[1][col]=metadata[1][col].replace(" ", "-")
836.
837.             #Print the metadata
838.             for row in metadata:
839.                 print(*row, sep=' | ',end=' |\n')
840.             print('')
841.
842. #This is a wrapper for make_hspy_si that adds the capability to
               save hsi objects into a directory for future use.
843. def create_hsi(datum,save=False, save_dir=None ,
               spec_units='nm' , overwrite=False):
844. #datum should be a scope_foundry_loader object
845. #spec_units='nm' will plot vs wavelength while 'eV' will plot
               vs energy
846.

```

```

847.     #If no save directory is specified, the current working
        directory will be used.
848.     if save_dir==None:
849.         save_dir=os.getcwd()
850.
851.     #Check if a directory exists to save the hsi objects. If
        one doesn't, create it.
852.     path=os.path.join(save_dir,'Saved Objects')
853.     if os.path.exists(path)==False:
854.         os.mkdir(path)
855.
856.     if save==False:
857.         hsi=make_hspy_si(datum.spec_map.squeeze(),datum.wls,
858.             pix_size=[datum.metadata.x_pix_size ,
            datum.metadata.y_pix_size] ,
859.             x_units= datum.metadata.pix_size_unit,
860.             spec_units=spec_units)
861.
862.         hsi.metadata.General.source = datum.fname
863.         hsi.metadata.General.title =
            os.path.splitext(datum.fname)[0]+'.hspy'
864.         return hsi
865.
866.     #If overwrite is set to True, create a new hsi object
        regardless of whether or not it exists in the save directory
867.     if overwrite==True:
868.         hsi=make_hspy_si(datum.spec_map.squeeze(),datum.wls,
869.             pix_size=[datum.metadata.x_pix_size ,
            datum.metadata.y_pix_size] ,
870.             x_units= datum.metadata.pix_size_unit,
871.             spec_units=spec_units)
872.
873.         hsi.metadata.General.source = datum.fname
874.         hsi.metadata.General.title =
            os.path.splitext(datum.fname)[0]+'.hspy'
875.
876.         path=os.path.join(path,hsi.metadata.General.title)
877.         hsi.save(path,overwrite=True)
878.         return hsi
879.
880.     #Check if an hsi object for the specified datum exists. If
        it has, load the saved object, otherwise create one.
881.     path=os.path.join(path,os.path.splitext(datum.fname)[0] +
        '.hspy')
882.     if os.path.exists(path):
883.         return hs.load(path)

```

```

884.     else:
885.         hsi=make_hspy_si(datum.spec_map.squeeze(),datum.wls,
886.             pix_size=[datum.metadata.x_pix_size ,
            datum.metadata.y_pix_size] ,
887.             x_units= datum.metadata.pix_size_unit,
888.             spec_units=spec_units)
889.
890.         hsi.metadata.General.source = datum.fname
891.         hsi.metadata.General.title =
            os.path.splitext(datum.fname)[0] + '.hspy'
892.
893.         hsi.save(path)
894.         return hsi
895.
896. #Runs decomposition on given hyperspy object with NMF and
            determines the number of components to use based on the elbow
897. # position determined from an SVD decomposition
898. def decompose(hsi):
899.     #Use SVD decomposition to estimate the number of required
            components
900.     hsi.decomposition(normalize_poissonian_noise=False,
            algorithm='SVD',print_info=False)
901.     num=hsi.estimate_elbow_position(max_points=60)
902.     print(f'Estimated elbow position = {num}')
903.
904.     #Non-Negative Matrix Factorization
905.     #setting all negative values to 0
906.     a=hsi>0
907.     hsi=hsi*a
908.
909.     hsi.decomposition(algorithm='NMF',
910.         output_dimension=num,
911.         tol=1e-6,
912.         max_iter=100000
913.         )
914.
915.     x_vect=np.linspace(hsi.axes_manager[2].offset,
916.         hsi.axes_manager[2].offset+hsi.data.shape
            e[-1]*hsi.axes_manager[2].scale,
917.         num=hsi.data.shape[-1])
918.     comsplot(hsi.get_decomposition_loadings().data,hsi.get_dec
            omposition_factors().data,x_vect,
919.         comps=np.arange(num))
920.
921.     return hsi
922.

```

```

923. #Denoise CL map with SVD
924. def denoise_hsi(noisy_hsi, save=False, save_dir=None,
    overwrite=False):
925.
926.
927.     #If no save directory is specified, the current working
    directory will be used.
928.     if save_dir==None:
929.         save_dir=os.getcwd()
930.
931.     #Check if a directory exists to save the hsi objects. If
    one doesn't, create it.
932.     path=os.path.join(save_dir, 'Saved Objects')
933.     if os.path.exists(path)==False:
934.         os.mkdir(path)
935.
936.     if save==False:
937.         noisy_hsi.decomposition(normalize_poissonian_noise=False,
    algorithm='SVD')
938.         num=noisy_hsi.estimate_elbow_position(max_points=60)
939.         denoised_hsi=noisy_hsi.get_decomposition_model(components=num)
940.
941.         denoised_hsi.metadata.General.source =
    noisy_hsi.metadata.General.title
942.         denoised_hsi.metadata.General.title =
    os.path.splitext(noisy_hsi.metadata.General.title)[0] +
    '_denoised.hspy'
943.         return denoised_hsi
944.
945.     #If overwrite is set to True, denoise the data regardless
    of whether or not it exists in the save directory
946.     if overwrite==True:
947.         noisy_hsi.decomposition(normalize_poissonian_noise=False,
    algorithm='SVD')
948.         num=noisy_hsi.estimate_elbow_position(max_points=60)
949.         denoised_hsi=noisy_hsi.get_decomposition_model(components=num)
950.
951.         denoised_hsi.metadata.General.source =
    noisy_hsi.metadata.General.title
952.         denoised_hsi.metadata.General.title =
    os.path.splitext(noisy_hsi.metadata.General.title)[0] +
    '_denoised.hspy'
953.

```

```

954.         path=os.path.join(path,denoised_hsi.metadata.General.ti
           tle)
955.         denoised_hsi.save(path,overwrite=True)
956.         return denoised_hsi
957.
958.         #Check if a denoised version of the specified hsi object
           exists. If it has, load the saved object, otherwise create one.
959.         path=os.path.join(path,os.path.splitext(noisy_hsi.metadata.
           General.title)[0] + '_denoised.hspy')
960.         if os.path.exists(path):
961.             return hs.load(path)
962.         else:
963.             noisy_hsi.decomposition(normalize_poissonian_noise=False,
           algorithm='SVD')
964.             num=noisy_hsi.estimate_elbow_position(max_points=60)
965.             denoised_hsi=noisy_hsi.get_decomposition_model(component
           ts=num+1)
966.
967.             denoised_hsi.metadata.General.source =
           noisy_hsi.metadata.General.title
968.             denoised_hsi.metadata.General.title =
           os.path.splitext(noisy_hsi.metadata.General.title)[0] +
           '_denoised.hspy'
969.
970.             denoised_hsi.save(path)
971.             return denoised_hsi
972.
973. def
           linear_regression(x,y,plot_result=False,xlabel=None,ylabel=None):
974.
975.     def estimate_coef(x, y):
976.         # number of observations/points
977.         n = np.size(x)
978.
979.         # mean of x and y vector
980.         m_x = np.mean(x)
981.         m_y = np.mean(y)
982.
983.         # calculating cross-deviation and deviation about x
984.         SS_xy = np.sum(y*x) - n*m_y*m_x
985.         SS_xx = np.sum(x*x) - n*m_x*m_x
986.
987.         # calculating regression coefficients
988.         b_1 = SS_xy / SS_xx
989.         b_0 = m_y - b_1*m_x
990.

```

```

991.         return (b_0, b_1)
992.
993.     def plot_regression(x, y, b, xlabel, ylabel):
994.         # plotting the actual points as scatter plot
995.         plt.scatter(x, y)
996.
997.         # predicted response vector
998.         y_pred = b[0] + b[1]*x
999.
1000.        # plotting the regression line
1001.        plt.plot(x, y_pred)
1002.
1003.        # putting labels
1004.        plt.xlabel(xlabel)
1005.        plt.ylabel(ylabel)
1006.
1007.        # function to show plot
1008.        plt.show()
1009.
1010.
1011.    # estimating coefficients
1012.    b = estimate_coef(x, y)
1013.    print("Estimated coefficients:\nb_0 = {} \
1014.          \nb_1 = {}".format(b[0], b[1]))
1015.
1016.    # plotting regression line
1017.    if plot_result: plot_regression(x, y, b, xlabel, ylabel)
1018.
1019.    return b
1020.
1021. def mybin(s, xbin=1, ybin=1, sbin=1):
1022.     """Return spectrum s binned by factors xbin, ybin, sbin"""
1023.     if (xbin < 1) or (ybin < 1) or (sbin < 1):
1024.         raise ValueError("One of your binnings is smaller than
1025.           1. For signal axis to remain constant, leave as 1")
1026.
1027.     if all(n==1 for n in (xbin, ybin, sbin)):
1028.         print("Not binning because all binnings == 1")
1029.         return s # End Early
1030.
1031.     # Get signal channels
1032.     signal_channels = s.axes_manager.signal_shape[0]
1033.
1034.     # Make sure signal channel length is a multiple of two
1035.     if signal_channels % 2 != 0:

```

```

1035.         #print("Signal axis length is odd-numbered! Cropping
           spectrum by 1 signal channel!")
1036.         s = s.isig[0:-1]
1037.         signal_channels = s.axes_manager.signal_shape[0]
1038.
1039.         # Check if image is a single spectrum:
1040.         try:
1041.             s.axes_manager.navigation_shape[0]
1042.         except IndexError:
1043.             # This is a 0D Single Spectrum, don't bin X or Y
1044.             single_spectrum = True
1045.         else:
1046.             single_spectrum = False
1047.             nav_x_channels = s.axes_manager.navigation_shape[0]
1048.
1049.         if single_spectrum:
1050.             print("Binning " + s.metadata.General.title + " by ( |
           " + str(sbin) + ").")
1051.             s = s.rebin((signal_channels/sbin,))
1052.             print("New shape: " + str(s.data.shape))
1053.             return s
1054.
1055.         # Make sure nav X pixel length is a multiple of two
1056.         if nav_x_channels % 2 != 0:
1057.             #print("x-axis length is odd-numbered! Cropping
           spectrum by 1 signal channel!")
1058.             s = s.inav[:,-1,:]
1059.             nav_x_channels = s.axes_manager.navigation_shape[0]
1060.
1061.         # Check if image is a Line profile:
1062.         try:
1063.             s.axes_manager.navigation_shape[1]
1064.         except IndexError:
1065.             #This is a 1D Line profile, don't bin the Y axis
1066.             line_profile = True
1067.         else:
1068.             # This is a 2D Spectrum Image Map
1069.             line_profile = False
1070.             nav_y_channels = s.axes_manager.navigation_shape[1]
1071.
1072.         if not line_profile:
1073.             if nav_y_channels % 2 != 0:
1074.                 #print("x-axis length is odd-numbered!
           Cropping spectrum by 1 signal channel!")
1075.                 s = s.inav[:, :-1]

```

```

1076.             nav_y_channels =
1077.                 s.axes_manager.navigation_shape[1]
1078.         if line_profile:
1079.             print("Binning " + s.metadata.General.title + " by ("
1080.                   + str(xbin) + " | " + str(sbin) + ").")
1081.             s = s.rebin((nav_x_channels/xbin,
1082.                          signal_channels/sbin))
1083.             print("New shape: " + str(s.data.shape))
1084.         else:
1085.             print("Binning " + s.metadata.General.title + " by ("
1086.                   + str(xbin) + ", " + str(ybin) + " | " + str(sbin) + ").")
1087.             s = s.rebin((nav_x_channels/xbin, nav_y_channels/ybin,
1088.                          signal_channels/sbin))
1089.             print("New shape: " + str(s.data.shape))
1090.         return s
1091.
1092. def
1093.     initialize_multipeak_model(hsi,peaks,zero_points=None,pixel=None)
1094.     :
1095.     #hsi should be a hyperspy signal
1096.     model=hsi.create_model()
1097.
1098.     #Define background polynomial
1099.     #If no zero_points are provided, no background polynomial
1100.     will be generated
1101.     if zero_points is not None:
1102.         order=len(zero_points)-1
1103.         model.append(hs.model.components1D.Polynomial(order=or
1104. der,legacy=False))
1105.         model[-1].name='Background'
1106.         x1, x2 = zero_points
1107.
1108.     #If no pixel is specified, a background line will be
1109.     fit to every pixel in the navigation space
1110.     if pixel is None:
1111.         '''
1112.         for pixel in np.ndindex(hsi.data.shape[:2]):
1113.             #Find the corresponding intensity at each zero
1114.             point
1115.             y=[hsi.inav[pixel[1],pixel[0]].isig[float(x)].
1116.               data[0] for x in zero_points]
1117.             #Fit polynomial to set of x,y points and save
1118.             to model
1119.             coeffs=np.polynomial.polynomial.Polynomial.fit
1120.             (zero_points,y,order).convert().coef

```

```

1108.
1109.             for i, coeff in enumerate(coeffs):
1110.                 model.inav[pixel[1],pixel[0]].components.B
background.parameters[i].value=coeff
1111.                 '''
1112.                 y1 = np.average(hsi.isig[x1-1:x1+1].data, axis=2)
1113.                 y2 = np.average(hsi.isig[x2-1:x2+1].data, axis=2)
1114.                 #y=mx+b
1115.                 m=(y2-y1)/(x2-x1)
1116.                 b=y1-m*x1
1117.                 for pixel in np.ndindex(hsi.data.shape[:2]):
1118.                     model.axes_manager.indices=[pixel[1],pixel[0]]
1119.                     model.set_parameters_value('a0',
b[pixel[0]][pixel[1]], component_list=[0], only_current=True)
1120.                     model.set_parameters_value('a1',
m[pixel[0]][pixel[1]], component_list=[0], only_current=True)
1121.
1122.                 else:
1123.                     #Find the corresponding intensity at each zero
point
1124.                     y=[hsi.inav[pixel[1],pixel[0]].isig[float(x)].data
[0] for x in zero_points]
1125.                     #Fit polynomial to set of x,y points and save to
model
1126.                     coeffs=np.polynomial.polynomial.Polynomial.fit(zer
o_points,y,order).convert().coef
1127.                     for i, coeff in enumerate(coeffs):
1128.                         model.components.Background.parameters[i].valu
e=coeff
1129.
1130.                     #Fix all background components so they don't get
changed in the fitting process
1131.                     model.set_parameters_not_free(['Background'])
1132.
1133.                 #Define peaks
1134.                 for peak in peaks:
1135.                     if peak[1]=='Gauss':
1136.                         model.append(hs.model.components1D.Gaussian())
1137.                     elif peak[1]=='GaussHF':
1138.                         model.append(hs.model.components1D.GaussianHF())
1139.                     elif peak[1]=='GaussE': #Gaussian in energy space
(eV), converted to wavelength space (nm)
1140.                         model.append(hs.model.components1D.Expression(
1141.                             expression="height * exp(-(1/x - 1/x0) **
2 * 4 * log(2) * 1239.9^2 / fwhmE ** 2)",
1142.                             name="Gaussian",

```

```

1143.         position="x0",
1144.         x0=0, #nm
1145.         fwhmE=1, #eV
1146.         height=1,
1147.         module="numpy"))
1148.     elif peak[1]=='SkewNormal':
1149.         model.append(hs.model.components1D.SkewNormal())
1150.     elif peak[1]=='Lorentz':
1151.         model.append(hs.model.components1D.Lorentzian())
1152.     else:
1153.         print('Specified peak type, ' + peak[1] + ', has
not been implimented!')
1154.         return
1155.
1156.     model[-1].name=peak[0]
1157.     for i,parameter in enumerate(model[-1].parameters):
1158.         parameter.value=peak[i+2][0]
1159.         parameter.bmin=peak[i+2][1]
1160.         parameter.bmax=peak[i+2][2]
1161.         parameter.free=peak[i+2][3]
1162.     return model
1163.
1164.
1165. #Get names of files in cwd and sort them by type
1166. data_dir, sorted_files = sort_files_from_directory()
1167. txts=sorted_files['txts']
1168. sifs=sorted_files['sifs']
1169. hdf5s=sorted_files['hdf5s']
1170. clmaps=sorted_files['clmaps']
1171. clims=sorted_files['clims']
1172. raman_maps=sorted_files['raman']
1173.
1174. #Show summary for all files in clmaps
1175. %matplotlib inline
1176. save_dir=data_dir / 'Saved Figures' / 'Summaries'
1177. if Path.is_dir(save_dir)==False:
1178.     Path.mkdir(save_dir, parents=True)
1179. for i,CLmap in enumerate(clmaps):
1180.     try:
1181.         print(i,end="\r")
1182.         datum=ScopeFoundryLoader(CLmap)
1183.         si_summary_banded(datum)
1184.     except:
1185.         print(f"Failed to load file {CLmap.name}")
1186.     pass
1187.

```

```

1188. ind=1 #Choose index of CL map you want to run decomposition on
1189. datum=ScopeFoundryLoader(clmaps[ind])
1190.
1191. #Interactively look at emission in different bands of the
    spectrum
1192. %matplotlib qt
1193. fig=band_selector(datum)
1194.
1195. #fix pix[0,0]
1196. datum.spec_map[:, :, 0, 0, :] = datum.spec_map[:, :, 0, 1, :]
1197. #assume dark bckground as average of first 20 pixels
1198. datum.spec_map = datum.spec_map -
    datum.spec_map[:, :, :, :, 0:40].mean()
1199. #Create or load hyperspy object
1200. hsi = create_hsi(datum)
1201.
1202. #Remove spikes caused by cosmic radiation from data
1203. %matplotlib qt
1204. hsi.spikes_removal_tool()
1205.
1206. #Denoise data with SVD decomposition
1207. hsi_denoised=denoise_hsi(hsi)
1208.
1209. #Decompose CL map with NMF, using the elbow point from SVD to
    define the number of components
1210. hsi_denoised=decompose(hsi_denoised)
1211.
1212. #Use blind source separation to make decomposition more
    meaning full and potentially reduce the number of components
1213. num=6
1214. hsi.blind_source_separation(number_of_components=num)
1215. x_vect=np.linspace(hsi.axes_manager[2].offset,
1216.                    hsi.axes_manager[2].offset+hsi.data.shape[-
    1]*hsi.axes_manager[2].scale,
1217.                    num=hsi.data.shape[-1])
1218. compsplo(hsi.get_bss_loadings().data, hsi.get_bss_factors().da
    ta, x_vect,
1219.          comps=np.arange(num))</attribute></attribute>

```

B.2 Code for Normalization

The code below was written in Python 3.9 to normalize spectra from CL maps collected with the software package ScopeFoundry (available here: <https://www.scopefoundry.org/>).

```

1. from pathlib import Path, PurePath
2. from importlib.machinery import SourceFileLoader
3. import matplotlib.pyplot as plt
4. import csv
5. import hyperspy.api as hs
6. import numpy as np
7.
8. #prints text to command line and saves it to a log file
9. open('normalization log.txt', 'w').close()
10. def printlog(text):
11.     print(text)
12.     with open('normalization log.txt','a',newline='') as f:
13.         f.write(text + '\n')
14.
15. def find_SFUtils(base_dir,file_name=None):
16.     # It is assumed that the current working directory is in a directory tree
    branching from the base directory-
17.     # base_dir should simply be the name of this directory rather than its
    full file path.
18.
19.     # A directory titled "SFUtils" containing one or more versions of the
    SFUtils files is assumed to be a child
20.     # directory of the base directory. The latest version of these files
    will be run unless a file name is
21.     # specified.
22.
23.     #Find file path of base directory
24.     p=PurePath(Path.cwd())
25.     path= PurePath(p.parts[0])
26.     for part in p.parts[1:]:
27.         path = path / part
28.         if part==base_dir:
29.             break
30.
31.     #Check that the SFUtils directory exists, import the latest (or given)
    SFUtils file contained in it if it does
32.     path=Path(str(path / 'SFUtils'))
33.     if Path.is_dir(path):
34.         if file_name is None:
35.             path=sorted(path.glob('SFUtils*.py'))[-1]
36.         else:
37.             path=path / file_name
38.             if path.is_file()==False:
39.                 print(f'Unable to find specified SFUtils file:
    {str(path.name)} in directory {str(path.parent)}')
40.             return
41.
42.     printlog('SFUtils file found, loading ' + str(path.name))

```

```

43.
44.         m=SourceFileLoader(path.with_suffix('').name,
    str(path)).load_module()
45.         return m
46.     else:
47.         printlog('Unable to find SFUtils directory at ' + path)
48.
49. def get_average_spectrum_from_normalized_map(datum):
50.     printlog('Cleaning up data...')
51.     datum.spec_map[:, :, 0, 0, :] = datum.spec_map[:, :, 0, 1, :] #fix pix[0,0]
52.     datum.spec_map = datum.spec_map - datum.spec_map[:, :, :, :, 0:40].mean()
53.     #Create hyperspy object
54.     hsi = SF.create_hsi(datum)
55.     #Reduce noise and spikes
56.     hsi = SF.denoise_hsi(hsi)
57.     #Cut off data at end of band edge peaks to avoid any interference from
    defect peaks
58.     hsi_cropped = hsi.isig[:215.]
59.     #Bin data to reduce number of pixels that need to be fit to the model
60.     #hsi = mybin(hsi,2,2)
61.
62.     #Initialize model
63.     init_peaks=[# Peak Name, Type,     Parameters [value, min, max, free]
64.                ['TA/LA'      , 'Gausse', [0.1,0.01,0.4,True],
    [250,0,None,True], [210.3,210.3,211.4,False]],
65.                ['TO/LO'      , 'Gausse', [0.1,0.01,0.4,True],
    [350,0,None,True], [214.83,213.82,214.83,False]]
66.                ]
67.     #Wavelengths where the spectrum should be at zero intensity
68.     zero_points=[hsi.axes_manager[2].offset,200.] #currently can only do two
    points
69.     hsi_model=SF.initialize_multipeak_model(hsi_cropped,init_peaks,zero_point
    s)
70.
71.     #Enforce that the height parameters of the two peaks must be proportional
    by the given proportionality constant
72.     p1=hsi_model[1].parameters[1]
73.     p2=hsi_model[2].parameters[1]
74.     const=6 #proportionality constant between the height parameters
75.     p1.twin = p2
76.     p1.twin_function_expr = f"x/{const}"
77.     p1.twin_inverse_function_expr = f"x*{const}"
78.
79.     #Fit model to first pixel, then do the rest of the map
80.     printlog('Fitting peaks')
81.     hsi_model.fit(return_info=False,bounded=True)
82.     hsi_model.multifit(bounded=True,iterpath='serpentine',show_progressbar=Fa
    lse)

```

```

83.
84.     printlog('Normalizing data by TOLO peak height')
85.     #Divide the spectrum at each pixel by the height of the TALA peak at that
      pixel
86.     newdatacube = (hsi.data.transpose() /
      hsi_model[2].parameters[1].map['values'].transpose()).transpose()
87.     hsi_norm = hs.signals.Signal1D(newdatacube)
88.
89.     #Recreate all the relevant metadata to match the metadata of the original
      hypserpy object
90.     hsi_norm.metadata.General.title = hsi.metadata.General.title +
      '_normalized'
91.     hsi_norm.axes_manager[0].name = 'x'
92.     hsi_norm.axes_manager[0].scale = hsi.axes_manager[0].scale
93.     hsi_norm.axes_manager[0].units = hsi.axes_manager[0].units
94.     hsi_norm.axes_manager[1].name = 'y'
95.     hsi_norm.axes_manager[1].scale = hsi.axes_manager[1].scale
96.     hsi_norm.axes_manager[1].units = hsi.axes_manager[1].units
97.     hsi_norm.axes_manager[2].name = 'Wavelength'
98.     hsi_norm.axes_manager[2].offset = hsi.axes_manager[2].offset
99.     hsi_norm.axes_manager[2].scale = hsi.axes_manager[2].scale
100.    hsi_norm.axes_manager[2].units = 'nm'
101.
102.    printlog('Calculating average')
103.    xl=hsi_norm.data.shape[2]
104.    xi=hsi_norm.axes_manager[2].offset
105.    xf=xi + hsi_norm.axes_manager[2].scale*xl
106.    wls=np.linspace(xi,xf,xl)
107.    ave_spec=hsi_norm.data.mean(axis=(0,1))
108.    return wls,ave_spec
109.
110. SF=find_SFUtils(base_dir='LBL x KSU hBN Research')
111.
112. data_dir=Path.cwd() #Current working directory should contain the data
113.
114. #Create a csv writer object
115. with open(str(data_dir / 'Averaged Normalized Maps of All Data.csv'),
      'w',newline='') as file:
116.     csvwriter = csv.writer(file)
117.     printlog(f'Appending data from {data_dir.name}...'.ljust(56,'-'))
118.
119.     data_dir, sorted_files =
      SF.sort_files_from_directory(data_dir=data_dir, show_metadata=False)
120.     clmaps=sorted_files['clmaps']
121.     for i,CLmap in enumerate(clmaps):
122.         try:
123.             printlog(f'Loading file {CLmap.name}')
124.             datum=SF.ScopeFoundryLoader(CLmap)

```

```
125.         wls, ave_spec = get_average_spectrum_from_normalized_map(datum)
126.
127.         printlog(f'Saving average spectrum to csv file')
128.         csvwriter.writerow([f'{data_dir.name} - {i}'])
129.         csvwriter.writerow(wls)
130.         csvwriter.writerow(ave_spec)
131.     except Exception as e:
132.         printlog(str(e))
133.         printlog('Done!\n')
134.     printlog('-'*56 + '\n\n')
```